Université de Neuchâtel
Institut de Microtechnique

Resonant Grating Filters for Microsystems

Thèse

Présentée à la Faculté des Sciences
pour obtenir le grade de docteur ès sciences
par

Guido Niederer

Neuchâtel, avril 2004

IMPRIMATUR POUR LA THESE

Resonant grating filters for microsystems

M. Guido NIEDERER

UNIVERSITE DE NEUCHATEL

FACULTE DES SCIENCES

La Faculté des sciences de l'Université de Neuchâtel, sur le rapport des membres du jury

MM. H.-P. Herzig (directeur de thèse),
R. Dändliker, D. Erni (Zürich),
M. Schnieper (Zürich) et O. Parriaux (St-Etienne F)

autorise l'impression de la présente thèse.

Neuchâtel, le 20 avril 2004

La doyenne:

Martine Rahier

Abstract

In the present work we report on the design and characterization of a tunable optical filter for use in a compact add-drop multiplexer. The optical filter is a resonant grating filter (RGF) consisting of a planar waveguide and a grating parallel to the surface. A resonance occurs when the incoming light is diffracted by the grating and matches a mode in the waveguide. Numerous aspects of the modeling, design optimization, fabrication tolerances and characterization are addressed. A particular emphasis is given to miniaturization of the device for use in a MEMS microsystem.

We have investigated tunable, oblique incidence resonant grating filters covering the C-band as add-drop devices for incident TE-polarized light. The fabrication tolerances as well as the role of the finite incident beam size and limited device size are addressed. The maximum achievable efficiency of a finite-area device as well as a scaling law relating the resonance peak width and the minimum device size are derived. In a filter application it is important to have negligible shape changes over the tuning range. This is shown in theory as well as in experiments, where we measured the resonance peak from 1526nm at 45° angle of incidence to 1573nm at 53° with a full width at half maximum of 0.4nm. In this range the shift of the peak wavelength is linear with respect to a change in the incidence angle. Infinite beams and devices show ideal performance. The performance decreases for smaller systems. We present the limits of miniaturization. Theoretical modeling shows that the minimum size is in the millimeter range. Additional aspects, such as the influence of wavefront distortion of the reflected and transmitted beams are studied. Wavefront distortions are important for fiber coupling. Finally polarization independent configurations are studied, leading to a novel tunable design.

Contents

1. Introduction

1.1. Motivation

In the last decade the demand for capacity in data transmission has exploded, mainly because of the internet. The most promising high-speed data transmission technology for long and medium distances is optical fiber. Through multiplex techniques, such as WDM, many channels can be packed onto the same fiber, with different carrier frequencies. Each channel occupies a frequency band and very selective optical filters are needed to separate them. Optical fibers are excellent carriers with extremely high capacity and low loss. But the fiber based technology has a bottleneck in switching rapidly between different fibers. An electronic switch between two or more transmission lines can redirect every packet (a few Bytes). In optical transmission we are far from this goal, since the switch is far too slow to be able to separate individual packets. Thus we focus on channel switching. This means that the channels are routed from a port to another port. Between two switching actions, a large amount of data (in comparison to only a few Bytes in packet switching) is redirected within a fixed switching configuration. Today's reconfigurable switches are often large and expensive. The goal of this collaboration between three labs (IMT-Applied Optics Lab, IMT-Samlab and

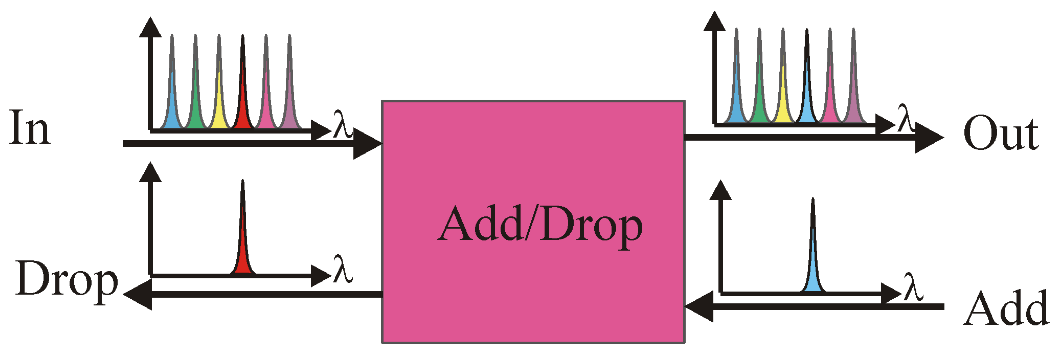

Fig. 1.1: Outline of the basic concept of an add-drop device. One channel of the incoming light is dropped and at its place another channel can be added.

CSEM Zurich) is to realize a compact and tunable optical add-drop multiplexer, as shown in Fig. 1.1. This thesis investigates the *design of the tunable optical filter*, including its *potential for miniaturization,* and its *characterization*. The filter is fabricated by CSEM and Samlab investigates the tiltable MEMS platform. The desired spectral reflection response of the optical filter is a rectangular shape; i.e. always zero except for a narrow frequency band with 100% reflectivity. The ideal spectral transmission response is the complement of the ideal reflection response; i.e. everywhere complete transmission except for a narrow frequency band with zero transmission.

1.2. Choice of the system

In the selection of the system for a compact and tunable optical multiplexer several constraints are present. The frequency grid for telecommunication, defined by the ITU (http://www.itu.int/home/), is extremely dense. For example the 100GHz channel spacing translates into a channel separation of only 0.8nm. The target spectrum of operation is the C-band, thus around 1550nm. This dense spacing requires extremely sharp passband edges or in resonance terms an extremely high Q-factor. In order to obtain this selectivity we decided to use a resonance phenomenon, by means of resonant grating filters (RGF). A RGF is a planar device, having a planar waveguide and a grating, parallel to the surface. We decided to use a reflection RGF. Then the majority of the incident light is essentially transmitted. But a small spectral band of the incident light is coupled through the grating into the waveguide. When coupling out again, the light interferes destructively with the transmitted beam resulting in a strong reflection [GOL85]. The resonance wavelength is a function of the incidence angle. So tuning can be performed by changing the angle of incidence or equivalently by tilting the filter, shown in Fig. 1.2.

The filter is glued on a silicon MEMS-platform. The MEMS part is studied by Samlab. However, an important point is to study the aspects of miniaturization. This platform can be tilted and is actuated by comb-drives [OVE02]. For proper operation a collimated incident beam is necessary, impinging under an oblique incident angle on the filter. The transmitted and reflected light is collected by additional collimators. With an AR-coating on the substrate, the element shows the same spectral response for light coming from the left or the right. So

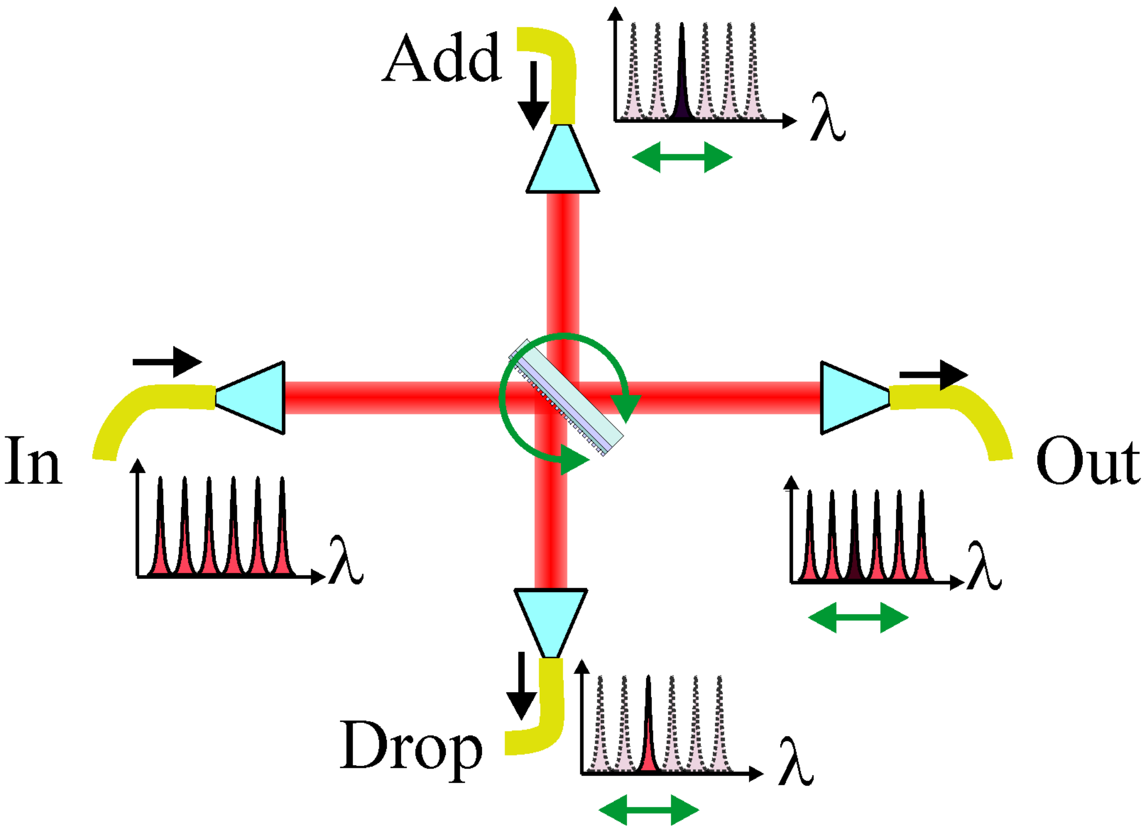

Fig. 1.2: RGF-Add/Drop device. A channel of the incoming light is reflected by the RGF into the drop output. The add channel with the same carrier frequency as the drop channel is reflected towards the output fiber.

with a single element, it is possible to build directly an add-drop device. This is done as shown in Fig. 1.2 with a channel coming from the top as the add-channel. For this channel the element shows strong reflection and so the beam is reflected to the right. The channels entering from the left are all transmitted with the exception of the drop-channel which is reflected towards the bottom.

1.3. Structure of this thesis

After the introduction (Chapter 1), the theoretical basis for the rigorous simulations is presented (Chapter 2). Starting from the Maxwell Equations we present the formulation of the Fourier modal method (FMM). In Chapter 3 weak coupling RGFs in classical mount (plane of incidence perpendicular to the grating grooves) are analyzed in detail, including fabrication tolerances. After determination of the relevant parameters and their influence on the optical response, a design procedure is proposed. The fabrication of such filters is described and the fabricated elements are characterized. In Chapter 4 some approximate models are presented. They are needed for better understanding of the coupling process and necessary for the design concept. In addition they give good initial conditions for numerical optimization with rigorous methods. Furthermore they can predict effects due to finite size. In Chapter 5 we investigate polarization independent devices. For this purpose we deal with conical incidence, as well as with crossed gratings. In Chapter 6 we discuss the system aspects. From the approximate model a scaling law is derived. The reflected and transmitted fields of a finite incident beam are distorted. Taking into account this distortion and the finite beams, fiber coupling efficiencies and resulting channel crosstalks are estimated. The weak coupling devices need a certain coupling length, often several millimeters. This cannot be handled with rigorous methods with today's computers. So a strong coupling device was designed, with a much smaller coupling length. At the basis of this strong coupling device, the effects of finite element size can be deduced. At the end a conclusion (Chapter 7) is given.

2. Theory

In this chapter we present the theoretical basis for use in later simulations. The structures of interest are modulated in the vertical and horizontal directions. In the lateral direction, the modulation is periodic or almost periodic. The modulations in the vertical direction are simple, basically (structured) thin film layers. The feature sizes are on the order of the wavelength and resonance phenomena occur. Rigorous theories are therefore required. The length of the involved gratings exceeds the size of the computational domain of most rigorous solvers. We can instead apply periodic boundary conditions and thus model an infinite grating and use rigorous grating theories. It is shown in chapter 6 that it is possible to simulate finite elements and incidence beam with grating diffraction theory.

In the first part starting from Maxwell's Equations we find an appropriate set of equations to describe the steady state situation of time harmonic fields and isotropic, non-magnetic materials. In the second part we focus on rigorous grating theory, especially the Fourier modal method (FMM).

2.1. General electromagnetic theory

2.1.1. Maxwell's equations

The properties of light are entirely described by Maxwell's equations, which hold at every point in whose neighborhood the physical properties of the medium are continuous:

$$\nabla \times \mathbf{E} + \dot{\mathbf{B}} = 0 \tag{2.1}$$

$$\nabla \times \mathbf{H} = \mathbf{j} + \dot{\mathbf{D}} \tag{2.2}$$

$$\nabla \cdot \mathbf{D} = \rho \tag{2.3}$$

$$\nabla \cdot \mathbf{B} = 0\,. \tag{2.4}$$

E is the electrical field, **H** is the magnetic field, **D** is the electric displacement (also called electric flux density), **B** is the magnetic flux density (or magnetic induction), ρ the charge density and **j** the electric current density. A summary of the names of the fields and the relevant constants with their units is given in Appendix A. $\nabla \times \mathbf{U}$ denotes the curl operator on the field **U** and $\nabla \cdot \mathbf{U}$ denotes the div operator on **U**. $\dot{\mathbf{U}}$ means differentiation of **U** with respect to the time. Implicit in the Maxwell equations is the *continuity equation* for the charge density and the current density, showing the conservation of electric charges.

$$\dot{\rho} + \nabla \cdot \mathbf{j} = 0 \tag{2.5}$$

2.1.2. Material properties, constitutive relations

The Maxwell Eqs. (2.1)–(2.4) involve 4 different fields. The electric fields **E** and **D** as well as the magnetic fields **H** and **B** are related to each other depending on the electric and magnetic properties of their media:

$$\mathbf{D} = \varepsilon_0 \mathbf{E} + \mathbf{P} \tag{2.6}$$

$$\mathbf{B} = \mu_0 (\mathbf{H} + \mathbf{M}). \tag{2.7}$$

P is the polarization density and **M** the magnetization density. They are both zero for free space and thus describe the difference between free space and the medium of interest. ε_0 and μ_0 are constants. In this work we only consider linear media, i.e. |**E**| and |**P**| as well as |**H**| and |**M**| have a linear relation. This is important because then the principle of superposition applies. For *linear* media Eqs. (2.6) and (2.7) can be rewritten as a tensor relation:

$$\mathrm{D_i} = \varepsilon_0 \sum\nolimits_k \varepsilon_{ik} \mathrm{E_k} \tag{2.8}$$

$$\mathrm{B_i} = \mu_0 \sum\nolimits_k \mu_{ik} \mathrm{H_k}. \tag{2.9}$$

This relation describes the optical properties of anisotropic linear materials. These relations further simplify for *isotropic* materials. Their physical properties are independent of the direction und thus **D** and **E**, as well as **B** and **H** are parallel, i.e.

$$\mathbf{D} = \varepsilon_0 \varepsilon \mathbf{E} \tag{2.10}$$

$$\mathbf{B} = \mu_0 \mu \mathbf{H}. \tag{2.11}$$

The number ε is the electric permittivity and the number μ is the magnetic permeability. Non-magnetic materials are characterized by the fact that μ=1.

The current density **j** and the electric field **E** are related through *Ohm's Law*:

$$\mathbf{j} = \sigma\mathbf{E}\,, \tag{2.12}$$

with the specific conductivity σ.

A dielectric material is characterized by the absence of free charges, thus |**j**|=0 and ρ=0. This implies that σ =0 for a dielectric material.

A conducting, linear isotropic material (metal) has a non-zero specific conductivity and implies therefore through Eq. (2.12) a current density. It can be shown (chapter 13 of [BOR93]) that for optical frequencies the relaxation time of the charge densities is so small, that they return in a good approximation immediately into their state of equilibrium and thus the charge density can be set to zero.

For *non-magnetic, linear, dielectric* and *isotropic* materials, the Maxwell Eqs. (2.1)–(2.4), only involving **E** and **H** can be written as

$$\nabla \times \mathbf{E} + \mu_0 \dot{\mathbf{H}} = 0 \tag{2.13}$$

$$\nabla \times \mathbf{H} = \varepsilon\varepsilon_0 \dot{\mathbf{E}} \tag{2.14}$$

$$\nabla \cdot \mathbf{E} = 0 \tag{2.15}$$

$$\nabla \cdot \mathbf{H} = 0\,. \tag{2.16}$$

It is shown afterwards that dielectric materials are lossless materials.

2.1.3. Boundary conditions

A continuous change of the material properties leads to a continuous change of the fields. In the presence of an abrupt change of the material properties, such as the interface of medium 1 (subindex 1 of the fields) and medium 2 (subindex 2 of the fields), the smooth variation of the fields is destroyed. The integral form of Maxwell's Equations reveals the boundary conditions for the electric and magnetic fields [JAC75]

$$\mathbf{n}_{12} \cdot (\mathbf{D_2} - \mathbf{D}_1) = \rho_s \tag{2.17}$$

$$\mathbf{n}_{12} \cdot (\mathbf{B_2} - \mathbf{B}_1) = 0 \tag{2.18}$$

$$\mathbf{n}_{12} \times (\mathbf{E_2} - \mathbf{E}_1) = \mathbf{j} \tag{2.19}$$

$$\mathbf{n}_{12} \times (\mathbf{H_2} - \mathbf{H}_1) = \mathbf{0}\,. \tag{2.20}$$

$\mathbf{n}_{12}$ is the unit vector perpendicular to the interface pointing from medium 1 into medium 2 and ρ_s is the surface charge density on the surface. The scalar Eqs. (2.17) and (2.18) mean that the normal components of the electric displacement **D** and the magnetic induction **B** are continuous. The vectorial Eqs. (2.19) and (2.20) state that the tangential components of the electric field **E** and the magnetic field **H** are continuous. These boundary conditions were derived from the general Maxwell's Equations and, thus, do not include any assumption concerning the materials.

2.1.4. Wave equation, time harmonic fields

Since we only consider linear materials, the principle of superposition applies. Furthermore every time-dependent field can be split into a series of time harmonic fields, via Fourier analysis [GOO96]. The same principle applies for the reciprocal space. Every polychromatic wave can be split in a set of monochromatic waves. So if we know the optical response of time harmonic monochromatic fields, the solution involving time dependent polychromatic fields can be derived. For mathematical convenience we introduce the complex representation, where $\Re\{\ \}$ stands for the real part of the complex argument, i is the imaginary unity, t is time, and ω the angular frequency. The physical time-varying electric and magnetic fields $\mathbf{E}(\mathbf{r},t)$ and $\mathbf{H}(\mathbf{r},t)$, with **r** a vector containing the coordinates, can be expressed as

$$\mathbf{E}(\mathbf{r},t) = \Re\{\mathbf{E}(\mathbf{r})\exp(-i\omega t)\} \tag{2.21}$$

$$\mathbf{H}(\mathbf{r},t) = \Re\{\mathbf{H}(\mathbf{r})\exp(-i\omega t)\}\,. \tag{2.22}$$

The great advantage of this representation is obvious when looking at the time derivation. The time derivative of time harmonic fields simply results in a multiplication by a factor of –iω. Thus the Maxwell Equations (2.1)–(2.4) for time harmonic fields become

$$\nabla \times \mathbf{E}(\mathbf{r}) = i\omega \mathbf{B}(\mathbf{r}) \tag{2.23}$$

$$\nabla \times \mathbf{H}(\mathbf{r}) = \mathbf{j}(\mathbf{r}) - i\omega \mathbf{D}(\mathbf{r}) \tag{2.24}$$

$$\nabla \cdot \mathbf{D}(\mathbf{r}) = \rho(\mathbf{r}) \tag{2.25}$$

$$\nabla \cdot \mathbf{B}(\mathbf{r}) = 0\,. \tag{2.26}$$

They further reduce for isotropic linear materials, including the use of Ohm's law, Eq. (2.12), to

$$\nabla \times \mathbf{E}(\mathbf{r}) = i\omega \mu(\mathbf{r}) \mu_0 \mathbf{H}(\mathbf{r}) \tag{2.27}$$

$$\nabla \times \mathbf{H}(\mathbf{r}) = \left(\sigma(\mathbf{r}) - i\omega \varepsilon(\mathbf{r}) \varepsilon_0\right) \mathbf{E}(\mathbf{r}) \tag{2.28}$$

$$\varepsilon_0 \left[\nabla \varepsilon(\mathbf{r})\right] \cdot \mathbf{E}(\mathbf{r}) + \varepsilon_0 \nabla \cdot \left[\varepsilon(\mathbf{r}) \mathbf{E}(\mathbf{r})\right] = \rho(\mathbf{r}) \tag{2.29}$$

$$\nabla \cdot \mathbf{H}(\mathbf{r}) = 0\,. \tag{2.30}$$

It is convenient to introduce a complex permittivity $\hat{\varepsilon}$ to simplify Eq. (2.28):

$$\hat{\varepsilon}(\mathbf{r}) = \varepsilon(\mathbf{r}) - i\frac{\sigma}{\varepsilon_0 \omega} \tag{2.31}$$

Then Eq. (2.12) is introduced in Eq. (2.5) by supposing isotropic conductivity yielding

$$\dot{\rho}(\mathbf{r}, t) + \sigma \nabla \cdot \mathbf{E}(\mathbf{r}, t) = 0\,. \tag{2.32}$$

For a time harmonic electric field Eq. (2.32) can directly be integrated:

$$\rho(\mathbf{r}, t) = -\frac{\sigma}{i\omega} \nabla \cdot \mathbf{E}(\mathbf{r}, t) + C\,. \tag{2.33}$$

C is the integration constant. To satisfy Eq.(2.3), the charge density must vanish without a field present and thus the integration constant must vanish (C=0). From Eqs. (2.29) and (2.33) we find

$$\varepsilon_0 \left[\nabla \varepsilon(\mathbf{r})\right] \cdot \mathbf{E}(\mathbf{r}) + \varepsilon_0 \nabla \cdot \left[\hat{\varepsilon}(\mathbf{r}) \mathbf{E}(\mathbf{r})\right] = 0\,. \tag{2.34}$$

Finally we get the final form of the Maxwell Equations for non magnetic materials which we use in this work,

$$\nabla \times \mathbf{E}(\mathbf{r}) = i\omega \mu_0 \mathbf{H}(\mathbf{r}) \tag{2.35}$$

$$\nabla\times\mathbf{H}(\mathbf{r}) = -i\omega\hat{\varepsilon}(\mathbf{r})\varepsilon_0\mathbf{E}(\mathbf{r}) \tag{2.36}$$

$$\varepsilon_0\left[\nabla\varepsilon(\mathbf{r})\right]\cdot\mathbf{E}(\mathbf{r}) + \varepsilon_0\nabla\cdot\left[\hat{\varepsilon}(\mathbf{r})\mathbf{E}(\mathbf{r})\right] = 0 \tag{2.37}$$

$$\nabla\cdot\mathbf{H}(\mathbf{r}) = 0\,. \tag{2.38}$$

By using elementary vector operations, we can reduce the above equations to two equations and furthermore separate the magnetic and electric fields [TUR97]:

$$\mathbf{\Delta E}(\mathbf{r}) + \nabla\left[\frac{\nabla\hat{\varepsilon}(\mathbf{r})}{\hat{\varepsilon}(\mathbf{r})}\cdot\mathbf{E}(\mathbf{r})\right] + \hat{\varepsilon}(\mathbf{r})k_0^2\mathbf{E}(\mathbf{r}) = \mathbf{0} \tag{2.39}$$

$$\mathbf{\Delta H}(\mathbf{r}) + \frac{\nabla\hat{\varepsilon}(\mathbf{r})}{\hat{\varepsilon}(\mathbf{r})}\times\left[\nabla\times\mathbf{H}(\mathbf{r})\right] + \hat{\varepsilon}(\mathbf{r})k_0^2\mathbf{H}(\mathbf{r}) = \mathbf{0}\,, \tag{2.40}$$

where $\mathbf{\Delta}$ designates the Laplace operator, ∇ the gradient operator and $k_0 = 2\pi/\lambda_0$ is the wave number in vacuum. These two equations are *Helmholtz equations.* We can render these two equations in the form of wave equations for time harmonic fields. Since a temporal derivation simply corresponds to a multiplication by a factor of –iω, the *wave equations* become

$$\mathbf{\Delta E}(\mathbf{r}) - \hat{\varepsilon}(\mathbf{r})\frac{k_0^2}{\omega^2}\ddot{\mathbf{E}}(\mathbf{r}) = -\nabla\left[\frac{\nabla\hat{\varepsilon}(\mathbf{r})}{\hat{\varepsilon}(\mathbf{r})}\cdot\mathbf{E}(\mathbf{r})\right] \tag{2.41}$$

$$\mathbf{\Delta H}(\mathbf{r}) - \hat{\varepsilon}(\mathbf{r})\frac{k_0^2}{\omega^2}\ddot{\mathbf{H}}(\mathbf{r}) = -\frac{\nabla\hat{\varepsilon}(\mathbf{r})}{\hat{\varepsilon}(\mathbf{r})}\times\left[\nabla\times\mathbf{H}(\mathbf{r})\right]. \tag{2.42}$$

The above equations are, in general, inhomogeneous equations. The different field components couple through the inhomogeneity. For a homogeneous material, they reduce to the classical wave equation, without the terms on the right side of Eqs. (2.41)–(2.42). According to a wave equation the propagation speed c is defined as

$$c^2 = \frac{\omega^2}{k_0^2}\Re\left\{\hat{\varepsilon}(\mathbf{r})\right\} = \frac{\varepsilon(\mathbf{r})}{\varepsilon_0\mu_0} = c_0^2\varepsilon(\mathbf{r})\,. \tag{2.43}$$

An electromagnetic wave in free space travels with the speed c_0

$$c_0 = \frac{1}{\sqrt{\varepsilon_0\mu_0}} = 2.99792458\;10^8\,\frac{\mathrm{m}}{\mathrm{s}}\,. \tag{2.44}$$

We introduce the complex refractive index $\hat{n}(\mathbf{r})$ through *Maxwell's relation* as

$$\hat{n}(\mathbf{r}) = \sqrt{\hat{\varepsilon}(\mathbf{r})}\,, \tag{2.45}$$

which can be written in another form:

$$\left(\hat{n}(\mathbf{r})\right)^2 = \left(n(\mathbf{r}) + i\kappa(\mathbf{r})\right)^2 = \hat{\varepsilon}(\mathbf{r}) = \varepsilon(\mathbf{r}) + i\frac{\sigma(\mathbf{r})}{\varepsilon_0\omega}. \tag{2.46}$$

n is the real part and κ the imaginary part of the complex refractive index. n is related to the phase velocity, whereas κ is associated to the absorption of the propagating wave. κ is related to the exponential decay constant α by the following relation

$$\alpha = \frac{4\pi}{\lambda}\kappa\,. \tag{2.47}$$

2.1.5. Solutions for a homogeneous medium

A homogenous medium is characterized by the fact that the dielectric constant ε is independent of position and thus its divergence vanishes. Then the Helmoltz Eqs. (2.39) and (2.40) become

$$\mathbf{\Delta E}(\mathbf{r}) + \hat{\varepsilon}k_0^2\mathbf{E}(\mathbf{r}) = \mathbf{0} \tag{2.48}$$

$$\mathbf{\Delta H}(\mathbf{r}) + \hat{\varepsilon}k_0^2\mathbf{H}(\mathbf{r}) = \mathbf{0}\,. \tag{2.49}$$

Solutions are for example plane waves, spherical waves, cylindrical waves, etc[1]. A dielectric material is characterized by a purely real permittivity. Then the solutions of the above equations are non-attenuated waves. So dielectric materials are lossless materials.

2.1.6. Poynting vector and energy density

First we apply the divergence operator on the vector product of **H** and **E** and use the following mathematical identity

$$\nabla\cdot(\mathbf{E}\times\mathbf{H}) = \mathbf{H}\cdot(\nabla\times\mathbf{E}) - \mathbf{E}\cdot(\nabla\times\mathbf{H}). \tag{2.50}$$

On the right hand side of the above equations we apply Eq. (2.1) and Eq. (2.2) including Eq. (2.12) to get

$$\nabla\cdot\left(\mathbf{E}\times\mathbf{H}\right)=-\mathbf{H}\cdot\dot{\mathbf{B}}-\mathbf{E}\cdot\left(\dot{\mathbf{D}}+\sigma\mathbf{E}\right). \tag{2.51}$$

By assuming isotropic linear fields, we can rewrite Eq. (2.51) as

$$\nabla\cdot\left(\mathbf{E}\times\mathbf{H}\right)=-\frac{1}{2}\frac{\partial}{\partial t}\left(\mathbf{H}\cdot\mathbf{B}+\mathbf{E}\cdot\mathbf{D}\right)-\sigma\mathbf{E}\cdot\mathbf{E}\,. \tag{2.52}$$

We look now at the units of the different terms. The argument of the time derivative corresponds to an energy density [J/m^3]. The argument of the divergence operator corresponds to an energy flux per area per time [J/m^{2}s], thus a power flow per area. The last term on the right corresponds to a power density. The physical meaning of the above equation is *energy conservation*. For a dielectric material, the last term vanishes. Then the change of energy density must induce an energy flux. If we allow absorption, the energy flux is decreased by the absorbed energy. The optical oscillations are so rapid (in the order of 10^{14} oscillations per second) that they can't be detected directly. We measure the time averaged fields. Therefore we are interested in the time averaged Poynting vector given by

$$\left\langle\mathbf{S}\left(\mathbf{r}\right)\right\rangle=\lim_{T\to\infty}\frac{1}{2T}\int_{-T}^{T}\mathbf{E}\left(\mathbf{r},t\right)\times\mathbf{H}\left(\mathbf{r},t\right)dt \tag{2.53}$$

which can be simplified in the time harmonic assumption to

$$\left\langle\mathbf{S}\left(\mathbf{r}\right)\right\rangle=\frac{1}{2}\Re\left\{\mathbf{E}\left(\mathbf{r}\right)\times\mathbf{H}^{*}\left(\mathbf{r}\right)\right\}. \tag{2.54}$$

2.1.7. Two dimensional problem

In two dimensions (Fig. 2.1) the waves are propagating in the xz plane and we suppose no variation of the fields and materials in the y-direction, resulting in vanishing of all partial y-derivatives. Then the Maxwell equations (2.35)– (2.38) can be rewritten in component form:

$$i\omega\mu_0 H_x\left(x,z\right)=-\frac{\partial}{\partial z}E_y\left(x,z\right) \tag{2.55}$$

$$i\omega\mu_0 H_z\left(x,z\right)=\frac{\partial}{\partial x}E_y\left(x,z\right) \tag{2.56}$$

---

[1] The widely used Gaussian beam is a solution of the paraxial Helmholtz equation.

$$\frac{\partial}{\partial z}H_x(x,z)-\frac{\partial}{\partial x}H_z(x,z)=j_y(x,z)-i\omega\varepsilon\varepsilon_0E_y(x,z) \tag{2.57}$$

$$j_x(x,z)-i\omega\varepsilon\varepsilon_0E_x(x,z)=-\frac{\partial}{\partial z}H_y(x,z) \tag{2.58}$$

$$j_z(x,z)-i\omega\varepsilon\varepsilon_0E_z(x,z)=\frac{\partial}{\partial x}H_y(x,z) \tag{2.59}$$

$$\frac{\partial}{\partial z}E_x(x,z)-\frac{\partial}{\partial x}E_z(x,z)=i\omega\mu_0H_y(x,z)\,. \tag{2.60}$$

The generalized Helmholtz Eqs. (2.39) and (2.40) reduce in the case where the electric field is entirely described by E_y (TE- or s-polarization) to

$$\frac{\partial^2}{\partial x^2}E_y(x,z)+\frac{\partial^2}{\partial z^2}E_y(x,z)+\hat{\varepsilon}(x,z)k_0^2E_y(x,z)=0 \tag{2.61}$$

and in the case where the magnetic field is entirely described by H_y (TM- or p-polarization) to

$$\frac{\partial}{\partial x}\left[\frac{1}{\hat{\varepsilon}(x,z)}\frac{\partial}{\partial x}H_y(x,z)\right]+\frac{\partial}{\partial z}\left[\frac{1}{\hat{\varepsilon}(x,z)}\frac{\partial}{\partial z}H_y(x,z)\right]+k_0^2E_y(x,z)=0\,. \tag{2.62}$$

2.2. Rigorous grating diffraction theories

2.2.1. Introduction

The structures of interest are basically periodic and the smallest feature sizes are on the order of the wavelength. This excludes most approximate theories such as the scalar approximation [GOO96, BOR93] requiring minimum features size of several wavelengths or effective medium theory [LAL96b] based on maximum feature sizes of a fraction of the wavelength. We use the so-called rigorous diffraction theories. The solutions of these theories satisfy Maxwell's equations. The rigorous methods are often divided into differential, integral, and analytical methods [PET80]. We emphasize on the Fourier Modal Method [BLA99], which belongs to the differential class. This method is similar to the well known Rigorous Coupled Wave Analysis (RCWA) [MOH82].

Most of the present work is done in a two dimensional geometry (i.e. a one dimensional grating). Only a small part is performed with a three dimensional geometry (chapter 5,

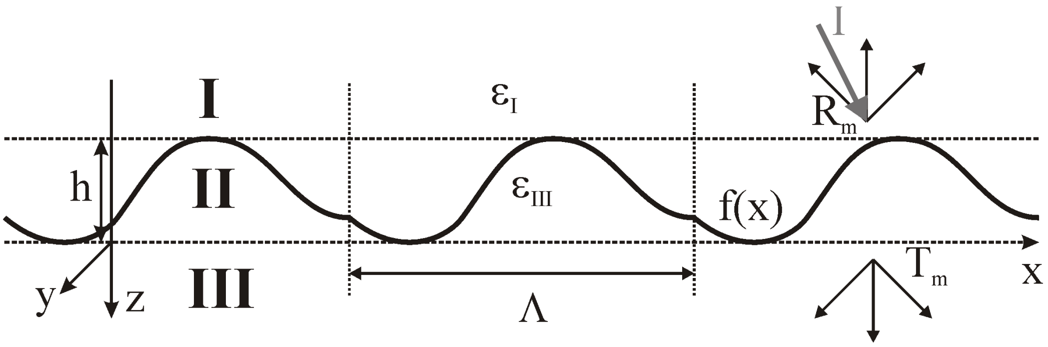

Fig. 2.1: Periodic modulation of the permittivity. The periodically modulated region II is surrounded by two semi-infinite half planes.

polarization dependence). Thus we present in more detail the method for the two dimensional geometry and give only a short introduction concerning the third dimension. When not stated otherwise, we suppose plane wave illumination. The development follows mostly the description of Turunen [TUR97].

Definitions (Fig. 5.1a):

Classical incidence describes the situation where the plane of incidence is perpendicular to the grating grooves, i.e. the conical angle α is zero. In this case, the calculations can be done in two dimensions.

Full conical incidence describes the situation where the plane of incidence is parallel to the grating grooves, i.e. $\alpha=90°$.

Conical incidence describes the general case, but excludes in general the classical incidence case, i.e. $\alpha\neq 0°$.

2.2.2. Grating properties

The solutions of rigorous diffraction methods are solutions of the Maxwell equations. The only approximations are made in the retention of a finite number of modes and the staircase approximation of the permittivity function in the z-direction.

The main property of a grating is its periodicity. The grating function can be described by a strictly periodic function $f(x)=f(x+\Lambda)$, with Λ being the grating period. It is well known that an infinite grating, illuminated by an infinite plane wave, generates a discrete set of propagating plane waves, the diffraction orders.

Consider the following situation (Fig 2.1):

A periodically modulated region II is surrounded by two semi-infinite homogenous regions I and III with corresponding permittivities ε_I, ε_{III}, respectively. A plane wave propagating in the +z direction illuminates the periodic modulated region. Then we get a discrete set of plane waves in transmission $\{T_m\}$ as well as in reflection $\{R_m\}$.

We abstract the problem by introducing U, the field component that appears in the appropriate propagation equation, i.e. $U=E_y$ for TE polarization, $U=H_y$ for TM polarization and use time harmonic fields. The field in region I can be written as a superposition of the incident field U_{inc} and the reflected field U_R. The incident field is assumed to be a plane wave under an angle of incidence (AOI) θ :

$$U_{inc}\left(x,z\right)=\exp\left[ikn_I\left(x\sin\theta+z\cos\theta\right)\right]. \tag{2.63}$$

The field in region III is the transmitted set of plane waves U_T. The Floquet-Bloch theorem [ASH76] states that the solution of a strictly periodic potential, in this case the permittivity, can be written in the form of a strictly periodic function multiplied by a linear phase term. This linear phase term in optics is better known as a plane wave. The product of the periodic function with the plane wave is referred to as a pseudo-periodic function, since its modulus is periodic, but not the function itself. Inside the periodically modulated region II, we can write the field as a superposition of pseudo-periodic functions (or modes). Equation (2.63) is a trivial pseudo-periodic function, a plane wave multiplied by a constant. Since the boundary conditions have to be fulfilled, the diffracted field has to be pseudo-periodic with the same period as the modulated region.

We introduce a periodic function G'

$$G'(x,z)=U_{inc}(x,z)\exp\left(-i\alpha_0 x\right),\quad \alpha_0=kn_I\sin\theta \tag{2.64}$$

which drops the x-dependency of the incident plane wave. This constant function in the x-direction can be seen as a periodic function with any periodicity. Through the boundary conditions and linearity of the equations, the diffracted fields, in transmission as well as in reflection, have to be pseudo-periodic with the same period. The reflected field can be expressed as

$$U_R\left(x,z\right)=G\left(x,z\right)\exp\left(i\alpha_0 x\right). \tag{2.65}$$

A periodic function $G\left(x,z\right)$ can be expressed as a Fourier series with Fourier coefficients $G_m\left(z\right)$. This allows us to express a pseudo-periodic function in a Fourier series:

$$U_R\left(x,z\right)=\sum_{m=-\infty}^{+\infty} G_m\left(z\right)\exp\left(i\alpha_m x\right) \tag{2.66}$$

and define:

$$\alpha_m=\alpha_0+2\pi m/\Lambda, \tag{2.67}$$

where m is an integer.

2.2.3. Field outside the modulated region

In the homogeneous regions I and III Eqs. (2.61) and (2.62) with Eq. (2.46) reduce to

$$\frac{\partial^2}{\partial x^2}U\left(x,z\right)+\frac{\partial^2}{\partial z^2}U\left(x,z\right)+\left(\hat{n}_i k_0\right)^2 U\left(x,z\right)=0, \tag{2.68}$$

where i=I for region I and i=III for region III. We look closer at region III. The diffracted field U_T can be written in the same way as U_R in Eq. (2.66). Inserting the result in Eq. (2.68) gives

$$\frac{\partial^2}{\partial z^2}G_m\left(z\right)+t_m^2 G_m\left(z\right)=0, \tag{2.69}$$

where $t_m^2=\left(kn_{III}\right)^2-\alpha_m^2$. The general solution of Eq. (2.69) is

$$G_m\left(z\right)=T_m\exp\left[it_m\left(z-h\right)\right]+R_m\exp\left[-it_m\left(z-h\right)\right] \tag{2.70}$$

with the sign convention

$$t_m=\begin{cases}\sqrt{\left(kn_{III}\right)^2-\alpha_m^2}, & \text{if } \left|\left(kn_{III}\right)^2\right|>\left|\alpha_m^2\right| \\ i\sqrt{\alpha_m^2-\left(kn_{III}\right)^2}, & \text{if } \left|\alpha_m^2\right|>\left|\left(kn_{III}\right)^2\right|\end{cases}. \tag{2.71}$$

The solution consists of a superposition of a set of plane waves traveling in the +z direction and a set of plane waves traveling in the –z direction. More specifically, T_m and R_m correspond to the complex amplitude of the transmitted and reflected diffraction orders, respectively. If the medium is dielectric, then the wave is not attenuated. Then similar to Eq. (2.66) we treat the solution in region III. Furthermore we suppose that there is no source in region III and thus no wave coming from –infinity, which implies $R_m=0$. We find

$$U_T(x,z) = \sum_{m=-\infty}^{+\infty} T_m \exp\left\{i\left[\alpha_m x + t_m (z-h)\right]\right\}. \qquad (2.72)$$

For region I, the reflected part (without the incident field) can be written as

$$U_R(x,z) = \sum_{m=-\infty}^{+\infty} R_m \exp\left[i\left(\alpha_m x - r_m z\right)\right]. \qquad (2.73)$$

We introduce the new variable r_m which is equivalent to t_m, in Eq. (2.71), but with n_{III} replaced by n_I. If we suppose now only dielectric materials then real values of r_m and t_m correspond to propagating waves and imaginary values correspond to evanescent waves. These plane wave expansions of the reflected and transmitted parts of a periodic scatterer are often referred to as the *Rayleigh expansions* [PET80]. By identification of $\alpha_m = k_0 n_{III} \sin\theta_m$ with Eqs. (2.67) and (2.72) we come up with the grating equation of the mth order

$$n_{III} \sin\theta_m = n_I \sin\theta + m\lambda/\Lambda \qquad (2.74)$$

and similarly for the reflection in region I

$$n_I \sin\theta_m = n_I \sin\theta + m\lambda/\Lambda. \qquad (2.75)$$

With m=0, Eq. (2.74) corresponds to Snell's law, remembering that θ_m is defined in the relevant medium and θ is the angle of incidence in region I.

We are interested in the energy distribution among the different diffraction orders. The diffraction efficiency is given by the normalized energy transfer to the diffraction order of interest. The diffraction efficiency of the order m in reflection and transmission for an incident plane wave with unit amplitude is given by

$$\eta_{R,m} = \Re\{r_m / r_0\}|R_m|^2 \tag{2.76}$$

$$\eta_{T,m} = C\Re\{t_m / r_0\}|T_m|^2, \tag{2.77}$$

with C=1 for TE-, and $C=\left(n_I / \Re\{n_{III}\}\right)^2$ for TM-polarization. The energy transfer is equal to the power flux per unit area. Since the diffracted orders propagate at different angles, the projections have to be taken into account, included in the first term of the right side of the above equations. Note that evanescent waves, characterized by a pure imaginary part of r_m and t_m, do not transfer energy in the z-direction. If we deal only with lossless materials, the principle of energy conservation imposes

$$\sum_{m=-\infty}^{+\infty} \eta_{R,m} + \eta_{T,m} = 1. \tag{2.78}$$

For numerical implementations Eq. (2.78) often serves as a control of convergence, especially to estimate the lowest number of space harmonics that must be retained in the calculation to achieve satisfying results.

2.2.4. Field inside the modulated region

The modulation can be of the surface relief type or of the volume grating type. For both cases we speak of an interface to mark a difference in the refractive index. Then the field inside the modulated structure is expanded into pseudo-periodic eigenmodes. As will be shown, in this approach we can handle only z-independent boundaries. Therefore the modulated region is split into L horizontal slices to approximate the real situation. A discussion of the quality of this approach can be found in [POP02].

First we consider the case of the TE polarization. After a separation of variables $E_y(x,z) = X(x)Z(z)$ and insertion into Eq. (2.61) two ordinary differential equations are obtained;

$$\frac{d^2}{dx^2}X(x) + \left[k_0^2\hat{\varepsilon}(x) - \gamma^2\right]X(x) = 0 \tag{2.79}$$

and

$$\frac{d^2}{dx^2}Z(z)+\gamma^2 Z(z)=0\,, \tag{2.80}$$

where γ^2 is the separation constant. Equation (2.80) has constant coefficients and has the general solution

$$Z(z)=a\exp(i\gamma z)+b\exp\left[-i\gamma(z-h)\right]. \tag{2.81}$$

a and b are constants, which have to be determined by the boundary conditions. Equation (2.79) contains non-constant terms with respect to x. From the Floquet-Bloch theorem we know that E_y and thus X has to be pseudo-periodic, with the same periodicity as ε. Thus we express the permittivity in a Fourier series

$$\hat{\varepsilon}(x)=\sum_{p=-\infty}^{\infty}\varepsilon_p\exp(i2\pi px/\Lambda) \tag{2.82}$$

and search for a pseudo-periodic solution

$$X(x)=\sum_{m=-\infty}^{\infty}P_m\exp(i\alpha_m x) \tag{2.83}$$

with the same definition as in Eq. (2.67). Both expressions are inserted into Eq. (2.79) :

$$\sum_{m=-\infty}^{\infty}\sum_{p=-\infty}^{\infty}\left[\left(\alpha_m^2+\gamma^2\right)\exp\left(i\alpha_p x\right)\delta_{mp}-k_0^2\varepsilon_p\exp\left(i\alpha_{m+p}x\right)\right]P_m=0 \tag{2.84}$$

where δ_{mp} stands for the Kroenecker symbol, i.e.

$$\delta_{mp}=\begin{cases}1, & m=p\\ 0, & \text{otherwise}\end{cases}. \tag{2.85}$$

If we multiply Eq. (2.84) by $\exp(i\alpha_l x)$, with l an integer, and integrate it over a period Λ, we get a system of linear equations, numbered by the same integer l:

$$\sum_{m=-\infty}^{\infty}\left(k_0^2\varepsilon_{l-m}-\alpha_m^2\delta_{lm}\right)P_m=\gamma^2 P_l\,. \tag{2.86}$$

It is convenient to express these linear equations in matrix form

$$\mathbf{MP}=\gamma^2\mathbf{P} \tag{2.87}$$

with the matrix **M** with coefficients

$$M_{l,m} = k_0^2 \varepsilon_{l-m} - \alpha_m^2 \delta_{lm} \tag{2.88}$$

and vector **P** with elements P_m. Equation (2.87) is the equation for a matrix **M** with eigenvector **P** and eigenvalue γ^2. There is no condition on the eigenvalue and thus we can solve for the complete set of eigenvalues γ_n^2 and corresponding eigenvectors $\mathbf{P_n}$. Then the complete solution of Eq. (2.61) is obtained by combining the solutions of Eq. (2.79) and Eq. (2.80)

$$E_y(x,z) = \sum_{l=-\infty}^{\infty} \sum_{n=1}^{\infty} P_{ln} \exp(i\alpha_l x) \left\{ a_n \exp(i\gamma_n z) + b_n \exp(-i\gamma_n (z-h)) \right\}. \tag{2.89}$$

The matrix equation is solved for γ_n^2. Thus the sign of γ_n is not determined and a sign convention is needed: $\Re\{\gamma_n\} + \Im\{\gamma_n\} > 0$.

For TM polarization we assume a separable pseudo-periodic solution for the relevant field component H_y:

$$H_y(x,z) = \left\{ a \exp(i\gamma z) + b \exp\left[-i\gamma(z-h)\right] \right\} \sum_{m=-\infty}^{\infty} P_m \exp(i\alpha_m x). \tag{2.90}$$

In the inhomogeneous Helmholtz equation [Eq. (2.62)] the permittivity is in the denominator and thus we express it as a Fourier series:

$$\frac{1}{\hat{\varepsilon}(x)} = \sum_{p=-\infty}^{\infty} \xi_p \exp(i2\pi p x / \Lambda). \tag{2.91}$$

With the definition of a new function

$$Q(x,z) = \frac{1}{\hat{\varepsilon}(x)} \frac{\partial}{\partial z} H_y(x,z) \tag{2.92}$$

and its pseudo-periodic expansion

$$Q(x,z) = i\gamma \left\{ a \exp(i\gamma z) - b \exp\left[-i\gamma(z-h)\right] \right\} \sum_{m=-\infty}^{\infty} P_m \exp(i\alpha_m x) \tag{2.93}$$

the problem is brought to a more convenient form. The next step is to multiply Eq. (2.92) by $\hat{\varepsilon}(x)$ and insert the pseudo-periodic expansions [Eqs. (2.82), (2.90), and (2.93)] resulting in

$$P_l = \sum_{m=-\infty}^{+\infty} \varepsilon_{l-m} Q_m \ . \tag{2.94}$$

After insertion in Eq. (2.62) we finally get

$$\sum_{m=-\infty}^{\infty} \left(k_0^2 \delta_{lm} - \alpha_l \xi_{l-m} \alpha_m \right) P_m = \gamma^2 Q_l \ . \tag{2.95}$$

In the matrix formalism the above equations are **NQ**=**P** and **MP**=γ^2**Q**. The coefficients of matrices **N** and **M** are $N_{lm} = \varepsilon_{l-m}$ and $M_{lm} = k_0^2 \delta_{lm} - \alpha_l \xi_{l-m} \alpha_m$. Then the following matrix equation can be obtained

$$\mathbf{MNQ} = \gamma^2 \mathbf{Q} \tag{2.96}$$

to determine the eigenvalues. It has to be stated that the hypothesis [Eq. (2.92)] is not unique at all. Equation (2.96) is mathematically correct, but it turns out that there are numerical convergence problems associated with it. Therefore alternative formulations with the same mathematical solution, but different numerical implementations were introduced [MOH95, LAL96a] satisfying the factorization rules of the inverse of the permittivity [LI96]. We use the formulation of [LAL96a] for the classical incidence case[2]. This is not a unique approach. The field can be described by other complete sets of modes or in other coordinates. The best choice of the most efficient method depends on the structure of interest.

2.2.5. Boundary conditions

Expressions for the fields in all three regions were derived. There remain a number of undetermined constants to find by imposing the boundary conditions. In the beginning it was mentioned that with the slicing we get N layers and at each interface the fields have to match. For the sake of simplicity we only take the case of one modulated layer with height h, for example a binary surface relief grating. Then the unknowns are the coefficients for the transmitted and reflected fields T_m and R_m respectively as well as the coefficients a_n and b_n respectively in the solution of Z(z). The boundary conditions Eqs. (2.17)–(2.20) are applied at z=0 and z=h.

[2] Definition of classical incidence given in Sect. 2.2.1.

First we start with TE-polarization, for $U=E_y$. The tangential part of the electric field has to be continuous across the interface. Thus E_y is continuous at the interfaces. At the first interface, the incident field, Eq. (2.63), and the reflected field, Eq. (2.73), have to be matched with the field in the modulated region, Eq. (2.89), at z=0. We get for $l=-\infty,\ldots,+\infty$

$$\delta_{l0} + R_l = \sum_{m=1}^{\infty} \left[a_m + b_m \exp\left(i\gamma_m h\right) \right] P_{lm} . \tag{2.97}$$

At the interface z=h with Eqs. (2.72) and (2.89) we get

$$T_l = \sum_{m=1}^{\infty} \left[a_m \exp\left(-i\gamma_m h\right) + b_m \right] P_{lm} . \tag{2.98}$$

Furthermore Eqs. (2.20) and (2.55) imply that $\partial / \partial z \, E_y \left(x, z\right)$ is continuous across the interface at z=0:

$$r_l \left(\delta_{l0} + R_l\right) = \sum_{m=1}^{\infty} \gamma_m \left[a_m - b_m \exp\left(i\gamma_m h\right) \right] P_{lm} \tag{2.99}$$

and at z=h:

$$t_l T_l = \sum_{m=1}^{\infty} \gamma_m \left[a_m \exp\left(-i\gamma_m h\right) - b_m \right] P_{lm} . \tag{2.100}$$

Then we combine Eq. (2.97) with Eq. (2.99) and Eq. (2.98) with Eq. (2.100) to obtain

$$\sum_{m=1}^{\infty} \left(r_l + \gamma_m\right) P_{lm} a_m + \sum_{m=1}^{\infty} \left(r_l - \gamma_m\right) \exp\left(i\gamma_m h\right) P_{lm} b_m = 2 r_l \delta_{l0} \tag{2.101}$$

and

$$\sum_{m=1}^{\infty} \left(t_l - \gamma_m\right) \exp\left(i\gamma_m h\right) P_{lm} a_m + \sum_{m=1}^{\infty} \left(t_l + \gamma_m\right) P_{lm} b_m = 0 . \tag{2.102}$$

These two equations can be solved for $\{a_n\}$ and $\{b_n\}$ for example by Gaussian elimination. After insertion in Eqs. (2.97) and (2.98) they can be solved for $\{R_l\}$ and $\{T_l\}$.

The solution of the unknown coefficients by the boundary conditions for the TM polarization is very similar to the TE polarization. H_y has to be continuous across the boundary. Then in view of Eq. (2.58) with the definition in Eq. (2.92) and the condition of continuity of the tangential part of the electric field, the function Q has to be continuous across the interface leading to

$$\sum_{m=1}^{\infty}\left(n_I^{-2}r_l P_{lm}+\gamma_m Q_{lm}\right)a_m+\sum_{m=1}^{\infty}\left(n_I^{-2}r_l P_{lm}-\gamma_m Q_{lm}\right)\exp\left(i\gamma_m h\right)b_m=2n_I^{-2}r_l\delta_{l0} \tag{2.103}$$

and

$$\sum_{m=1}^{\infty}\left(n_{III}^{-2}t_l P_{lm}-\gamma_m Q_{lm}\right)\exp\left(i\gamma_m h\right)a_m+\sum_{m=1}^{\infty}\left(n_{III}^{-2}t_l P_{lm}+\gamma_m Q_{lm}\right)b_m=0\,. \tag{2.104}$$

In the general case, when the modulated region is sliced into many layers, then the boundary conditions have to be applied at any intermediate interface. There are efficient implementations with progressive solving.

2.2.6. 1D grating, conical incidence

We considered the problem in the classical incidence with the plane of incidence perpendicular to the grating grooves. The conical case can be regarded as a superposition of TE- and TM-polarization including projection of the incoming grating vector on the grating. Thus the matrices are in general double the size of the matrices for the classical incidence. Details can for example be seen in [MOH95, LAL96a]. Note that in the conical case, polarization mixing occurs and that the outgoing polarization state is generally not the same as the incident one.

2.2.7. 3D geometry and crossed grating

A further extension to structures not constant in y-direction but periodic with period Λ_y can be performed. There are also implementations with oblique Cartesian coordinates to handle crossed gratings at an arbitrary angle. The permittivity has to be developed in a two dimensional Fourier series. The Matlab™ code used in this thesis was programmed by V. Kettunen and is based on the formalism presented in [LI97]. The two dimensional development is much more demanding on computer memory and CPU time. Note that in the literature the number of retained orders is often defined as $N'=(2\cdot N_x+1)\cdot(2\cdot N_y+1)$ with N_x and N_y the retained orders in x- and y-directions, respectively. The computational effort scales with N^3 [LI04]. If N_x=N_y then the computation effort scales with N_x^6. Therefore with today's computers only a few evanescent orders can be retained in the calculations.

3. Resonant Grating Filters

This section consists of several parts. A definition of resonant grating filters and a short historical overview is given in the introduction. Then the general convergence aspects of the Fourier modal method are discussed. After this we concentrate on a special class of resonant grating filters (RGFs), the weak coupling devices. These devices are analyzed in more detail and some rules of thumb are derived. With this knowledge, a design procedure is proposed leading to a RGF named RGF1201, shown in Fig. 3.4, followed by a tolerance analysis. The fabrication process is illustrated. And finally the characterization of the fabricated element is given.

3.1. Introduction

A RGF consists essentially of a combination of a waveguide with a grating. The incident light is coupled by the grating into the waveguide and has to match a mode. There are many degrees of freedom to arrange one or more gratings with one or more waveguides, including additional elements such as thin film layers. Most of the spectrum of the diffracted light does not match a mode of the waveguide. The reflection and transmission can be obtained by using equivalent thin film layers for the calculations resulting in smooth spectral variations. But a small spectral part of the incident light couples to a mode and starts to resonate. This strong resonance effect is associated with strong spectral changes in reflection and transmission. The same class of device has several names in the literature, such as: corrugated waveguide [GOL85], guided-mode resonance filters (GMRF) [SHI98], guided-mode resonant subwavelength gratings (GMRSWG) [BEN01], grating-waveguide structure (GWS) [SHA97]. We call it a resonant grating filter (RGF).

RGF are closely related to one class of grating anomalies. The first grating anomalies were observed about 100 years ago [WOO02]. The abrupt change of reflection of a grating within a very limited range of parameters could not be explained. There are three different groups of anomalies [LOE97]. First the threshold phenomena that are connected to energy redistribution, often found when a diffraction order appears or disappears when changing the angle of incidence or the wavelength. Second, the resonance anomaly that appears by the excitation of guided waves along a corrugated surface. Finally the third case of non-resonant anomalies ("broad" anomalies) with relatively smooth spectral variations. In this work we focus on resonant anomalies, when the light is coupled into waveguides.

Lord Rayleigh tried to explain the discovered anomaly ("Wood's anomaly") by threshold effects [RAY07a], but the predictions did not agree with experimental work. Many years later Fano [FAN41] made the next step in the interpretation, namely the connection with surface wave excitation. It took several more years to get to the today's accepted phenomenological interpretation described by Hessel and Oliner [HES65]. The case of a resonant anomaly without a surface wave was investigated by Nevière [NEV80]. The major difficulty was the mathematical description of a RGF, which has a period smaller than the wavelength and including resonant effects. In the case of a shallow grating and a planar waveguide, accurate results can be obtained by using the Fourier-Rayleigh approximation [RAY07b]. The method fails in the case of deep grooves [WIR80]. Several authors from URSS investigated the reflection from weakly corrugated waveguides [GOL85] as well as [POP86]. The convergence problems of deep grating grooves could be relaxed by using the rigorous Fourier Modal Method (FMM), described in the previous chapter. With the new tools and the appearance of powerful personal computers many new devices were proposed. The potential to design filters with very narrow spectral linewidths in reflection or transmission attracted the attention of many research groups. Magnusson [MAG92] proposed wavelength selective reflection filters and investigated their line shape [DAY96]. He showed the first example of a transmission RGF [TIB97a,b]. Sharon studied RGF with metallic layers [SHA97] and introduced electrical modulation [SHA96]. A remarkable work was done by Peng [PEN96]. He investigated crossed grating RGF in theory and in experiment. He showed near normal incidence a RGF independent of polarization. Note that the coupling mechanism is always polarization dependent. In special configurations, the location of the resonance wavelength for both fundamental polarizations can be the same. There are solutions for a simple grating RGF

[LAC01] as well as for crossed gratings [MIZ01] at oblique incidence. The aspects of polarization independence are discussed in Chapter 5.

3.2. Convergence aspects of FMM

The field as well as the dielectric grating refractive index variations are described by an infinite series in the FMM routines. In the implementation the infinite series have to be truncated. This means only a finite number of orders in the expansions are retained. So we need to know how many orders N need to be used in order to produce good results. Keep in mind that the number of operations scales approximately as N^3, and the memory requirements as N^2. The best way to show this is to take a concrete example, the RGF1201 shown in Fig. 3.4. We consider a wavelength spectrum close to the resonance condition for incident TE-polarization. No resonance is expected for TM polarization. We simply calculate the spectrum for different numbers of retained orders. Then the difference to the spectral reflectance obtained with ±50 retained orders is determined for both polarizations. It is not surprising that the convergence in the resonance domain is slower than away from the resonance as can be seen in Fig. 3.1. In this example in order to have an absolute precision better than 10^{-4} we need to take ±13 orders in the resonance domain and ±7 orders when no resonance is present. Continuous convergence can be observed in both regimes. In the non-resonant domain, the convergence is similar for the whole spectrum.

For the designer it is also important to know the computation time. The same example (RGF1201) is taken and we look at the computation time as a function of the number of retained orders. The solid line in Fig. 3.2 corresponds to the measured calculation time and the dashed line corresponds to the fitted curve. The computer used was an 866 MHz Pentium III. The curve fit is based on a power function

$$f(x) = y_0 + Ax^b, \tag{3.1}$$

with y_0, A and b unknown constants. The best results were obtained with y_0=0.07s, A=9.66 10^{-5}s and b=3.01. The curve fit results confirm the N^3 law.

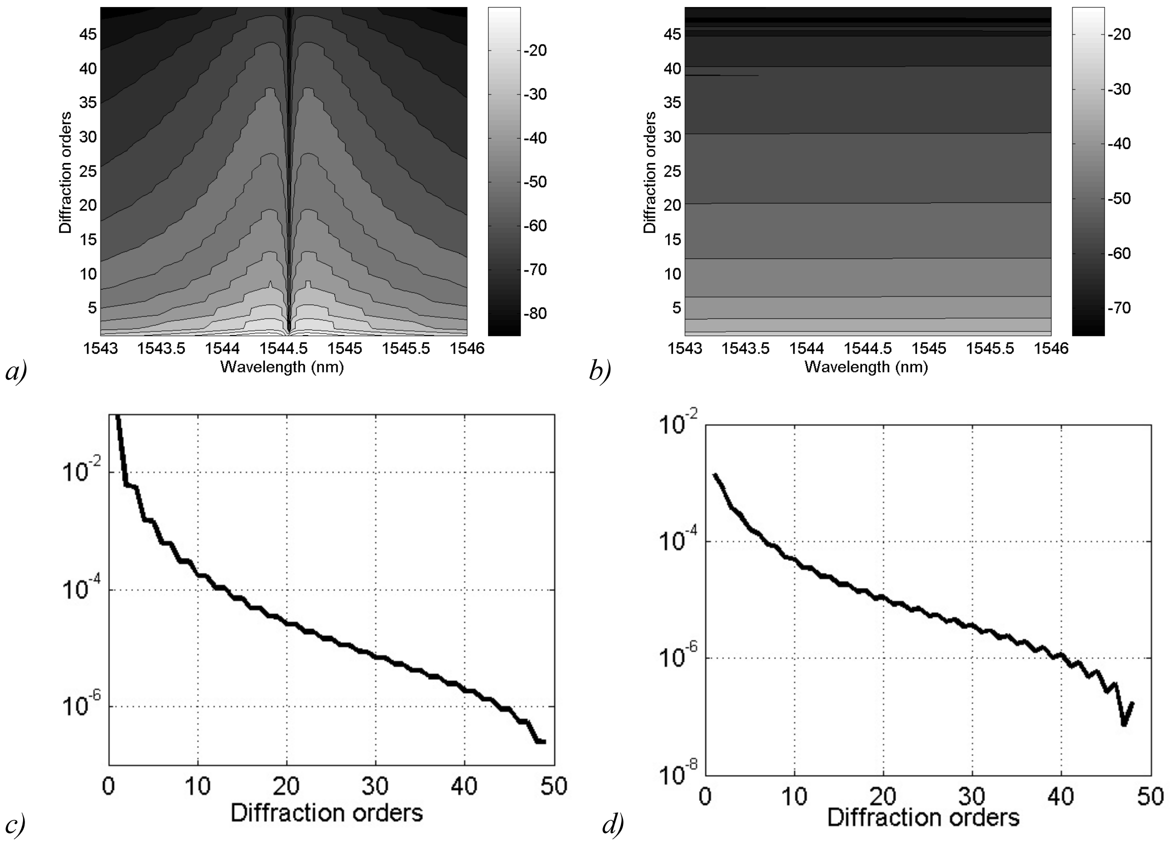

Fig. 3.1. Convergence of the FMM routines. In a) for TE polarization and b) for TM polarization the difference of the reflectance calculated with N orders compared to the reflectivity obtained with ±50 orders is illustrated in a dB scale. In c) and d) a vertical section of a) and b), respectively, at λ=1544.5nm is shown. In TE polarization, a), a resonance occurs at 1544.5nm, whereas in TM polarization, b), no resonance occurs and the convergence is independent of the wavelength over the range shown.

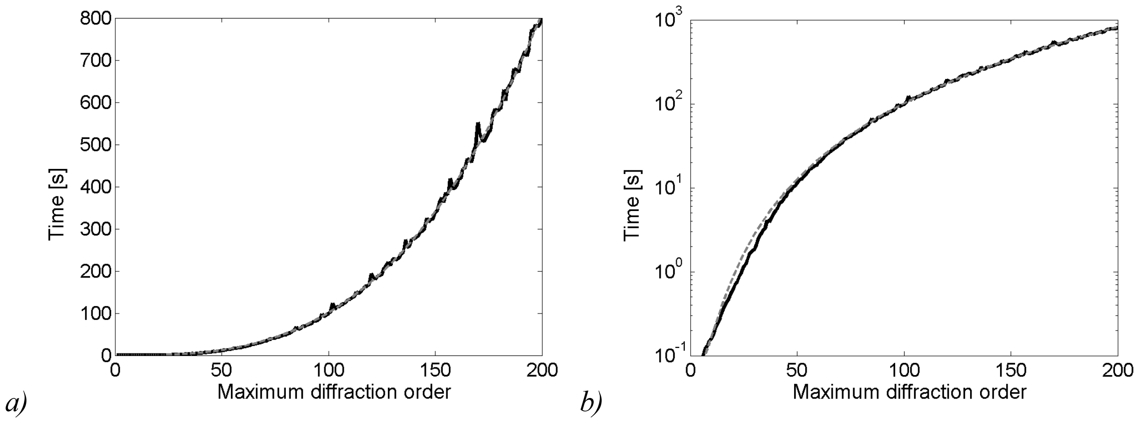

Fig. 3.2: Calculation time per iteration as a function of truncation order: a) in linear scale and b) in logarithmic scale. The solid line is the measured elapsed time and the dashed line corresponds to the curve fit $t = y_0 + A * N^b$*, with* $y_0 = 0.07$*s,* $A = 9.66\ 10^{-5}$*s and* $b = 3.01$*.*

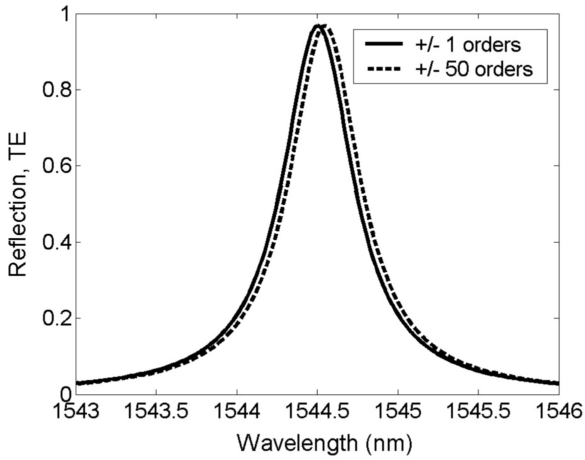

Fig. 3.3: Spectral reflectance of the RGF1201. The solid line is obtained with ±1 retained orders and the dashed line is obtained with ±50 retained orders.

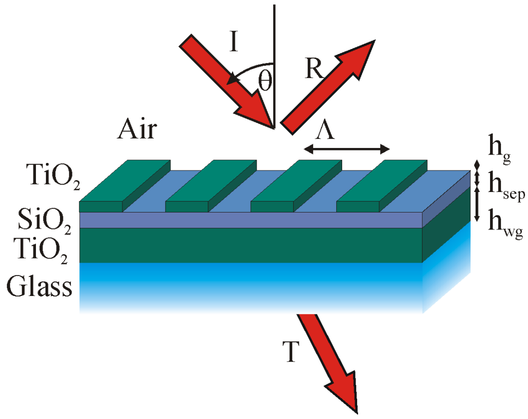

Fig. 3.4: Three layer stack consisting of a waveguide (TiO_2) on a glass substrate covered by the separation layer (SiO_2) with a grating (TiO_2) on top. With n_{TiO2}=2.298, n_{SiO2}=1.444, n_{Glass}=1.51 and n_{air}=1.00, h_{wg}=287nm, h_{sep}=146nm, h_g=38nm, Λ=592nm and the fill factor ff=0.515.

It is helpful to know the coupling mechanism of the device to be designed. In the case of the RGF1201 we have only propagating specular orders outside the structure. Through coupling by the -1^{st} diffraction order of the grating we can excite the fundamental mode of the buried waveguide. Thus the redistribution of the energy happens between the specular orders and the -1^{st} order in the waveguide. Thus if we consider only up to the $\pm 1^{st}$ orders we can already observe a resonance. This resonance peak is close to the real peak, in position and in width, as shown in Fig. 3.3. It is clear that the Fourier series describing the dielectric distribution of the grating (Eq. 2.82) truncated after the first order, cannot take into account the exact shape of the grating. As additional evanescent orders are retained in the calculation the exact solution is approached. A sufficient precision can be obtained when retaining only a few evanescent orders in the calculation routine.

In conclusion, in order to find the resonance location for this class of devices, it is sufficient to take a few evanescent orders into account. But for accurate results (better than 10^{-6}) it is necessary to calculate using a considerable number (±45) of evanescent orders.

3.3. Common properties of the three layer stack with a shallow grating (weak coupling)

The goal of this section is to show the dependence of the spectral response of the RGF on several geometrical and optical parameters. In this section we limit the analysis to weak coupling devices. The coupling force depends on several factors, one of them is the grating height: the shallower the grating the weaker the coupling. The shallow grating in our case, when considered in the thin element approximation, generates a maximum phase difference of far less than π. Furthermore the waveguide modes are only weakly affected by shallow gratings. The stronger the coupling the worse the following approximations apply. As shown subsequently, the obtained rules of thumb work fine when applying them to the example of the RGF1201 (Fig. 3.4). This element consists of a high index layer, the waveguide, covered with a low index layer and a grating on top.

3.3.1. Fourier series of the rectangular dielectric function

The coupling power of the grating and the resonance width are related. We wish to look more closely at the coupling power of shallow gratings. The coupling power depends on the modal field as well as on the structure. We will limit the development to the structure. The shallow grating is described by a Fourier series of the dielectric material in the FMM. Within this formalism, complicated grating structures are horizontally sliced into rectangular or binary gratings. So we look more closely at rectangular gratings. Normally the first diffraction order of the grating is used to couple the incident light into the waveguide. Then the first coefficient of the Fourier series is the most important. In this case the coupling strength is proportional to the square of the relevant Fourier coefficient. First we calculate the first Fourier coefficient and can then directly see its dependencies.

We suppose the dielectric function to be real (non absorbing materials). A rectangular grating can be centered to be an even function without effect on the coupling strength. In this case the Fourier coefficients are real and we will not need complex numbers in the integrals.

The Fourier series of a periodic function with complex coefficients is

$$f(x) = c_0 + \sum_{k=-\infty}^{+\infty} c_k e^{ik2\pi\frac{x}{\Lambda}}, \quad c_k = \frac{1}{\Lambda}\int_{-\Lambda/2}^{+\Lambda/2} f(x) e^{ik2\pi\frac{x}{\Lambda}} dx \tag{3.2}$$

and equivalently with real coefficients

$$\begin{aligned} f(x) &= \frac{a_0}{2} + \sum_{k=1}^{+\infty} a_k \cos(2\pi kx/\Lambda) + \sum_{k=1}^{+\infty} b_k \sin(2\pi kx/\Lambda) \\ a_k &= \frac{2}{\Lambda}\int_{-\Lambda/2}^{+\Lambda/2} f(x)\cos(2\pi kx/\Lambda)dx, \quad b_k = \frac{2}{\Lambda}\int_{-\Lambda/2}^{+\Lambda/2} f(x)\sin(2\pi kx/\Lambda)dx. \end{aligned} \tag{3.3}$$

The coefficients are related through

$$\left.\begin{aligned} c_k &= \frac{1}{2}(a_k - ib_k) \\ c_{-k} &= \frac{1}{2}(a_k + ib_k) \end{aligned}\right\} k > 0 \qquad . \tag{3.4}$$
$$c_0 = \frac{1}{2}a_0$$

We assume we have a rectangular grating with two permittivities ε_1 and ε_2. The relative fraction consisting of ε_2 is called the fill factor (ff) and thus the remaining fraction (1–ff) is ε_1. The non-zero Fourier coefficients describing this rectangular grating are then

$$a_k = 2(\varepsilon_2 - \varepsilon_1)\frac{\sin(\pi \, ff \, k)}{\pi k} \tag{3.5}$$

$$c_{-k} = c_k = a_k / 2 . \tag{3.6}$$

In the case where the first Fourier coefficient (k=1) is dominant we can make two observations since the resonance width is expected to be proportional to the square of that Fourier coefficient [ROS97]:

- The expected line width is proportional to $\sin^2(ff\ \pi)$. A numerical verfication of this statement is given in Fig. 3.5, where we have excellent agreement between the normalized width and the inferred relationship as a function of the fill factor of the rectangular grating.

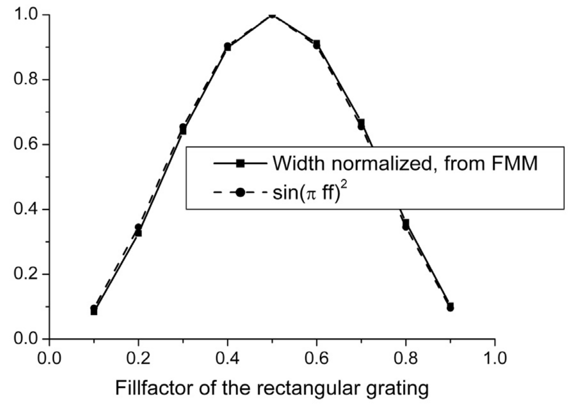

Fig. 3.5: Influence of the fillfactor (ff) on the relative linewidth. The solid line is obtained with FMM calculations, normalized by the width resulting with ff=0.5. The dashed line corresponds simply to the $sin^2(\pi*ff)$ formula.

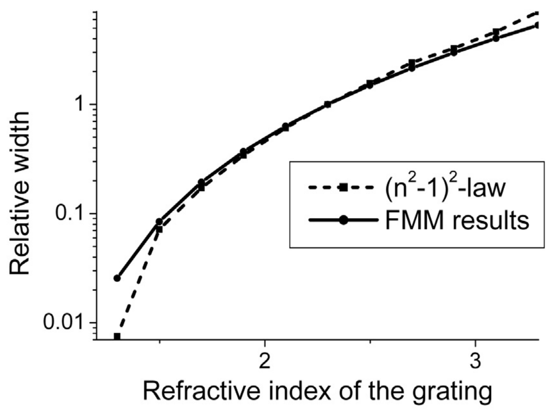

Fig. 3.6: Resonance width as a function of the refractive index of the grating (high index material). The low index material is air (n=1.0). The solid line corresponds to the relative width obtained with FMM and is compared to the approximation formula (dashed line).

- A second estimation is that the resonance width is proportional to $\left(\varepsilon_2-\varepsilon_1\right)^2$ which can be rewritten $\left(n_2^2-n_1^2\right)^2=\left(n_2+n_1\right)^2\left(n_2-n_1\right)^2=4n_{av}^2\Delta n^2$. A numerical comparison of this law and the FMM results is shown in Fig. 3.6.

It must be mentioned that the solution of truncating after the 1st orders cannot be exact. The Fourier series of a rectangular grating truncated after the first order corresponds to a sinusoidal grating.

3.3.2. Influence on the grating height, "Quadratic grating height rule"

The grating height has a strong influence on the coupling strength of the grating (Eq. 4.13). We can take advantage of previous work published on grating couplers [RIG76], based on the so-called Rayleigh-Fourier approximation [BLA99]. This approximation is exact for homogeneous layers, but not for structured layers. It turns out that this approximation is identical to the assumption of a shallow grating. The radiation loss coefficient is a measure of

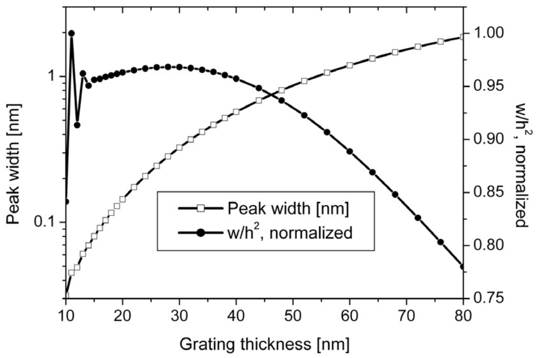

Fig. 3.7: Numerical verification that the resonance width scales with the square of the grating height.

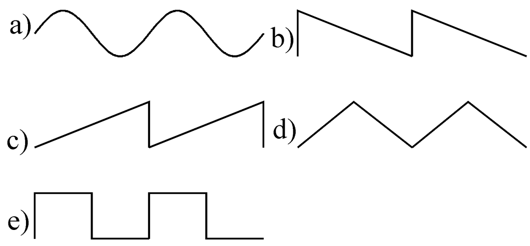

Fig. 3.8: Different grating shapes: a) sinusoidal grating, b) asymmetric triangular grating 1, c) asymmetric triangular grating 2, d) symmetric triangular grating, and e) rectangular grating.

the coupling strength and directly related to the resonance width. In this model the resonance width is proportional to the square of the grating height. This can be confirmed with rigorous calculations, see Fig. 3.7. We can state a good correlation between the approximation and rigorous theory. For thicker gratings we can see that the width increases less than predicted by the approximate model.

3.3.3. Influence of the grating shape

Here we wish to study the influence of the grating shape on the filter performance, while maintaining the height h_g and the period Λ of the grating constant. We consider 5 different grating shapes, shown in Fig. 3.8 and determine their resonance width and location. All gratings, including the rectangular grating, where divided into 100 rectangular slices and calculated with ±11 retained orders. The results are given in Table 3.1. In the last section, we saw a dominant contribution from the first coefficient of the Fourier series and that the resonance width is proportional to the square of the height. In the fifth column of the table the first Fourier coefficient c_1 is given. h is the grating height. When comparing the normalized width and the normalized square of the Fourier coefficient we can observe an excellent agreement. Since the coupling strength of the shallow grating is proportional to the square of the first Fourier coefficient, grating b) and grating c) have the same coupling strength. This result is surprising from the perspective of classical diffractive optics, involving blazed

Grating	λ_c [nm]	w [nm]	w, normalized	c_1	$(c_1/c_{1r})^2$
a) 	1544.70	0.322	0.621	$h/2$	0.617
b) 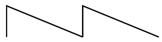	1544.75	0.131	0.252	h/π	0.25
c) 	1544.70	0.130	0.252	$-h/\pi$	0.25
d) 	1544.75	0.213	0.411	$4h/\pi^2$	0.405
e) 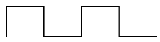	1544.50	0.518	1	$2h/\pi$	1

Table 3.1: Resonance location λ_c and resonance width w of the RGF1201 (Fig. 3.4) for different gratings with the same height h=38nm. In order to show the dependence of w on the square of the 1^{st} Fourier coefficient c_1, the square of the ratio of the first coefficient for the grating of interest and its counterpart for the rectangular grating is reported. An excellent agreement can be observed. Since we look at the square, the sign of the coefficient has no influence.

gratings, and highlights the importance of the resonant coupling to the functionality of the device.

3.3.4. Phase shift at a resonance

The relative phase of the transmitted, reflected and incident waves has a huge impact on the reflection and transmission. The relative phase shift is responsible for constructive or destructive interference in transmission and reflection. In some situations it is necessary to look at the resulting phase shifts for a correct interpretation of the spectral reflectance.

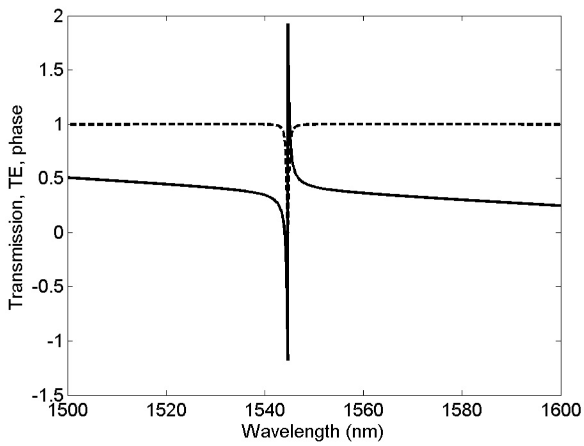

Fig. 3.9: Phase in radians of the 0^{th} transmitted order of the RGF1201 device. The solid line is the phase and the dashed line corresponds to the transmittance.

The phase associated with the complex reflection or transmission coefficient is in general rather complex to interpret. The

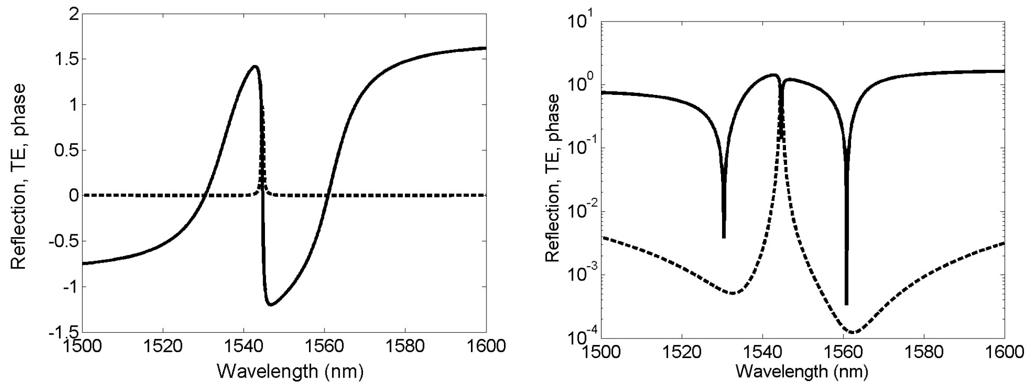

Fig. 3.10: Phase of the 0^{th} reflected order of the RGF1201 device in linear and logarithmic scale. The solid line is the phase (absolute value in the logarithmic scale) and the dashed line corresponds to the reflectance. We still have the abrupt change at the resonance. There is a second more slow change of the phase, without a dramatic redistribution of energy.

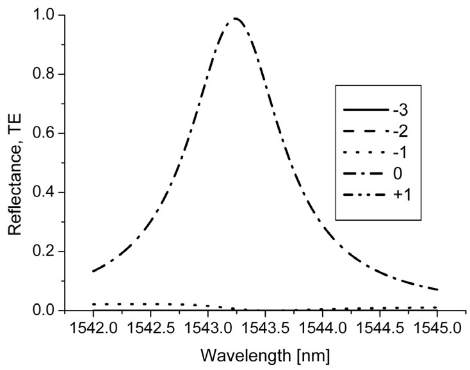

a)

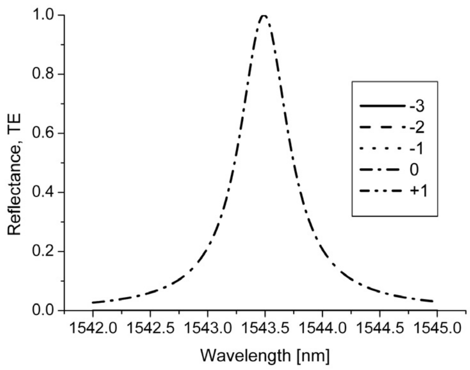

b)

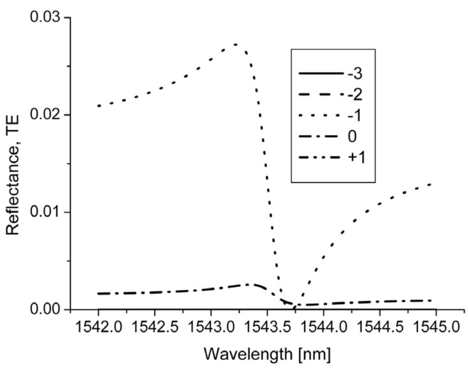

c)

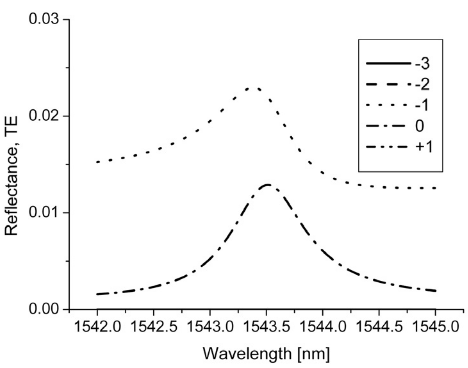

d)

Fig. 3.11: Reflectance of the $+1^{st}$ through -3^{rd} diffraction orders as a function of the coupling in order. The grating period is adjusted to fulfill different resonances: a) $+1^{st}$ order resonant, Λ=1291nm, b) -1^{st} order resonant, Λ=591.5nm, c) -2^{nd} order resonant, Λ=1183nm, and d) -3^{rd} order resonant, Λ=1774nm.

phase unwrap algorithm has to be applied with care because of the periodicity of the phase. In this section we just wish to show the phase shift associated with a resonance. Because of this phase shift, energy transfer is possible. A phase shift of 180° can change from destructive to constructive interference, or vice versa. So it is possible to design transmission RGFs [TIB96a,b].

Then, in the absence of a resonance, the RGF should behave as a mirror. This requires more dielectric layers than a good transmitter. The resonance peak shape becomes asymmetric when the out of resonance reflection or transmission curve is not symmetric.

Fig. 3.9 shows the phase as well as its corresponding square modulus of the RGF1201 (Fig. 3.4) of the transmitted zeroth order and Fig. 3.10 shows the reflected zeroth order. It can clearly be seen that there is a π-phase shift at the resonance in transmission and reflection. A slow second phase change can be observed in reflection. The interpretation is difficult. A possible explanation is a smooth change of the sign, more clearly visible with the logarithmic scale.

3.3.5. Higher order designs

Here we wish to look at the design freedom of choosing the grating diffraction order. The initial design was made to excite the waveguide mode using the -1^{st} diffraction order. Then no other orders propagate outside the structure. The waveguide stays single mode for the range of wavelengths of interest. The grating period is adjusted to use other grating diffraction orders for coupling in. Additional propagating diffraction orders can emerge. We look specifically at the -3^{rd}, -2^{nd}, and $+1^{st}$ coupling order and examine their interaction with the propagating orders. The reflectance and the corresponding phase of the orders around the resonance are plotted in Fig. 3.11 and Fig. 3.12 respectively. The grating periods are 1774nm for the -3^{rd} order, 1183nm for the -2^{nd} order, 591.5nm for the -1^{st} order, and 1291nm for the $+1^{st}$ order. From the two figures we can see that the device works well for the -1^{st} and $+1^{st}$ grating diffraction orders. But for the other two cases the element behaves different. By using the 2^{nd} order, a phase shift of twice 180° is added, so its effect essentially cancels. One would expect that the 3^{rd} order should work. But in this case one should notice that the light can couple out via all the propagating orders and the interaction of the incident wave and the light

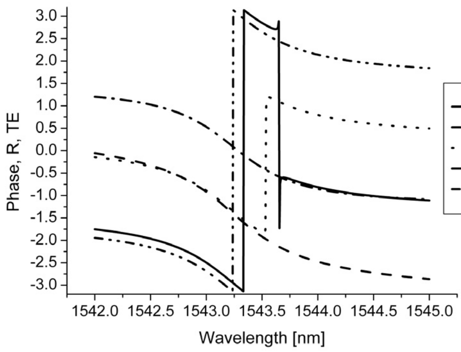

a)

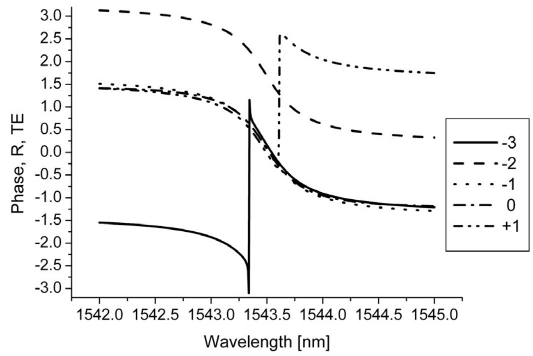

b)

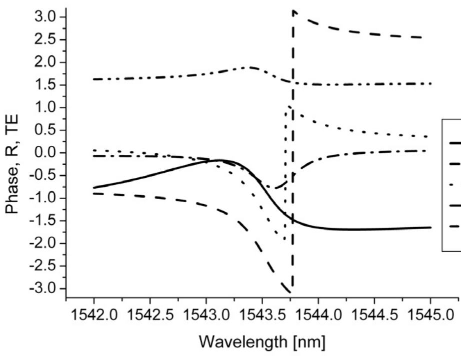

c)

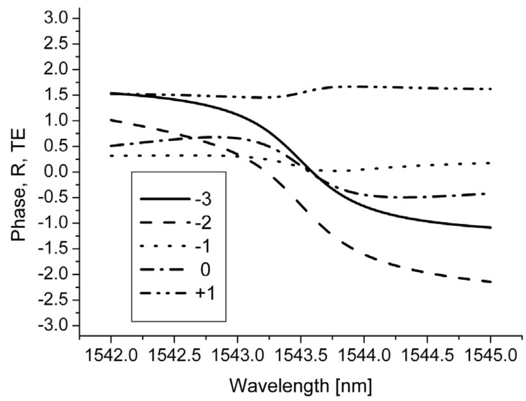

d)

Fig. 3.12: For completeness we show the phases corresponding to the reflectance of the +1^st^ through –3^rd^ diffraction order as a function of the coupled order. The grating period is adjusted to fulfill different resonances: a) +1^st^ order coupling in, Λ=1291nm, b) –1^st^ order coupling in, Λ=591.5nm, c) –2^nd^ order coupling in, Λ=1183nm, and d) –3^rd^ order coupling in, Λ=1774nm.

coupled out through the 3rd grating diffraction order is no longer dominant. So as a conclusion the device works best for the 1st grating diffraction orders.

3.4. Design

Our design goal is a device that shows a narrow band reflection at a given wavelength with a given spectral width. In addition we want to realize a tunable device. This should be realized in a simple way using standard technology and standard materials.

Of course, there is no unique solution to this problem. Many approaches can lead to the desired device. Resonant grating filters can offer narrow spectral linewidths and tuning capabilities. The tuning is performed by changing the illumination angle. We wish to maintain the shape of the spectral reflection peak over the whole tuning range. A good solution is obtained with a device having a constant linear dispersion, i.e. the resonance wavelength to illumination angle relation. The dispersion relation of a simple grating is locally linear around 45° AOI. The same applies for a planar dielectric waveguide. We emphasize the fact that we need a *locally* linear dispersion relation, since the relative change of the wavelength to cover the C-band is only ±1.3%. If the mode in the waveguide is affected by the presence of the grating, the dispersion relation changes. Associated with this variation is the fact that the resonance strength changes. We can observe therefore that the change of the shape of the spectral reflection peak is smaller in the case of weak coupling devices. They only induce a weak perturbation of the waveguide mode.

The kind of problem we are looking at in general does not offer a unique, analytical solution as well as no single way to obtain a solution. We present an approach which is fast and simple. The design process simplifies greatly if we use some a priori knowledge and start with a good initial guess of the parameters. First we give a short overview of the design process and then we present step by step the design of the RGF1201.

The design process, based on a resonant grating filter (Fig. 3.4) can be divided into several steps:

1) Select the structure (layers, materials, angle of incidence, wavelength).

2) Fix a "reasonable" grating height h_g as an equivalent homogenous layer.

3) Solve for the thicknesses h_{sep}, h_{wg} to fulfill AR conditions.

4) Determine the grating period Λ to achieve resonance at the desired wavelength.

5) Change the grating height h_g to get the desired FWHM.

6) Numerical optimization.

We discuss the design procedure for the following design goals: Tunable reflection filter with a peak width of 0.5nm. The tuning range is the C-band and the center tuning angle is 45°.

3.4.1. Select the structure

We choose the so-called three layer stack as our starting point for the design which can easily be fabricated and integrated in the system (Chapter 1). The three layer stack consists of a high index material forming the waveguide on a substrate, covered by a low index material with a shallow grating on top (see Fig. 3.4). We choose the following materials: glass for the substrate (n=1.51), TiO_2 as the high index material (n=2.298), and SiO_2 as the low index material (n=1.444). The grating is made of the high index material, in order to reduce the number of materials being involved. In this configuration the low index material separates the grating and waveguide. In the following we call this layer separation layer. It also forms an etch stop when etching the grating. Our design wavelength is 1545nm, corresponding to the center of the C-band. The grating shape, as shown in the previous chapter, changes the coupling strength, but does not give additional degrees of freedom. Therefore, we choose the most suitable grating shape for computation, which is the rectangular grating profile. This grating shape is also suitable for straightforward fabrication.

3.4.2. Fix a "reasonable" grating height h_g, as an equivalent homogenous layer

The subwavelength grating is not only a coupling element, but behaves similar to a thin film layer as well. The reflection of the RGF can be seen as coming from two sources: for most of the spectrum, the reflectance can be described by equivalent thin film layers and only a small part of the spectrum is dominated by the resonance effects. We denote *thin film reflection* when only looking at the first kind of reflection. For example by changing the grating period, the resonance reflection peak position is affected, but the thin film reflection stays approximately the same. In this and the next point we want to minimize this thin film reflection. So the grating is replaced by an equivalent homogeneous layer. The equivalent layer in s-polarization is simply the same layer thickness with the refractive index according to the zeroth order effective medium theory

$$n_{eff,TE} = \sqrt{ff\ n_H^2 + \left(1 - ff\right) n_L^2}\ , \tag{3.7}$$

with ff being the fillfactor, the fraction of the rectangular grating with the high index material n_H, sometimes also called the dutycycle. The zeroth order effective medium theory is sufficient to give a good starting point for the rigorous optimization routines in point 6. The grating height heavily changes the resonance width (Sect. 3.3.2). Therefore the grating height is not chosen as a free parameter to find the minimum of reflection. We fix the grating height for the following step. A good initial guess requires some design experience, but can also be obtained in an iterative way.

In our case the high and low index materials of the grating are TiO_2 and air. We start with *ff=0.5*, resulting in an effective refractive index of $n_{eff}=1.77$. We fix a starting height h_g of *40nm*.

3.4.3. Solve for the thicknesses h_{sep}, h_{wg} to fulfill AR conditions

The thicknesses of the waveguide and the separation layer are adjusted to minimize the thin film reflection at a given wavelength and AOI. There is not only one solution, but there are periodic solutions. Furthermore it is easier to grow thin layers to achieve a given absolute tolerance. An example of the dependence of the reflectance on the thicknesses of the waveguide and the separation layer with the grating replaced by a homogeneous layer of thickness 40nm and effective refractive index of 1.77 is given in Fig. 3.13. The reflectance is a periodic function of the thicknesses. A numerical optimization reveals in TE polarization the two fundamental solutions, a) h_{wg}=283.3nm, h_{sep}=151.2nm, and b) h_{wg}=69.9nm, h_{sep}=310.3nm. The thicknesses of the different minima differ by an integer multiple of half the wavelength in the medium of concern. Therefore we refer to thin film orders. These solutions are not equal in terms of tolerances. The spectral reflectance of the fundamental

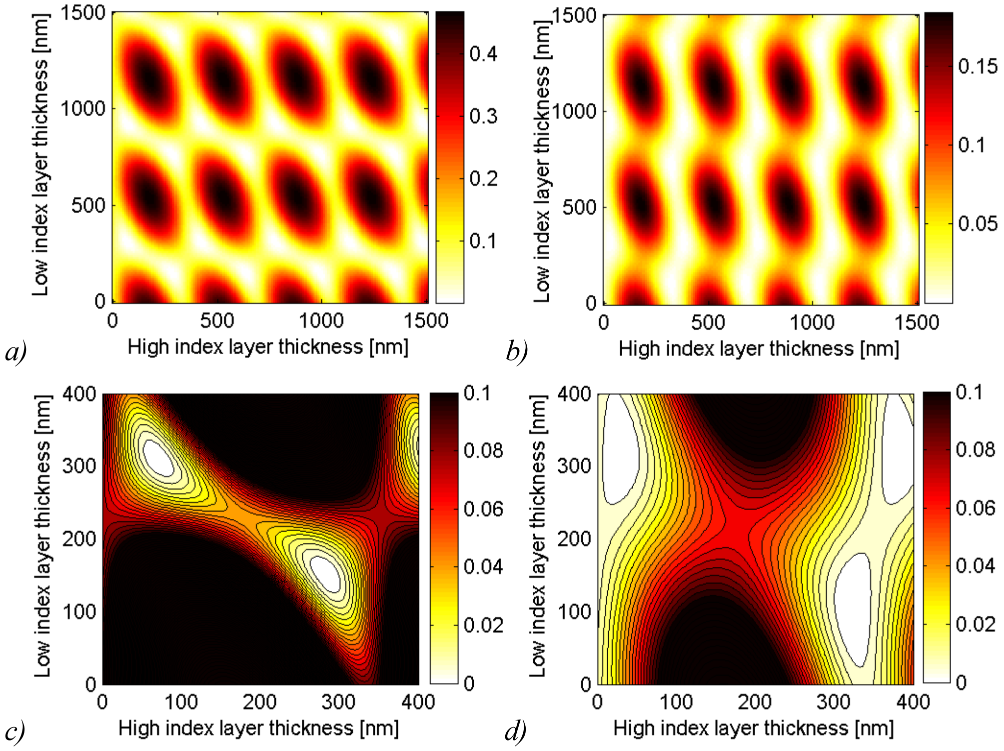

Fig. 3.13: Reflection as a function of the waveguide (high index) and separation layer (low index) thicknesses, on the left for TE polarization and on the right for TM polarization. A zoomed contour plot of the first row is shown in the second row. The contour interval is 0.005. For both polarizations there are two periodic minima of reflection.

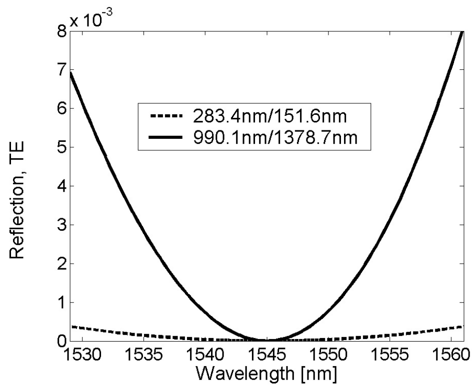

Fig. 3.14: Reflection spectrum of two structures fulfilling AR conditions for λ=1545nm. The dashed line corresponds to the fundamental reflection minimum and the solid line corresponds to the third order (in both directions) reflection minimum.

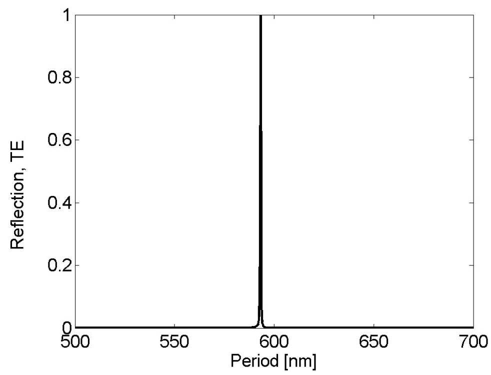

Fig. 3.15: Grating period determination. The reflectance as function of the grating period, shows a sharp peak, where the resonance occurs (Λ=593.2nm).

minimum (h_{wg}=283.3nm, h_{sep}=151.2nm) and its 3rd order minimum (h_{wg}=990.1nm, h_{sep}=1378.7nm) is shown in Fig. 3.14. A difference in the reflection curvature around the minima can be seen. It is advantageous to take the fundamental minimum to maximize the tuning range. We continue with the solution h_{wg}*=283.3nm,* h_{sep}*=151.2nm*.

3.4.4. Determine the grating period to achieve resonance at the desired wavelength

Now we consider the grating coupling property. The grating period is adjusted to bring the resonance to the desired wavelength (λ=1545nm). Therefore in the calculations we replace the homogeneous layer with the original grating. Then, as described in section 4.1, the appropriate grating period to couple into the waveguide mode is estimated. With this starting point, the exact grating period for coupling is determined with FMM. With the above values we find from Fig. 3.15 a grating period of *593.2nm*.

3.4.5. Change the grating height to get the desired FWHM

After the above steps, the thin film reflectivity and the resonance locations are optimized. But probably the resonance width differs from the target width. Therefore we apply the rule of Sect. 3.3.2, predicting that the resonance width scales with the square of the grating height. It is known that RGF with symmetrical sidebands (thus working in a thin film reflection minimum) have a Lorentzian peak shape [NOR96, ROS97]. Therefore we use Lorentzian curve fit routines to determine the exact peak position and width, in order to become more independent of the chosen calculation grid. The resonant grating filter with the above-determined parameters has its peak position at 1544.95nm with a full width at half maximum (FWHM) of 0.57nm. In this case the height has to be divided by a factor of $(0.57\text{nm}/0.50\text{nm})^{1/2}$=1.07 resulting in a new grating height of *37.5nm*.

3.4.6. Numerical optimization

For the optimum solution we apply numerical methods (Nelder-Mead simplex method, using Matlab™). The deviation between the actual spectral curve and the design curve shape is minimized by adjusting the thicknesses, the grating period and the grating fill factor. In order to ensure convergence of the algorithm, the starting point has to be chosen with the resonance near the desired location. The function to be minimized is a weighted sum of the difference of the actual curve and the target curve. So, different weightings lead to slightly different solutions. Several combinations have to be calculated to achieve a good solution. For the RGF1201 we obtained the following parameters:

	"exact" value	**rounded value**
Grating height h_g	38.000nm	38nm
Separation layer height h_{sep}	146.166nm	146nm
Waveguide thickness h_{wg}	286.596nm	287nm
Grating period Λ	592.276nm	592nm
Fillfactor ff	0.515	0.515

We added a column for "rounded value" because from the numerical perspective it would be possible to come very close to the optimum solution. But as can be seen in Sect. 3.6, it makes no sense to give values significantly more precise than it is possible to fabricate. For the rest of the analysis we just use the rounded values, although the peak position and width are slightly different, namely λ_{res}=1544.63nm, FWHM=0.519nm, instead of the target values λ_{res} =1545nm, FWHM=0.5nm.

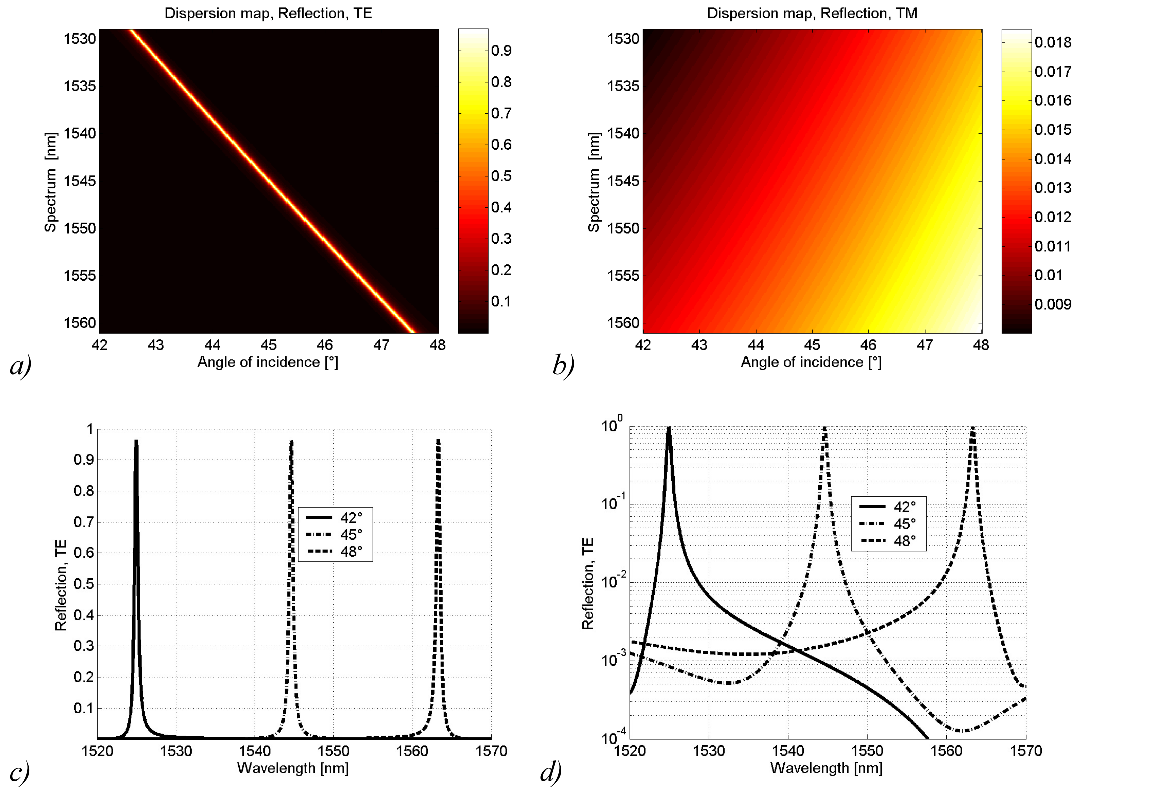

Fig. 3.16: Dispersion maps of the RGF1201, a) in TE polarization and b) in TM polarization. c) and d) are sections of a) in linear and logarithmic scale, respectively. In the region of interest, there is no resonance for TM polarization.

3.5. Tuning

The resonance wavelength depends on the angle of incidence (AOI). The best way to show this tuning potential is to show the dispersion maps, the reflectivity as a function of the angle of incidence and the wavelength. A sharp change of the reflectivity corresponds to a resonance[3]. Working around 45° offers the advantage of convenient separation of the incident and reflected beam. A grating coupler and a planar waveguide offer a locally linear dispersion relation. So if they can be treated as separate elements (shallow grating approximation), then their resulting dispersion relation is locally linear as well. This can be numerically confirmed by comparing the dispersion relation with rigorous methods (Fig. 3.16) and within the waveguide-grating coupler model (Fig. 4.2) of the RGF1201. In the figure we can see only

[3] A sharp change of reflectivity can also occur when a propagating order is emerging. In our case we work in the 0^{th} order region, where no propagating orders, other than the specular one exist.

one resonance. The dispersion relation is approximately linear with a slope of 6.4nm/°. A closer look, however, reveals a local slope variation from 6.7nm/° at 42° to 6.1nm/° at 48°. Furthermore, it can be seen that the resonance line shape stays almost constant over the whole tuning range, but its width changes from 0.472nm at 42° (λ_{res}=1525.0nm) to 0.543nm at 48° (λ_{res}=1563.4nm).

3.5.1. Aspects of normal incidence

Many publications considered normal incidence illumination. However, we find that there are several advantages to design a device for operation at oblique incidence. A first argument is that additional devices (e.g. a circulator) are needed to separate the incident and reflected beams. Furthermore around normal incidence we get crossed resonance lines, the –1st and +1st order coupling, making it impossible to have only one adjustable resonance wavelength (Fig. 3.17). But additional effects occur. When looking closer at the crossing lines in Fig. 3.17b), the dispersion map is symmetric with respect to a change of the AOI, but not for the wavelength. So we expect non-constant relation between the angular and spectral width around resonance. Furthermore at exactly normal incidence the grating necessary for coupling into the waveguide acts additionally as a Bragg reflector. Thus the propagation length within the waveguide is reduced (reduced broadening of the reflected beam). At normal incidence the angular tolerance is relaxed, since the situation is symmetric with respect to the incident angle. It is possible to add a second grating with twice the period of the fundamental grating to reduce further the angular tolerance by maintaining the spectral width [LEM98]. The situation at perfect normal incidence corresponds to a degenerated state. When the AOI is reduced close to zero we would expect gently crossing lines (Fig. 3.17a). At oblique incidence it is logical that two modes can be excited through coupling by the –1st and +1st grating diffraction order, having different propagation directions and propagation constants. At normal incidence the two modes coincide (same wavelength). By approaching normal incidence the two modes start to couple. This leads to a change in the dispersion at normal incidence, forming a band gap. Figure 3.17a) does not reveal the details shown in Fig. 3.17b). For higher order modes in multimode waveguides, this effect is even more pronounced with a larger gap, when the symmetry of the mode changes.

At normal incidence the spectral resonance shape changes with the angle of incidence. Close to normal incidence two resonances can occur and it is even possible to have a band gap, thus no resonance for a certain wavelength. Given these factors a simpler device can be realized when working at non-normal incidence.

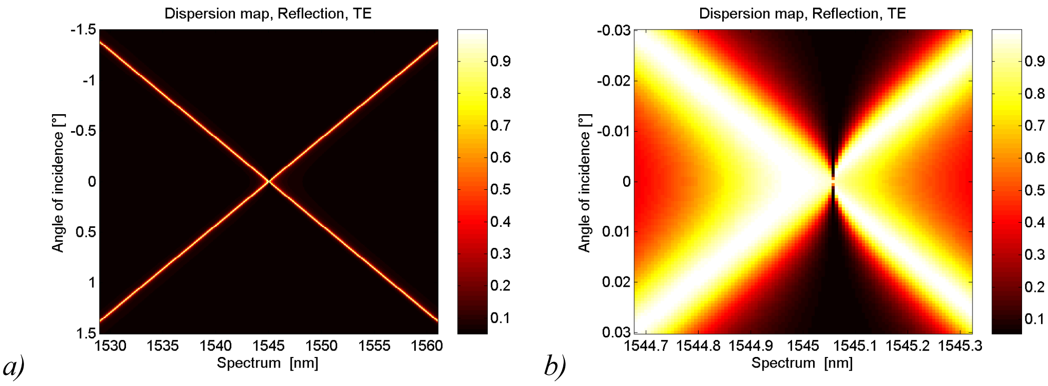

Fig. 3.17: Dispersion maps of the RGF1201b, optimized for working around normal incidence. In a) the crossing resonance lines can be observed. The zoom of the intersection b) reveals the mode coupling at normal incidence.

Parameter	*Design*	*+3% on λ_{res}*	*+3% on FWHM*
Period	592nm	2.62	7.81
n_{TiO2}	2.298	1.96	5.86
AOI	45°	0.55	3.28
h_{wg}	287nm	0.36	–6.86
$n_{substrate}$	1.51	0.22	–4.73
n_{SiO2}	1.444	0.13	2.35
fill factor	0.513	0.01	–0.51
h_g	38nm	0.00	5.87
h_{sep}	146nm	0.00	–4.09
Incomplete etching by	3nm	–0.01	–14.83
Overetching into SiO_2 by	3nm	0.00	0.20

Table 3.2: Tolerancing of different design variables. The resulting percentage change of the resonance wavelength λ_{res} and the resonance width FWHM by increasing the design parameter in column two by 3% is reported in the 3rd column and the last column respectively. Values below 3% indicate an attenuation of the relative error on the optical response, whereas values above 3% indicate an amplification of the error. The device with the rounded design parameter shows a FWHM of 0.519nm at 1544.6nm at an angle of incidence of 45°.

3.6. Fabrication tolerances

For the fabrication and characterization of the device, it is important to know how the deviation of the design parameters influences the optical response of the device. Only a few papers [HEG00, SHI98], evaluated the consequences of fabrication errors on filter performance. We take the rounded values obtained in Sect. 3.3.6, leading to λ_{res}=1544.63nm and FWHM=0.519nm. The influence of the errors of the different design parameters on the resonance wavelength λ_{res} and on the resonance width FWHM is given in Table 3.2. The design values are given in column 2 and the results of increasing these values by 3% on the peak wavelength λ_{res} and the peak line width FWHM are given in columns 3 and 4, respectively.

In this table it can be seen that the 3% change in the period and the refractive index of the waveguide have the largest relative effect on the peak wavelength. However the grating period can be controlled very well, on the order of 0.01%. In contrast, the refractive index of the waveguide material depends on the deposition process and varies on the order of 1%. So it becomes the largest uncertainty for the peak position. The relative precision of the fill factor is only on the order of 10%, but due to its small influence, this parameter can be neglected.

The influence of the parameters on the peak width is different, mostly larger. In many cases the relative errors are amplified, needing good control over the various parameters. Under error amplification we understand that a relative change of 3% of the design parameter induces a relative change of the resonance width by more than 3%. Fortunately, in the case of statistically distributed errors, some errors with opposite effects on the peak width may cancel out.

The advantage of the tunable device is that a peak wavelength shift due to fabrication errors can be compensated by adjusting the tilt angle. This can be observed in the measurements (Fig. 3.24).

3.6.1. Losses by absorption

The loss of the waveguide structure is the amount of light not guided further. Since the lost amount of light is proportional to the total amount of the guided light, it can be described by an exponential decay constant, characterized by a total loss coefficient, α_{tot}. The total loss coefficient can be written as the sum of the different loss coefficients, the scattering losses α_{sc}, the radiation losses α_{rad} and the absorption losses α_{abs}. Assuming smooth interfaces, in this work we shall neglect scattering losses. The radiation loss coefficient describes the interaction strength between the incident light and the light in the planar waveguide through the grating and is therefore proportional to the resonance line width of the structure [AVR89]. In our application we need a selective structure, i.e. a weak

Im(n)	*[dB/cm]*	*FWHM [nm]*	*R_{max} [%]*
0	0	0.517	100
1e–6	0.35	0.518	99.7
2e–6	0.71	0.519	99.4
5e–6	1.77	0.521	98.4
1e–5	3.53	0.526	96.8
2e–5	7.06	0.535	93.7
5e–5	17.66	0.561	85.3
1e–4	35.32	0.604	73.7

Table 3.3: Peak reflection efficiency of an infinite device as a function of the absorption loss coefficient α of the waveguide material.

coupling device. The radiation loss coefficient for this class of devices is given in Chapter 4. Rigorous calculations show that in the absence of absorption and scattering the peak reflection of resonant grating filters can reach 100% [MAS85]. The unwanted loss is caused by absorption and given by the absorption loss coefficient. This coefficient is directly related to the imaginary part of the refractive index $\alpha_{abs}=4\pi/\lambda\,\Im\{n\}$. Qualitatively it can be said that if the absorption loss coefficient is much smaller than the radiation loss coefficient, then the device works as intended. Furthermore this means that very selective devices, with a small radiation loss coefficient, are more sensitive to absorption. A quantitative overview in the case of the RGF1201 (Fig. 3.4) of the reflection efficiency in the presence of absorption of the waveguide is given in Table 3.3. There we can see that an absorption of 1dB/cm still leads to a maximum reflectivity of more than 99% and almost no peak broadening.

3.6.2. Line shape asymmetry

A deviation from the optimum value often results in a deformation of the resonance line shape, making it more asymmetric. If the resonance takes place where the element with the homogeneous layer would show a reflection extremum, the resonance line shape is symmetric. By moving out of this optimum situation, the line shape is affected. An example is given in Fig. 3.18. The thin film reflectivity is a periodic function of the inverse of the wavelength. Then the RGF1201 is taken and the period is adjusted to bring the resonance position to the desired wavelength.

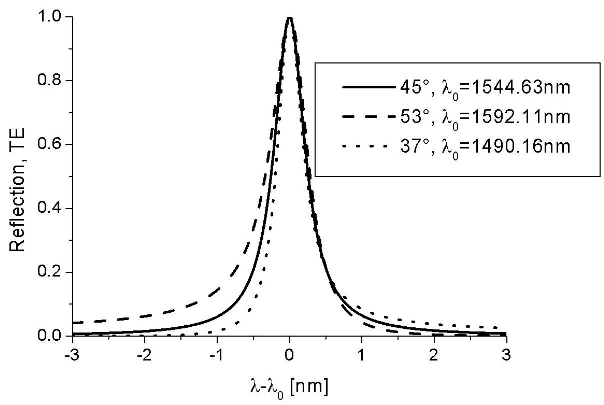

Fig. 3.18: Line shape asymmetry. When the incident angle is changed, the corresponding spectral resonance shape deteriorates.

3.7. Fabrication

The RGF was fabricated by our project partner, the CSEM in Zürich, and consists of three successive process steps (Fig. 3.19):

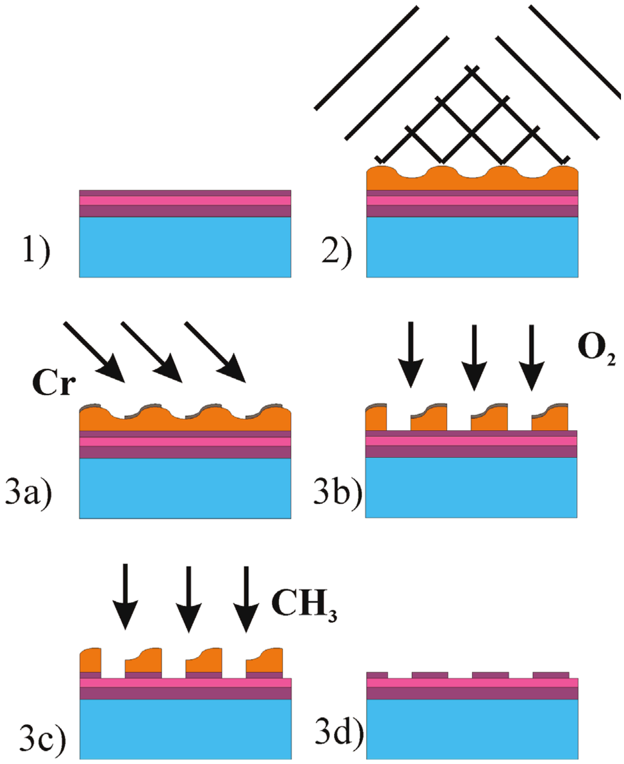

Fig. 3.19: Grating fabrication. 1) Deposition of the layers, 2) holographic lithography, and 3) grating etching

1) The **deposition** of the SiO_2 and TiO_2 layers is done by DC Magnetron sputtering. Optical monitoring is used to control the layer thicknesses. This is a standard procedure and allows the deposition of the layers with ±3% tolerance in optical thickness.

2) **Holographic lithography** is used to generate a grating structure on the layer stack. For patterning of the grating structure the layer stack is coated with photoresist. A HeCd -Laser beam (λ=441.6nm) is split into two beams which interfere on the coated substrate to expose a linear grating with the desired periodicity of 592nm. Development of the photoresist results in a photoresist grating structure with a sinusoidal profile. The accuracy of the grating period is better than 0.1nm.

3) To **transfer** this **grating** into the topmost waveguide layer, chromium is slope evaporated onto the photoresist grating at an angle of incidence smaller than 45°. By careful adjustment of the angle of incidence and chromium layer thickness it is possible to generate a chromium grating (Fig. 3.19, step 3a) with the same period and with a fill factor of 0.5 [SCH02]. Subsequent etching of the resist (3b) with O_2 and of the upper waveguide layer (3c) with trifluoromethane (CHF_3) generates the desired rectangular grating structure in the waveguide layer. Finally the remaining resist and chromium is removed (3d). The final grating tolerances are defined by the achievable tolerances of the process steps. The fill factor of the slope evaporated chromium grating is determined by the angle of incidence and amount of

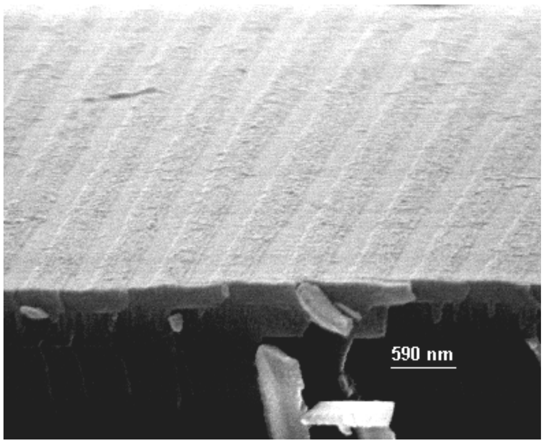

Fig. 3.20: Scanning electron microscopy (SEM) picture of the fabricated grating.

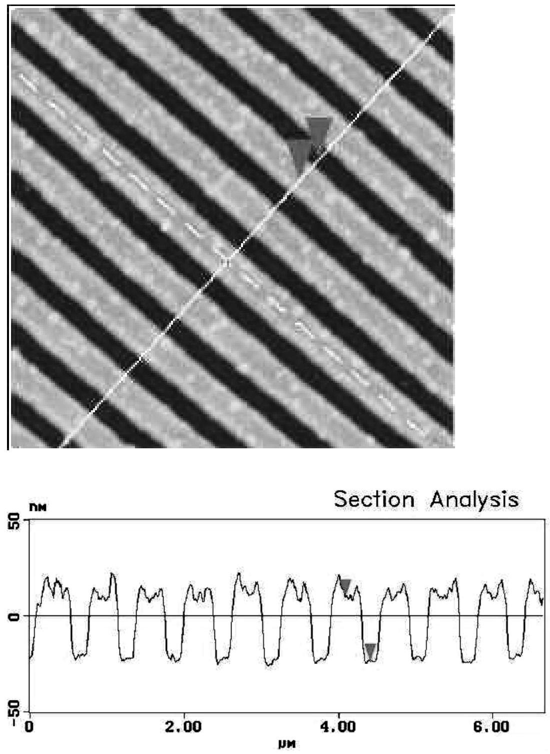

Fig. 3.21: Atomic force microscopy (AFM) picture and profile of the grating structure, revealing an average grating depth of 35±2nm

chromium deposited, as well as the precision and depth of the photoresist sinusoidal grating. Practical tolerances are in the range of ±10%. The grating depth is determined by the etch rate of CHF_3 in the grating layer material.

As the material composition of TiO_2 (porosity) is not only critical for the refractive index of the layer but also for the etch rate, experiments for the particular TiO_2 layer have to be performed to evaluate the exact etch rate.

Figure 3.20 shows a scanning electron microscope (SEM) picture of the final grating, which has a fill factor of slightly larger than 0.5 and a still relatively rough TiO_2 surface. The corresponding atomic force microscope (AFM) picture (Fig. 3.21) of the same structure reveals a grating depth of 35nm, close to the targeted 38nm.

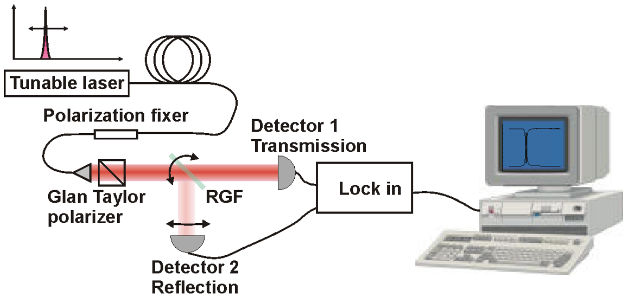

Fig. 3.22: Measurement setup. The light from the tunable laser source goes through polarization controllers and after collimation impinges on the RGF. The transmitted and reflected light is directly measured by means of two detectors.

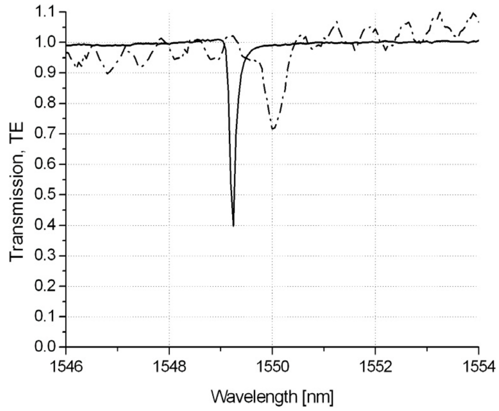

Fig. 3.23: Measured transmissivity of the device with the shallow (depth 12nm) grating. Measured a) with a large collimator (8mm, solid line) at an angle of incidence of 49° and b) a small (1mm, dash-dotted line) collimator at an angle of incidence of 49.3°. The values are normalized to the offset of the Lorentzian curve fit. It is clear that in a) the hole is deeper and narrower than in b). Due to the measurement setup, b) shows undesirable Fabry-Perot interference fringes.

3.8. Measurements

The diced filter sample was attached via index-matching oil to a wedge prism of 2° to avoid parasitic Fabry-Perot interference fringes. The assembly was mounted on a precision rotation stage. The whole device is illuminated with a collimated beam from a modulated tunable laser source, HP8168 (Fig. 3.22). For each angle of incidence a measurement series is made by changing the wavelength. The transmitted and reflected beam intensities are simultaneously measured by two detectors. Only the specular orders propagate outside of the device. So it is possible to measure a spectrum under a certain AOI without readjusting the detectors. The orientation of the grating can easily be determined when illuminating with a visible laser and observing the -1^{st} diffraction order.

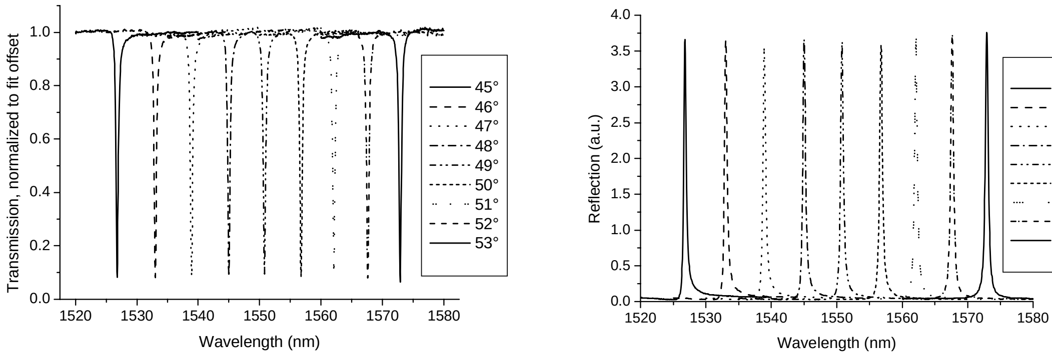

a) *b)*

Fig. 3.24: Measured transmission (a) and reflection (b) spectra of the device with 35nm grating depth. The transmission is normalized to the offset of the Lorentzian curve fit. The fit results are presented in Table 3.4. The collimator used for the measurements is specified to have a beam diameter of 8mm and the sample size was one inch square.

	Reflection			*Transmission*		
angle	λ_{res}	w	R_{max}	λ_{res}	w	ΔT_{max}
45	1526.80	0.40	3.71	1526.80	0.39	0.94
46	1533.04	0.43	3.74	1533.01	0.41	0.94
47	1538.92	0.44	3.59	1538.90	0.43	0.92
48	1545.01	0.45	3.72	1544.99	0.42	0.93
49	1550.80	0.46	3.71	1550.78	0.43	0.93
50	1556.77	0.47	3.64	1556.74	0.44	0.93
51	1562.10	0.47	3.68	1562.09	0.43	0.91
52	1567.63	0.48	3.79	1567.61	0.45	0.94
53	1572.93	0.49	3.88	1572.89	0.43	0.97

Table 3.4: Lorentzian curve fit results of the measured reflection and transmission spectra at different angles of incidence shown in Fig. 3.24. The angle is the incidence angle in °, λ_{res} the peak reflection wavelength and w the FWHM, in nanometers. R_{max} is the peak reflection [a.u.] and ΔT_{max} is the drop in transmission, relative to the offset. The average slope between 45° and 53° AOI is 5.8nm/°.

Experimental measurements were performed on two filters with different grating depths. The first filter sample has a grating depth of only 12nm instead of the design value of 38nm. This results in a narrower and asymmetric resonance peak and a higher out of resonance reflectivity. It should be mentioned that we used a Lorentzian fit to determine the width of the resonance peak, even if the line shape was (slightly) asymmetric. Rigorous calculations show that the line width for the shallower grating drops from 0.52nm to 0.052nm without absorption or to 0.061nm with α_{abs}=0.8cm^{-1}, accompanied by a significant drop in peak efficiency (from 100% to 75%). Assuming a slope of 6nm/°, the spectral width of 0.06nm corresponds to an angular width of 0.01°. The maximum peak efficiency [Eq. (4.11)], in this case for λ=1545nm and w=0.5mm, is only 10% and for w=4mm it is 56%.

To investigate the filter performance for different filter sizes and different divergence angles of the collimated beam, the sample with 12nm grating depth was measured with both, a) a large collimator (2w=8mm) and b) a standard (2w=1mm) collimator. The results are shown in Fig. 3.23, where w is the beam waist of the collimator. Since there is an uncertainty in the normalization of the reflected beam, the transmission spectra were taken and normalized by the offset of their Lorentzian curve fit. The drop of the measured peak from the fit was a) 63.5% and b) 30.0% with corresponding width FWHM a) 0.12nm and b) 0.33nm. The predicted lower peak efficiency and its broadening are observed. The drop in the transmission spectrum includes not only the reflected part, but the absorbed and the scattered part as well, which explains that the drop is larger than predicted by theory.

The parameters of the other filter sample were closer to the design parameters with a grating depth of 35nm, leading to the results shown in Fig. 3.24 and summarized in Table 3.4. This shows that tuning over the full C-band is feasible. The calculated peak reflection wavelength for the device with 35nm grating depth is 1544.4nm and the peak width is 0.44nm. The efficiency could be improved, close to the designed shape. The reflection peak under 45° AOI occurs at λ=1526.8nm instead of 1545nm with a line width of 0.40nm. The average tuning slope is 5.8nm/° for the range 45°–53°. The shift towards shorter wavelengths, as well as the slight asymmetry, which diminishes for larger angles of incidence, can mainly be attributed to a smaller refractive index of the waveguide material than assumed in the design. Therefore we simulated the transmission spectrum for an AOI of 45° with a lower index of refraction of TiO2, namely n_{TiO2}=2.259. The measured and simulated curves are shown in Fig. 3.25. The peak shift can be compensated by an additional tilting of 3.0° with no significant effect on the line shape.

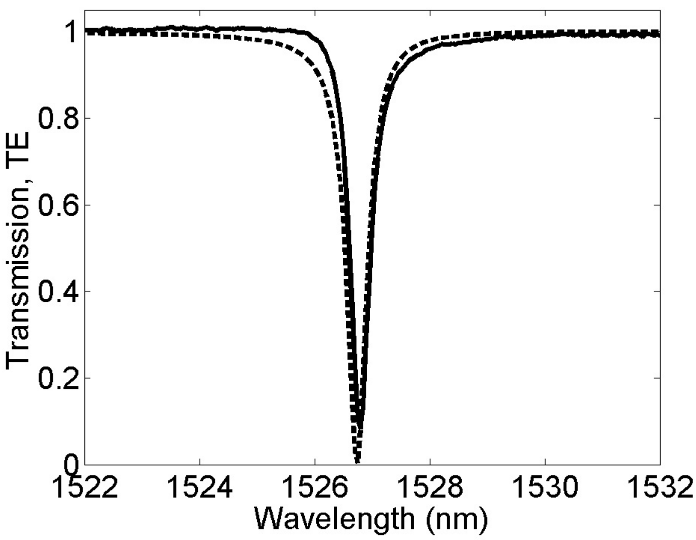

Fig. 3.25: Comparison between measurements and simulation. The measured values (solid line) from Fig. 3.24 for 45° AOI are compared with the simulated values (dashed line), with n_{TiO2} *changed to 2.259*

4. Approximate Models

Rigorous methods give accurate results and are able to predict the field distributions. However they are very slow, memory- and time-consuming. Therefore we present in this chapter a simple model based on the unperturbed waveguide mode with an infinitely shallow grating for approximate resonance prediction, as well as mode identification. In addition wave vector diagrams are introduced. They are useful for the interpretation of rigorous simulations. Another model is introduced with the goal of predicting the losses of finite devices, where the involved lengths exceed the maximum computational window of rigorous methods. In chapter 6 some of these results are compared with results obtained using rigorous methods.

4.1. Simple waveguide and infinite shallow grating model

Using the simple model presented below we hope to obtain a good approximate design for optimization using rigorous methods, as well as to obtain more physical insight into the functioning of the device. The model consists of an infinite thin grating, separated from a planar waveguide by a low-index separation layer as shown in Fig. 4.1. Thus, in this approximation, we assume that the mode shape of the waveguide is affected neither by the grating nor by the finite thickness of the separation layer. The separation layer is chosen with a lower refractive index to give good

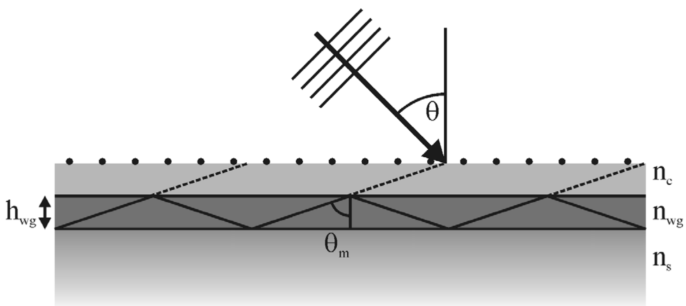

Fig. 4.1: Simplified coupling model. An incoming plane wave is coupled into a waveguide mode. The mode is assumed not to be affected by the grating and the finite thickness of the cover (separation layer).

confinement in the waveguide, resulting in evanescent coupling of the incoming light into the waveguide.

First we introduce the condition for a waveguide mode and combine this with the grating equation. The grating and the waveguide are treated as separate elements. We start with the well known equations [KOG79] of a planar waveguide (self-consistency or transverse resonance condition):

$$h_{wg} k_0 n_{wg} \cos(\theta_m) - \phi_c - \phi_s = m\pi \tag{4.1}$$

with the effective index n_e of the mode defined as

$$n_e = n_{wg} \sin(\theta_m)\,. \tag{4.2}$$

h_{wg} is the waveguide thickness, k_0 the wave number in vacuum, n_{wg}, n_s and n_c are the respective refractive indices of the waveguide, the substrate and the cover. θ_m is the propagation angle in the waveguide, ϕ_c and ϕ_s are the phase shifts induced by total internal reflection at the cover and the substrate, respectively, and m is the order of the mode. The phase of the total internal reflection depends on the polarization, leading to a polarization dependence of the device. The conditions for single mode operation (m=0) of the planar waveguide (cutoff conditions), supposing $n_s>n_c$, are

$$\mathrm{TE}: \frac{h_{wg}}{\lambda} \leq \frac{1}{2\pi\sqrt{n_{wg}^2 - n_s^2}} \arctan\left(\frac{n_s^2 - n_c^2}{n_{wg}^2 - n_s^2}\right) + \frac{1}{2\sqrt{n_{wg}^2 - n_s^2}} \tag{4.3}$$

$$\mathrm{TM}: \frac{h_{wg}}{\lambda} \leq \frac{1}{2\pi\sqrt{n_{wg}^2 - n_s^2}} \arctan\left(\frac{n_{wg}^4}{n_c^4}\frac{n_s^2 - n_c^2}{n_{wg}^2 - n_s^2}\right) + \frac{1}{2\sqrt{n_{wg}^2 - n_s^2}}\,. \tag{4.4}$$

For a given configuration and mode number (m) the corresponding TM wavelength is always smaller than for TE, because $n_{wg} > n_c$.

The grating coupler is governed by the following equation:

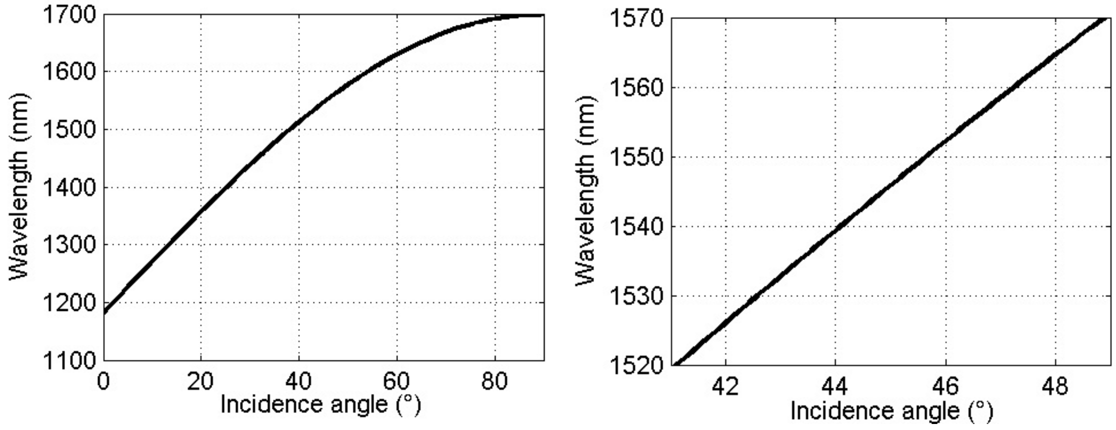

a) *b)*

Fig. 4.2: Scalar dispersion map a), including a magnified view of the region of interest b). The simulation parameters are: M=–1, m=0, h_{wg}=287nm, n_{wg}=2.298, n_s=1.51, n_c=1.444, and TE polarization.

$$\frac{\Lambda}{\lambda_0}\left[n_{wg}\sin\left(\theta_m\right)-n_{in}\sin\left(\theta_{in}\right)\right]=M, \tag{4.5}$$

with Λ being the grating period, λ_0 the wavelength in vacuum, n_{in} the refractive index of the incoming medium, θ_{in} the angle of incidence in that medium and M the diffraction order. $n_i \sin(\theta_i)$ is a conserved quantity in Eq. (4.5), imposed by Snell's law. In our case we couple to the backward propagating fundamental mode of the waveguide, which means that the sign of the angle in the waveguide, θ_m, is negative corresponding to the -1^{st} diffraction order (M=–1). We are interested in having only the 0^{th} propagation order outside the waveguide to prevent unwanted diffraction losses. This is true when

$$\Lambda \le \frac{\lambda_0}{n_{in}\sin\left(\theta_{in}\right)+\max\left(n_{in},n_{out}\right)}. \tag{4.6}$$

The coupled Eqs. (4.1) and (4.5) cannot, unfortunately, be solved in a closed form, and must be solved numerically. By fixing the geometry, the refractive indices of the materials, the mode number, m, and the diffraction order, M, we find, for every incidence angle, a corresponding resonance wavelength, as long as the boundary conditions [Eqs. (4.3), (4.4), (4.6)] are fulfilled. This leads to a typical λ-θ map (dispersion map with λ, the resonance wavelength and θ, the corresponding AOI), valid for a specified polarization. The λ-θ map for

M=–1, m=0, h_{wg}=287nm, n_{wg}=2.298, n_s=1.51, n_c=1.444 and TE polarization is shown in Fig. 4.2. For small variations of the incidence angle θ around 45° the relation between the wavelength and the angle of incidence is quite linear (right plot). The waveguide in this example stays single mode for TE polarization for thicknesses in the range of 53nm to 455nm. Using Eq. (4.6), it can be shown that there are no propagating orders other than the specular orders when the period is smaller than 654nm or 905nm, with substrate material glass or air respectively.

4.2. Wave vector analysis

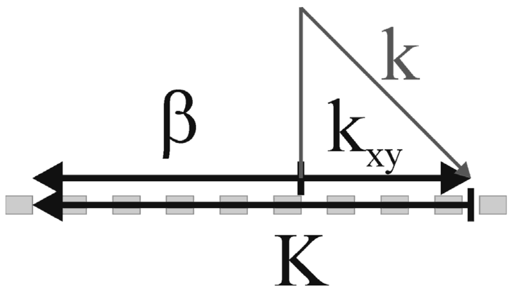

Fig. 4.3: Wave vector analysis in the classical mount. The projection $\boldsymbol{k}_{xy}$ *of the incident wave vector k and the grating vector* ***K*** *are added and must match the waveguide mode vector* $\boldsymbol{\beta}$ *for coupling. With angle of incidence θ=45°, wavelength λ=1545nm, angle in the mode* θ_m*=55.9°, and period 592nm, we see that Eq. (4.7) is fulfilled.*

Only the basic concepts of wavevector analysis are outlined to facilitate the comprehension of coupling in RGF. They are extensively used in crystal analysis in solid state physics [ASH76]. A plane wave is characterized by its wavevector, **k**, with modulus 2πn/λ, the wave number in the medium and its orientation is along the direction of propagation. A grating is characterized by its grating vector **K**, with length 2π/Λ, Λ being the grating period. The orientation is perpendicular to the grating grooves. In a RGF, the grating vector of the surface relief grating is parallel to the underlying planar waveguide. The guided wave is characterized by its wavevector β with magnitude $2\pi n_{eff}/\lambda$ and direction along its propagation direction. The effective index of a guided wave is smaller than the real index of refraction of the guided material. The coupling condition, Eq. (4.5), can be illustrated by the summation of the k-vectors in the grating plane (Fig. 4.3). This is equivalent to the following equation:

$$|\boldsymbol{\beta}| = |\mathbf{K}| - |\mathbf{k}_{xy}| \Leftrightarrow \frac{n_{wg}\sin(\theta_m)}{\lambda} = \frac{1}{\Lambda} - \frac{\sin(\theta)}{\lambda}. \tag{4.7}$$

The projection of the incident wave vector onto the grating plane is named $\mathbf{k}_{xy}$ with length $k\sin\theta$. This wave vector analysis is well suited for shallow gratings, when the waveguide mode is almost not perturbed by the grating, as is the case with the elements under study. With the knowledge of the waveguide mode from the previous Sect. 4.1 and by applying the grating diffraction, it is easy to estimate a good starting point for the rigorous calculations.

4.3. Angular efficiency

The following section only applies to oblique incidence. At normal incidence the situation is different, as the slope of the dispersion map tends towards zero. This is due to the coexistence of two coupling modes, which both fulfill the Bragg condition for reflection within the waveguide. With double periodic structures, the angular tolerance can be even further increased [LEM98,MIZ03].

Assuming monochromatic illumination the angular reflection response is directly related to the spectral reflection response through the slope of the λ-θ map at oblique incidence (see Fig. 3.16). In the absence of absorption and scattering, a plane wave reaches 100% reflectivity for a given wavelength at the resonance angle [MAS85]. A mismatch of the resonance angle translates to a reduced peak reflectivity. A finite incident beam can be decomposed into plane waves (angular spectrum) and then each plane wave component has its specific reflection coefficient. The overall situation can be described by a multiplication of the angular spectrum of the incident beam by the angular response of the filter. In spatial coordinates this is equivalent to a convolution of the incident beam with the Fourier transform of the angular response of the filter. We see that the condition for high reflection efficiency is to ensure that the incoming angular spectrum is smaller than the accepted angular spectrum of the resonant grating filter.

The incident beam distribution coming from a single mode fiber collimator is assumed to be Gaussian and the angular response of the device is assumed to be Lorentzian. The angular response of the device is only selective in one direction, the direction of the grating vector. Therefore we can limit the discussion to this one dimension.

The angular spectrum G of the incident Gaussian beam $g(x) = A_0 \exp\left[-(x/w)^2\right]$, with waist w is

$$G(p_x) = FT\{g(x)\} = \sqrt{\pi} w A_0 \exp\left[-(\pi \ p_x w)^2\right]. \tag{4.8}$$

We use the paraxial approximation, $p_x = \frac{x}{\lambda z} = \frac{\theta}{\lambda}$, to obtain the angle (in radians). When taking an angular offset of θ_0, the projections have to be taken into account. Then the angle in the paraxial approximation with angular offset has to be divided by $\cos(\theta_0)$ for use in the same formalism. We find

$$\begin{aligned} G(\theta,\theta_0) &= \frac{\sqrt{\pi} w A_0}{\cos(\theta_0)} \exp\left[-\left(\pi \frac{(\theta - \theta_0) w}{\lambda \cos(\theta_0)}\right)^2\right], \\ G_{norm}(\theta,\theta_0) &= \sqrt{\sqrt{2\pi} \frac{w}{\lambda \cos(\theta_0)}} \exp\left[-\left(\pi \frac{(\theta - \theta_0) w}{\lambda \cos(\theta_0)}\right)^2\right], \end{aligned} \tag{4.9}$$

where G_{norm} is the angular spectrum of the Gaussian beam, normalized with respect to the energy. We can directly see the well-known angular half width $\Delta\theta$ at the 1/e points at $\theta=\lambda/\pi/w$, for $\theta_0=0$. Note that θ is the half angle.

The angular response of the RGF is of Lorentzian type [NOR96, ROS97] at oblique incidence in the absence of degenerate states, (i.e. no crossing lines in the λ-θ map). The optimized filter has an angular reflection response L with negligible out of resonance reflectivity:

$$\left|L(\theta,\theta_0)\right| = \frac{\left(\frac{\Delta\theta}{2}\right)^2}{(\theta-\theta_0)^2 + \left(\frac{\Delta\theta}{2}\right)^2}. \tag{4.10}$$

Since the device is tilted and the angle is defined with regard to the incident beam, there is an angular offset, $\theta \Rightarrow (\theta+\theta_0)$. The FWHM, $\Delta\theta$, is directly related to the slope of the λ-θ map with the spectral linewidth $\Delta\lambda$: $\Delta\theta=\Delta\lambda$ /slope. Then the peak efficiency is given by [POP01]:

$$\eta_B = \frac{\int |G(\theta)L(\theta)|^2 \, d\theta}{\int |G(\theta)|^2 \, d\theta} = \int (G_{norm}(\theta))^2 \left|L(\theta)\right|^2 d\theta. \tag{4.11}$$

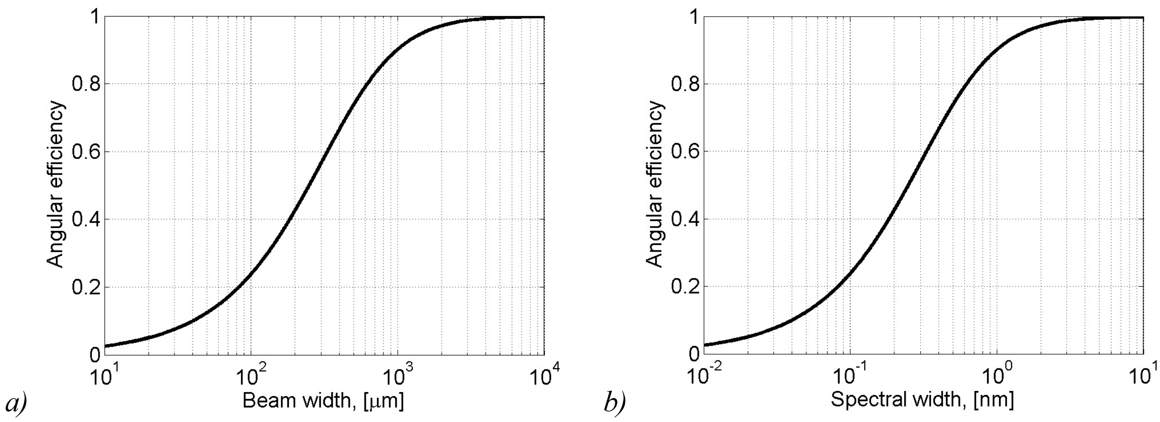

Fig. 4.4: Angular efficiency at $\lambda=1.545\mu m$, assuming a slope of 6.4nm/° in the dispersion map. (a) Fixed linewidth $\Delta\lambda=0.5nm$ with variable incidence beam waist and (b) fixed beam waist $w_0=0.5mm$ with variable linewidth of the filter.

The condition for Eq. (4.11) to be valid is that the incident angular spectrum $G(\theta)$ is real and positive.

Our filter is designed to have a spectral FWHM of 0.5nm, and a slope of 6.4nm/°. The output of a standard collimator has a waist of 0.5mm. The expected peak efficiency is shown in Fig. 4.4: a) a variable incident beam diameter and a fixed linewidth of the filter and b) a fixed incident beam diameter with a variable linewidth. We can see that with our design values and a standard collimator we get only a peak efficiency of 74%. Note that for highly selective devices one must choose either a wide collimated beam or a reduced angular selectivity. The angular selectivity and the spectral selectivity are related by the slope of the λ-θ map. A change in the angular selectivity by maintaining the spectral selectivity, corresponds to a change in the slope of the λ-θ map.

4.4. Waveguide grating model

The aim of this model is to describe the coupling process, with the waveguide as the central element. The calculations are made along the waveguide, in the transverse direction, in contrast to the FMM routines. As shown in Chapter 3, weak coupling devices are well described by the Fourier Rayleigh approximation. Thus we begin with the model of a directly structured waveguide [BRA95, LYN97]. We adapt the formalism and apply it to the RGF1201. The coupling coefficient is then determined for comparison with rigorous methods.

First we must determine the interaction strength of the grating, described by the radiation loss coefficient α, or its inverse, the coupling length L_c. With this knowledge we solve the differential equation governing the energy exchange. There are approximate analytical expressions for the radiation loss coefficient for directly structured waveguides [RIG76, AVR91]. In our device the grating is separated from the waveguide by the separation layer and, therefore, this theory cannot be applied directly. In order to overcome this problem we may consider the coupling as consisting of two processes, a lateral grating coupling in conjunction with a vertical evanescent coupling. The evanescent coupling through the separation layer can be described as a prism coupler. Qualitatively it can be said that if the incident beam is much larger than the coupling length, there is almost no shift between the input and the output beam. Then we need essentially a device size of the order of the incident beam. The other extreme is that the beam size is much smaller than the coupling length. Then the region of coupling is relatively inefficient. The mode in the waveguide, after the incident beam, is governed by the exponential decay of the mode amplitude.

4.4.1. Prism coupler

A simple way to couple into a planar waveguide is using evanescent wave coupling [TAM79]. This can for example be achieved by illuminating a sandwich consisting of two high index materials separated by a low index material under an angle (in the high index material) that is large enough to cause total internal reflection at the first interface. The evanescent wave in the low index material becomes a propagating wave in the second high index material. However the field amplitude is decreased exponentially when traversing the low index medium, governed by the decay constant. The decay constant α_e is simply the inverse of the penetration depth, known from planar waveguide theory:

$$\alpha_e = k_0\sqrt{n_{wg}^2 \sin\left(\theta_m\right)^2 - n_c^2}\ . \tag{4.12}$$

With the parameters used in previous section and with λ=1545nm, the angle θ_m is 56°. This leads to an exponential decay constant of 5.05 $10^6 m^{-1}$ or a penetration depth of 198nm.

4.4.2. Grating coupler

The period of our filter is short enough so that only the –1st diffraction order is non-evanescent in the waveguide. Thus we obtain significantly simpler formulae [PAR96]. If we take a perfect planar waveguide with propagating light and add a semi-infinite grating at z=0, then the light starts to couple out by radiation. The field in the waveguide decreases exponentially, with decay constant α_0, the radiation loss coefficient. For a sinusoidally modulated waveguide of height h_{wg}, with undulation amplitude $h_g/2$ within the Rayleigh approximation, the radiation loss coefficient for TE polarization can be expressed as [PAR96],

$$\alpha_0 = \left(\frac{k_0 h_g/2}{2}\right)^2 \frac{n_{wg}^2 - n_e^2}{n_e h_{wg}} \frac{\left(n_{wg}^2 - n_s^2\right)\left\{N_c N_{wg}^2 + N_s\left[N_c^2 + \left(n_{wg}^2 - n_c^2\right)\cos^2\left(N_{wg} k_0 h_{wg}\right)\right]\right\}}{\left[N_{wg}^2 + N_s N_c\right]^2 - \left(n_{wg}^2 - n_c^2\right)\left(n_{wg}^2 - n_s^2\right)\left(\cos^2\left(N_{wg} k_0 h_{wg}\right)\right)} \tag{4.13}$$

$$N_i = \sqrt{n_i^2 - \left(n_e - \lambda_0/\Lambda\right)^2},\ i = s, c, wg\,. \tag{4.14}$$

The indices s, c and wg correspond to the substrate, cover and waveguide. With the same values as for the prism coupler and with a grating period of 592nm, we obtain 4620 m^{-1} for the radiation loss coefficient for the device without the separation layer. This result corresponds to a coupling length of 217µm. Rectangular phase gratings couple more efficiently in the ±1st order than a sinusoidal grating with the same height (Sect. 3.3.3). The coupling strength of the grating is directly related to the spectral width of the resonance [AVR89]. Since Eq. (4.13) was derived for a sinusoidal grating we introduce a correction factor f_c to adjust the radiation loss coefficient for rectangular gratings. FMM calculations of the RGF1201 with a rectangular grating and a fill factor of 0.5 show a linewidth of 0.518nm, whereas with a sinusoidal grating (sliced into 100 layers), with the same height shows a linewidth of only 0.322nm. Thus f_c=0.518nm/0.322nm=1.6009, which comes close to the predicted difference of $(4/\pi)^2$=1.621.

4.4.3. Combination of prism and grating coupler

For the above analysis, we know the interaction strength α_0 for a grating adjacent to the waveguide. However, with our device the diffracted light has to tunnel twice through the separation layer h_{sep}. We shall neglect the possible interference caused by the separation layer. Thus the equivalent radiation loss coefficient can be written as

$$\alpha = \alpha_0 \quad f_c \exp\left(-2\alpha_e h_{sep}\right) \tag{4.15}$$

with α_0=4620m^{-1}, f_c=1.6009, α_e=5.05 10^{-6}m^{-1} and h_{sep}=146nm we obtain α=1701m^{-1}=1.701mm^{-1}, corresponding to a coupling length of 588μm.

4.4.4. Field amplitude on the grating

We adapt the formalism for the determination of the coupling efficiency [LYN97], with the difference that we do not try to maximize the light contained in the waveguide at the end of the grating of length L_g, z=0, (Fig. 4.5). The device is illuminated by a Gaussian beam with a waist w_0 at an angle θ with its center Δz away from $-L_g$. The waist w_0 of the Gaussian beam is located at a distance l_0 from the grating. Then the normalized incident amplitude is given by [LYN97]

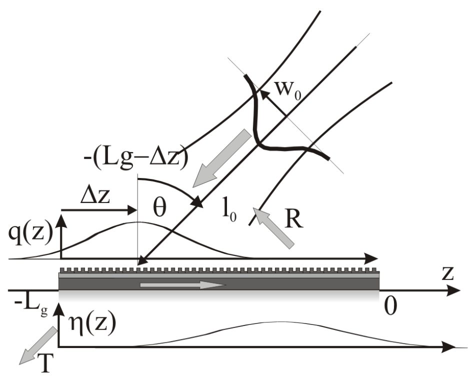

Fig. 4.5: Grating coupler. The incident Gaussian beam with waist w_0, l_0 distant from the point $-(L_g-\Delta z)$ incident on the grating. The light with complex amplitude q(z) along the grating surface couples into the waveguide leading to an efficiency η(z).

$$q(z) = \sqrt{\frac{\sqrt{1/\pi}}{w_0}\frac{1+i\delta}{1+\delta^2}\exp\left[-\frac{i\delta}{1+\delta^2}\left(\frac{z+\Delta z}{w_0/\cos(\theta)}\right)^2\right]\times\exp\left[-\frac{1}{1+\delta^2}\left(\frac{z+\Delta z}{w_0/\cos(\theta)}\right)^2\right]} \tag{4.16}$$

with

$$\delta = \frac{2\left[l_0 + (z + \Delta z)\sin(\theta)\right]}{k w_0^2}. \tag{4.17}$$

At normal incidence and with the waist on the grating, δ=0 and the complex amplitude reduces to a conventional real Gaussian amplitude.

4.4.5. Power efficiency η_{wg}

The power efficiency of the mode excitation η_{wg} is defined as the ratio of the power in the waveguide at a distance z and the incident power between –infinity and z. The power in the mode of an infinite device is zero at –∞ and light starts to couple in while approaching the incident beam. After reaching its maximum, more light is coupled out than in. Far enough from the incident beam the light is coupled out completely. Neglecting the scattering, absorption and reflection at the edges of the grating, the efficiency is given by [LYN97][4]

$$\eta(z) = 2\alpha\cos(\theta_0)\exp(-\alpha z)\left|\int_{-L_g}^{z}\exp[(\alpha + i\,\Delta\beta)z']q(z')dz'\right|^2 \tag{4.18}$$

with

$$\Delta\beta = k\left(\sin\theta_0 - \sin\theta\right). \tag{4.19}$$

Δβ is the detuning from the excitation resonance. Maximum coupling occurs under the phase-matching condition (Δβ=0), corresponding to the maximum power transport in the waveguide. An example of the power efficiency in the waveguide along the z axis is given in Fig. 4.6. For weak coupling gratings, the shift between the maximum of the incident beam and the maximum power in the waveguide becomes important. In the tail (right side), where the incident beam vanishes, there is still energy in the waveguide and the power efficiency decay is exponential.

---

[4] In [LYN97], the efficiency is always evaluated at z=0, thus the term exp(-αz) is equal to 1.

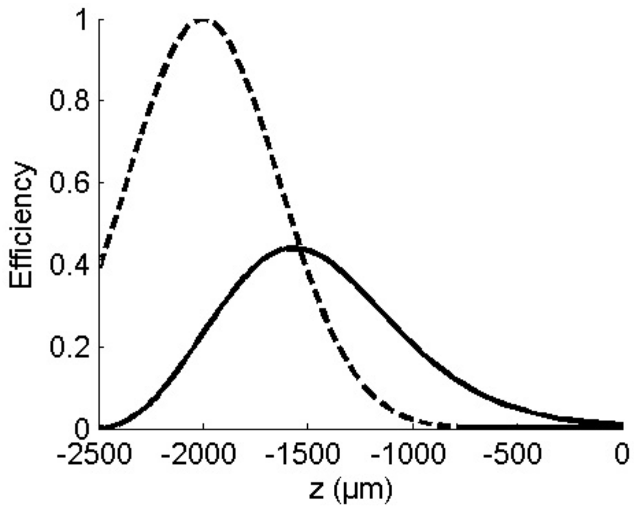

Fig. 4.6: Power efficiency $\eta(z)$ (solid line) as a function of z on a finite device for a given incident beam. The dashed line corresponds to the normalized intensity of the incident beam $|q(z)|^2$. The simulation parameters are w_0=500µm, Δz=500µm, λ=1545nm, α=1.70mm^{-1}, and θ_0=45°. Through the truncation of the incident beam 8% of the energy is lost. At z=0µm, after 2.5mm, there is still 4.4% of the light in the waveguide.

4.5. Rigorous determination of the radiation loss coefficient

The radiation loss coefficient can best be determined when only the outcoupling process occurs. Then the exponential field decay can directly be observed. However the outcoupling process can not easily be separated from the coupling in process. According to [BRA95] we can construct a situation, where the size of the incoming beam is smaller than the coupling length and the grating length. The coupling length obtained by the approximate model for RGF1201 is more than half a millimeter. This makes the rigorous calculation of a finite device prohibitively inefficient. So we must consider an infinite grating. Because of the linearity of Maxwell's Equations we can construct a limited incident beam by plane wave superposition. Then every plane wave is propagated through the structure and the fields obtained for each plane wave are added coherently. The resulting field for RGF1201 is shown on a logarithmic scale (Fig. 4.7), with the incident beam omitted. More details about the field calculations are given in Sect. 6.2. The incident beam coming from the upper left is strongly coupled and mostly reflected. As we know from rigorous grating theory, we can separate the variables. So a horizontal (z=const) section of the field is sufficient to determine the transverse distribution. This is important from a numerical point of view. Only because of this property are we able to calculate the section with a reasonable sampling rate. The extended section taken in the middle of the waveguide of the RGF in the same situation is given in Fig. 4.8. On the logarithmic scale we can clearly see the exponential tail on the left and the Gaussian shape on the right side, including a small field-shift to the left. An exponential fit gives a radiation loss coefficient of 2.03mm^{-1} or a coupling length of 492µm. The value obtained with all the approximations is 16% smaller.

The advantage of the rigorous method is that it is possible to get an accurate value for all grating shapes, including thin films, superimposed gratings etc.

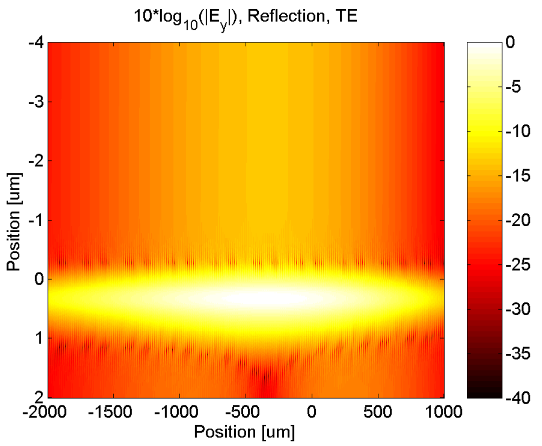

Fig. 4.7: Field distribution of the RGF1201 under resonance. Note that the x- and the z-axis do not have the same scale. The field is incident at 45° from the upper left corner. We find a strong field enhancement (more than a factor 100) and therefore use a logarithmic field scale. The incident field hits the structure at x=0 and a beam shift of the reflected beam towards –x can be observed. The incident field is omitted.

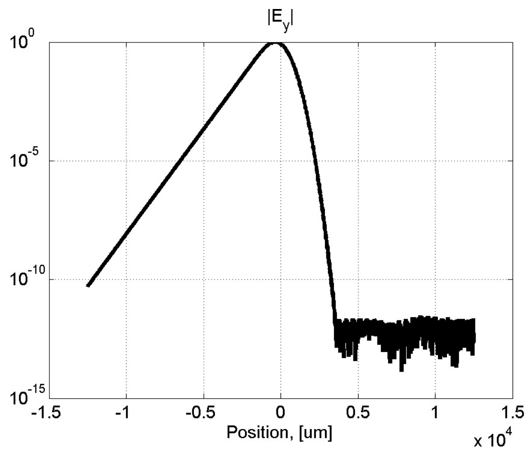

Fig. 4.8: Extended section of the field distribution at the center of the waveguide (z=328nm) of Fig. 4.7. On a logarithmic scale we can clearly see the exponential tail on the left side and the Gaussian shape on the right side, including a small shift to the left with respect to the incident beam centered at z=0. The exponential fit gives a decay constant of $\alpha=2.03mm^{-1}$.

5. Polarization Independence

In general, resonant grating filters are polarization dependent. We can distinguish in a simple manner two main sources of polarization dependence: the modes of a planar waveguide are different for the two fundamental polarizations and the grating shows form birefringence. A system for telecommunications should ideally show the same spectral response for all incoming polarization states. Therefore we study RGF configurations for the resonances for which the two orthogonal polarization states coincide. We define polarization independence to be when the resonances take place under the same angle of incidence and wavelength. Full polarization independence is achieved when in addition the peak widths coincide. We discuss possible solutions with 1D gratings and with crossed gratings, as is shown in Fig. 5.1.

A common condition for efficient polarization-independent filtering can be outlined. The simultaneous excitation of *two* independent modes is necessary to obtain high-efficiency filtering of unpolarized light [FEH03]. In classical incidence all coupling processes can be reduced to two dimensions. The two excited modes can in general exchange energy (cross-

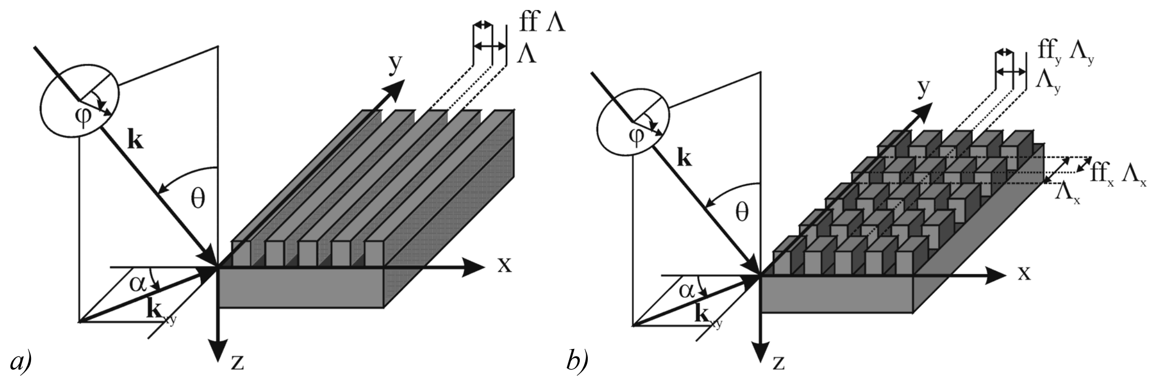

Fig. 5.1: Definitions for conical incidence for a) a 1D grating and b) a crossed grating. θ: incidence angle, φ: polarization angle, α: conical angle, ff: fillfactor. φ=90° and. φ=0° correspond to incident s-and p-polarized light, respectively.

coupling), but not in the classical mount[5]. The cross-coupling results in change of the dispersion relation, including the possible appearance of no possible resonance for certain wavelengths (analogy to an energy gap). By minimizing this cross-coupling, the gap of no resonances can be reduced and even brought to zero. One solution is to choose a situation with symmetric or antisymmetric eigenmodes or to choose orthogonal propagation directions [FEH02]. It has been shown that we need left-right symmetry for efficient coupling for all states of polarization. In absence of this symmetry, light that couples out of the structure may couple into modes other than the specularely reflected order, resulting in a reduced efficiency. For the coupling in, the mode in the waveguide has to be matched. A homogenous region offers a continuum of modes. Thus the light coupling out always matches a "mode".

5.1. 1D grating

An exhaustive theoretical discussion about polarization independent RGFs with a simple grating can be found in [LAC02]. Here we treat only conceptual aspects, without a detailed theoretical discussion. Again, the RGF of interest differs in the fact, that we add a separation layer.

5.1.1. a) Classical incidence

The advantage of classical incidence is that the polarization states are well separated and no polarization mixing occurs. An incident s-polarized (s-light) wave couples into a TE Mode and an incident p-polarized (p-light) wave couples into a TM mode. Light coupling from a TE mode into the TM mode or vice versa via the grating is not possible. For a given wavelength and angle of incidence it is not possible to obtain a resonance for the same mode number and same diffraction order for both polarizations. Therefore we have to look at crossing lines in the dispersion map, leading to some discrete solutions. One possible solution for a single mode waveguide is to couple p-light by the -1^{st} diffraction order and s-light by the $+1^{st}$ diffraction order into the corresponding modes. The unique angle is determined by the structure. Another solution is to take a multimode waveguide and to couple into adjacent

[5] See definition in Sect. 2.2.1.

modes for the two polarizations. In all these cases the angle of incidence is imposed by the structure, and we only have discrete solutions, consequently, angular tuning is not possible.

5.1.2. b) Conical incidence

Conical incidence means that the conical angle α is non-zero. When the conical angle α reaches 90° we denote it as full conical incidence. It can be seen that there are not many degrees of freedom to place the resonance location independent of the incoming polarization state. The dispersion diagram of the unperturbed waveguide shows that the TE- and TM-modes are far from each other and thus it is not possible to excite two modes with different polarization with the same mode number and the same grating diffraction order simultaneously with a 1D-grating. In full conical mount two mirror (anti-)symmetric modes of the same polarization are excited. As long as the incident wave and the mode propagation direction are not orthogonal, coupling is possible. With in general the resonance conditions for incident p- and s-polarization differ slightly. The phase shift of the coupling process depends on the polarization as well as the effective index of the grating (form birefringence). The form birefringence can be changed by changing the fill factor of the grating. In some cases the phase difference between incident s- and p-polarization cancel out and resonance occurs for all incident polarization for the same angle of incidence and wavelength. For illustration an example based on the RGF0303 (Fig. 5.2) is shown in Fig. 5.3. The incoming light is linear polarized at φ = 45°. With a grating period of 972nm, we couple into two TE modes, and with the same device, but a grating period of 1075nm, two TM modes (Fig. 5.4) are excited. In both cases the resonance lines cross and we find points of

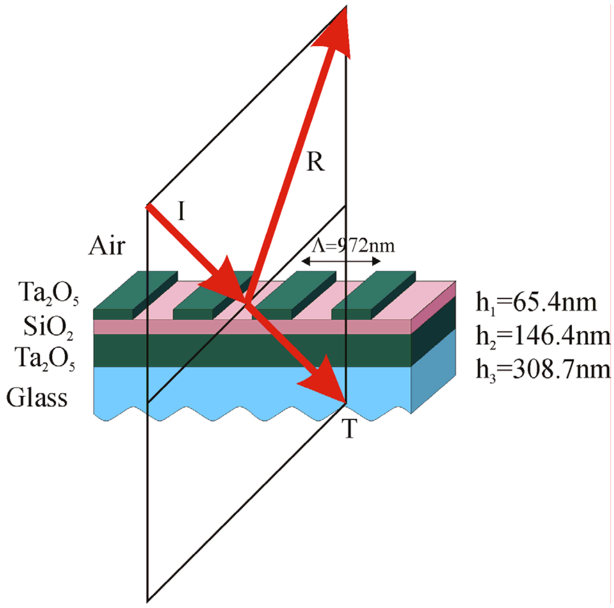

Fig. 5.2: Polarization independent filter, RGF0303, working around 45° AOI in full conical incidence. The grating fill factor is 0.475. The refractive indices are n_{Ta2O5}=2.066, n_{SiO2}=1.444, n_{Glass}=1.51, and n_{Air}=1.0, α=90°.

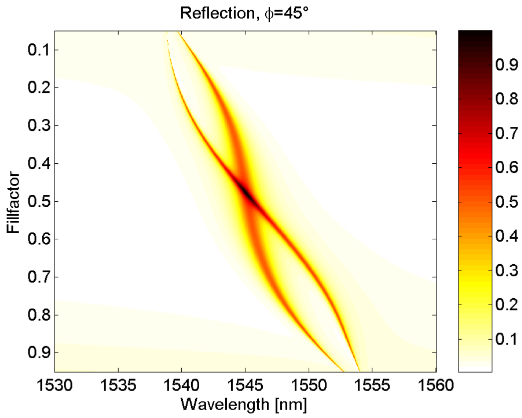

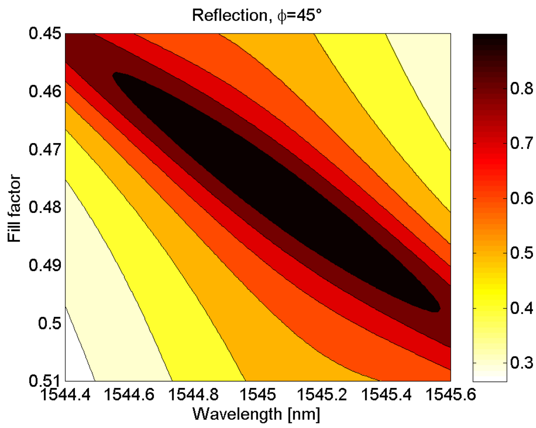

a) *b)*

Fig. 5.3: a) Spectral reflectivity for 45° linearly polarized light of the RGF0303 as a function of the fillfactor with b) magnified view of the intersection point. The light is coupled into two TE-modes with a grating period of 972nm. The narrower ridge corresponds to the incident s-polarization.

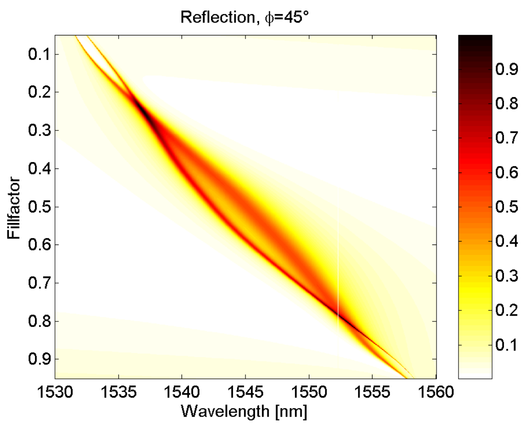

a)

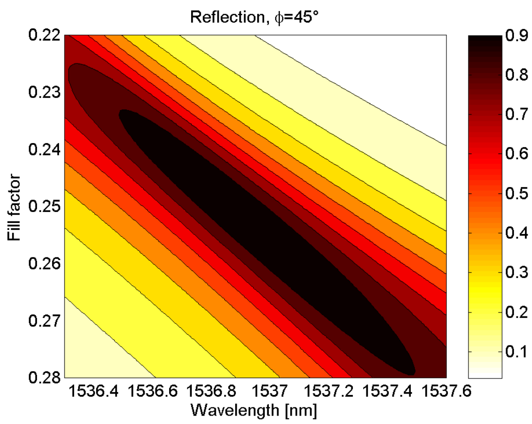

b)

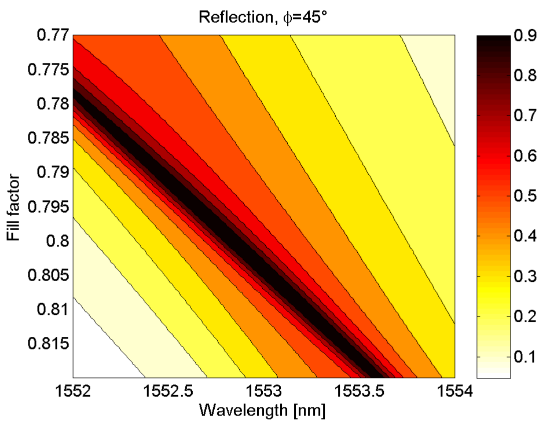

c)

Fig. 5.4: Spectral reflectivity of the RGF0303, but with a period of 1075nm, as a function of the fillfactor. The light is coupled into two TM-modes. The two ridges cross twice and magnified views of the two intersections are shown in b) and c) respectively. The narrower ridge corresponds to the incoming p-polarization.

polarization independence. Since the intersection point is closer to a fillfactor of 0.5 and since there is more margin to prevent propagation of non-specular orders we prefer to couple into two TE modes.

Unfortunately, the resonance width under 45° AOI depends on the polarization. It can be shown that there exists one AOI where the two resonance widths are equal [LAC02]. In our application it is important to work around 45° and thus we optimize the structure around that angle and we accept a polarization dependent width. At 45° AOI, it is no longer possible to reduce the out of resonance reflection to 0 for both orthogonal polarizations simultaneously. Thus the sum of the reflectance for incident s- and p-polarization was minimized. The resulting element of this optimization, with a very similar procedure to the one described in Sect. 3.4. is given in Fig. 5.2 and named RGF0303. This RGF shows a spectral width of 0.56nm for incident s- and 1.64nm for incident p-polarization, a ratio of 2.92. The dispersion map is given in Fig. 5.5 and some cross-sections for different incident polarizations are given in Fig. 5.6. We can clearly see that the relative peak positions, as well as the peak shapes are maintained when changing the angle of incidence. Therefore we can conclude that it is

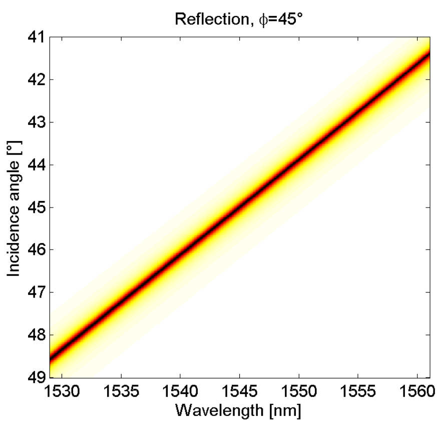

Fig. 5.5: Dispersion diagram of the RGF0303. The incident light is polarized at φ=45°. We can observe a linear relation between the incident angle and the resonance wavelength. The sign of the slope is negative, as in the case of forward coupling in the classical configuration.

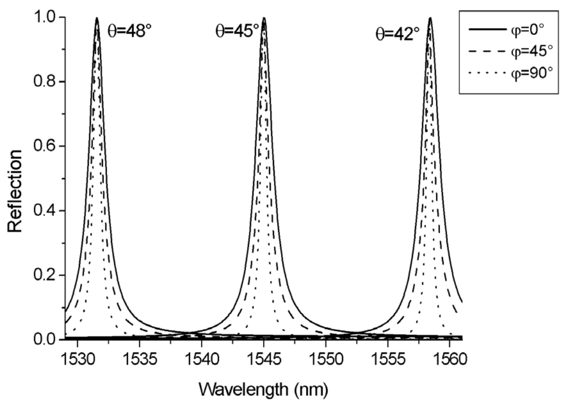

Fig. 5.6: Tunability of the RGF0303. For three different angles of incidence (θ) and three different polarization angles (φ) the spectral reflectance is shown. It can be observed that the polarization independence as well as the peak shape is maintained.

possible to use this structure as a tunable device. The impact of the different design parameters on the resonance location and its width are similar to the example discussed in classical incidence, with one exception: the conical angle. As already stated above, for efficient coupling, two modes have to be excited. A small deviation in the conical angle corresponds to breaking the symmetry and thus two different modes can be excited, resulting in a split of the peak as shown in Fig. 5.7. The slight asymmetry of the figure with respect to the conical angle is due to the non- symmetric incident polarization state resulting in a small change in the coupling efficiency.

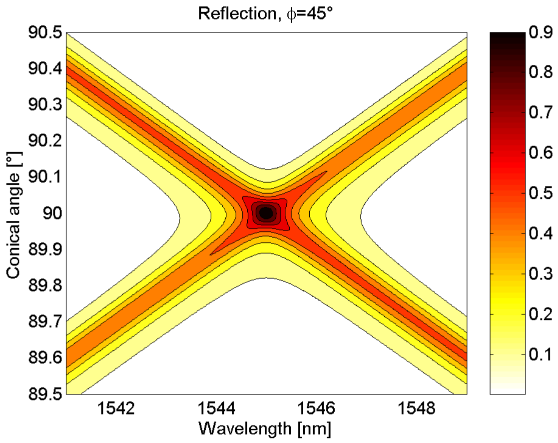

Fig. 5.7: Conical angle dependence of the RGF0303. We can see that an accuracy better than 0.1° in conical angle is necessary to prevent a double peak in reflection.

5.2. Crossed gratings

Crossed gratings offer additional degrees of freedom, but also more design challenges. In the case of crossed gratings, it is possible to excite a TE- and a TM- mode at the same time. For efficient coupling we need to excite two modes with mirror symmetry. The easiest way to get polarization independence is at normal incidence on a checkerboard-like grating [PEN96]. Since the projection of the incident wave-vector in the grating plane is zero, two perpendicular propagating modes are excited. Normal incidence has the drawback, that for extracting the reflected light additional elements are required, and thus we study oblique incidence. At oblique incidence we have a non-zero component in the grating plane from the input wave-vector.

In order to match the resonance for all incoming polarization states for the same parameters, the grating form birefringence must compensate the phase difference resulting from the coupling for the different polarization states. This is not always possible, as for example for very shallow gratings. In two dimensions this problem is not easy to solve and numerical calculations are often very tedious. For efficient coupling and easier design, the plane of incidence must be a symmetry plane of the structure. Some designs can be found in [MIZ01] and illustrations of some configurations are given in [NIE03].

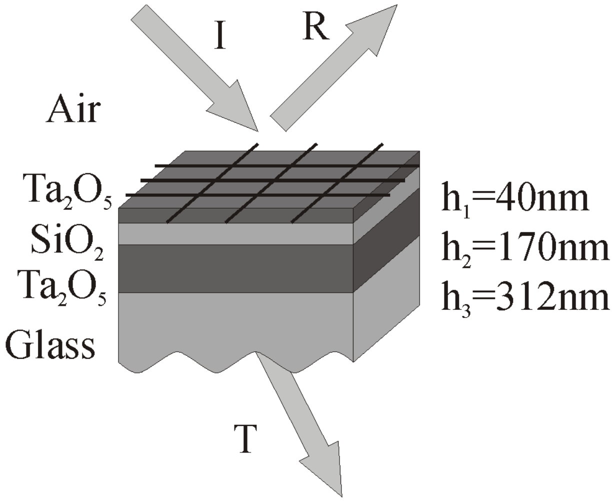

Fig. 5.8: Common starting point (three layer stack) for the different configurations. By only adjusting the grating layer polarization independence can be

The calculations are based on [LI97] and the model has been implemented by V. Kettunen. The few examples given consist basically of the same three layer stack (see Fig. 5.8), showing an approximate out-of-resonance reflection minimum with a grating having a fillfactor of 0.5 under 45° AOI and λ=1545nm.

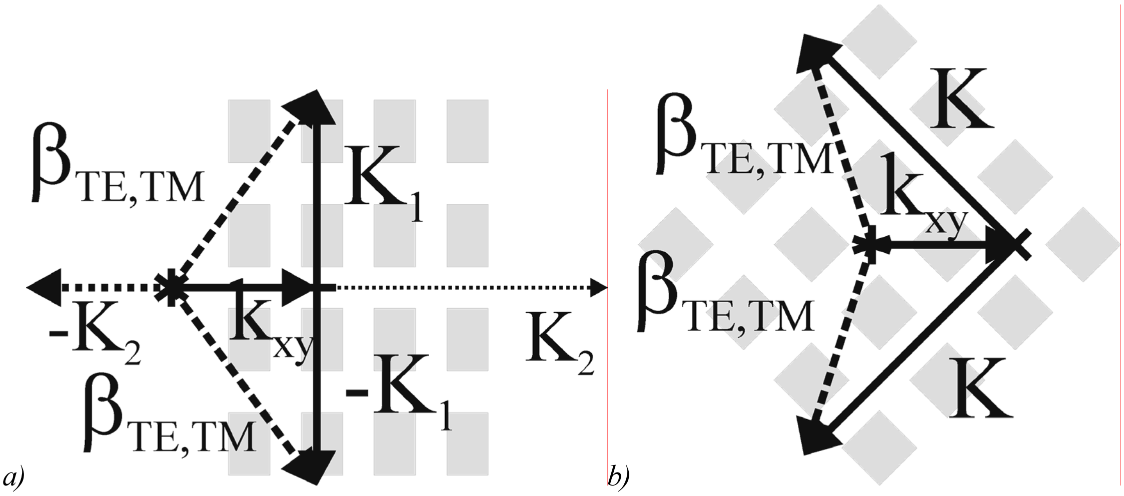

Fig. 5.9: Wavevector diagrams, a) incidence along one grating vector and b) corner illumination. In the first case only the transverse grating couples and the other grating only adds birefringence. In the second case, the two gratings have to be similar to achive mirror symmetry.

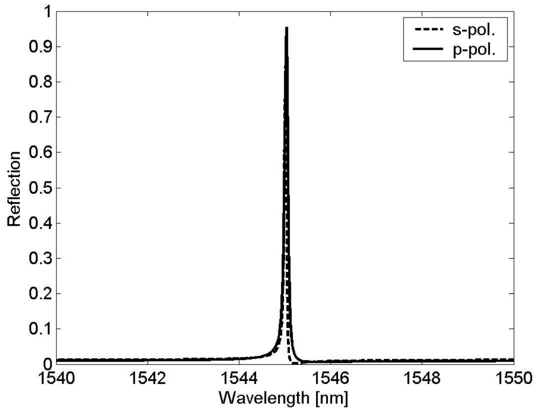

Fig. 5.10: Reflection spectrum of configuration shown in Fig. 5.9a) with a grating thickness of 40nm. With Λ_x=550nm, Λ_y =972.5nm, ff_x=0.5, ff_y=0.465.

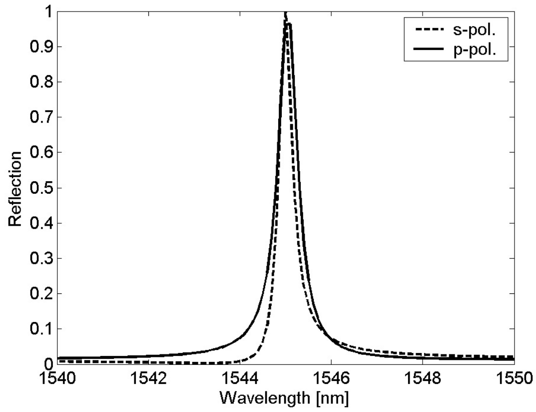

Fig. 5.11: Reflection spectrum of configuration shown in Fig. 5.9a) with a grating thickness of 200nm. With Λ_x=550nm, Λ_y =971.5nm, ff_x=0.5, ff_y=0.42.

5.2.1. a) Illumination along the grating grooves

This case is very similar to the 1D grating in full conical mount and its wavevector diagram is shown in Fig. 5.9a). Only the grating perpendicular to the plane of incidence acts as a coupling grating. The other grating is only a birefringent element. The period of the second grating should be chosen to avoid an additional resonance with resulting distortion of the dispersion map. An example is given in Fig. 5.10. It can be seen that the coupling power of the grating is very weak. This is clear since the grating used for coupling is only piecewise constant, due to the intersection with the second grating. For better coupling the grating height was increased from 40nm to 200nm and the result is shown in Fig. 5.11, with a similar resonance width as the 40nm grating of the 1D grating in full conical incidence.

5.2.2. b) Corner illumination

In the case of corner illumination, we assume we have two equal crossed gratings with the corresponding wavevector diagram shown in Fig. 5.9b). Then we have a symmetry plane along the bisector. With the shallow grating (40nm) we were unable to find a solution for polarization independence. So the grating depth was increased to 200nm and the result is shown in Fig. 5.12. Due to the significant grating thickness and the large fillfactor of 0.74, the out of resonance reflectivity for the incoming s-polarization becomes critical.

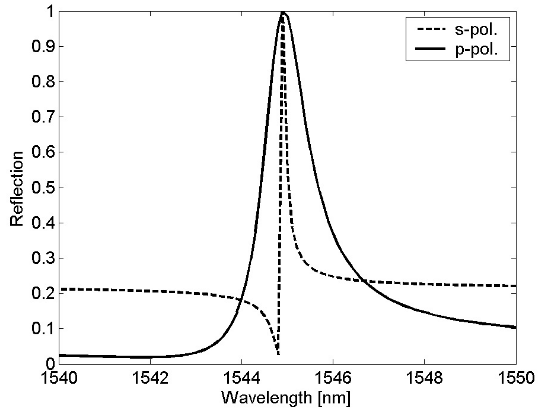

Fig. 5.12: Reflection spectrum. Configuration of Fig. 5.9b) with a grating thickness of 200nm. With $\Lambda_x = \Lambda_y = 710.0nm$, $ff_x = ff_y = 0.74$.

5.2.3. Coupling between waveguide modes

An important issue in the design and understanding of structures with crossed gratings is to look at the crossing lines in the dispersion diagram with respect to the grating periods. We consider a specific case, where the interpretation is easy. We want to have a symmetric checkerboard grating, with corner illumination under an angle of incidence of 45°. First we use the wave vector analysis of Fig. 5.9b) to predict the resonance locations:

$$\begin{aligned} &\boldsymbol{\beta} = \mathbf{k}_{\mathbf{xy}} + \mathrm{M}\,\mathbf{K}, \quad \mathrm{M} = 1 \\ &\boldsymbol{\beta} = \mathrm{n}_{\mathrm{eff}}\frac{2\pi}{\lambda}\begin{pmatrix}\cos\delta\\ \sin\delta\end{pmatrix}, \quad \mathbf{k}_{\mathbf{xy}} = \frac{2\pi}{\lambda}\begin{pmatrix}\sin\theta\\ 0\end{pmatrix}, \quad \mathbf{K} = \frac{2\pi}{\Lambda}\begin{pmatrix}\cos\gamma\\ \sin\gamma\end{pmatrix} \end{aligned} \tag{5.1}$$

We would like to couple into two TE modes. The effective index of the undisturbed TE-mode in the sandwich between two infinite glass and SiO_2 layers is 1.7467. With λ=1545nm, θ=45°, γ=135° (backwards coupling), we find a solution for δ=118.37° and Λ=710.8nm. The resonant grating period obtained with rigorous calculations is near 710.0nm for d_g=200nm, as

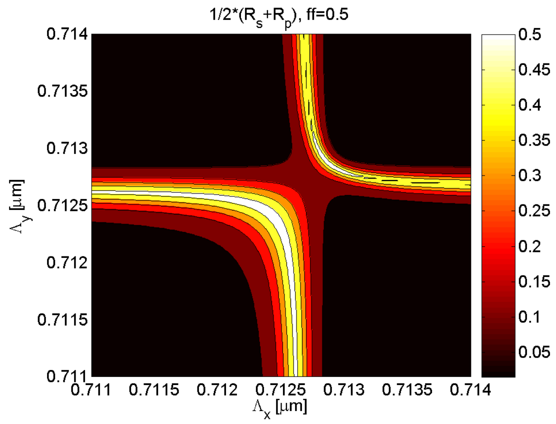

Fig. 5.13: Average reflection of incident s- and p-polarizations with a fill factor of 0.5 as a function the grating periods for the configuration of Fig. 5.9b) with a grating thickness of 200nm. In this case we have mode competition and one mode dominates the other.

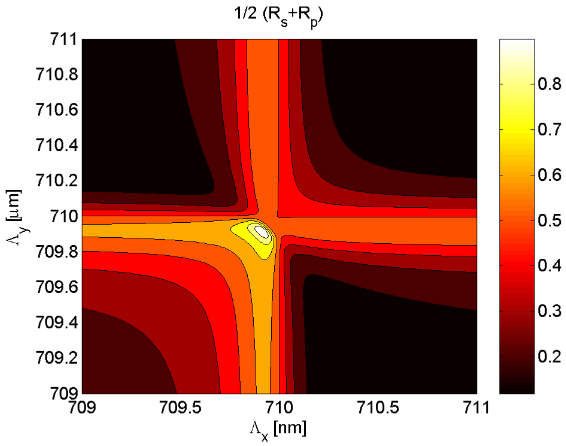

Fig. 5.14: Average reflection of incident s- and p-polarizations with a fill factor of 0.75 as a function the grating periods for the configuration of Fig. 5.9b) with a grating thickness of 200nm. In this case there is a point of polarization independence. The resonance widths of incident s- and p-polarizations differ significantly.

shown in Fig. 5.12. First we consider the case with a non-optimized fill factor. For an uncoupled system, one would expect a smooth crossing of the two branches. However since the coupling phases of the branches are in general different, but they are to couple into the same mode, the system is perturbed. The two branches repel each other. Following the line of symmetry (Λ_x=Λ_y) two peaks with different widths can be observed. The average reflectance clearly does never exceeds 50% and efficient polarization independent coupling is not possible, as shown in Fig. 5.13. By adjusting the fill factors, the phase difference can be eliminated in some cases. In Fig. 5.14 (fill factor 0.75) the two branches cross. Since the coupling efficiencies of the incident s- and p-polarizations are very different, the crossing is not completely symmetric, but there is a point where the reflectance is clearly higher than 90% for all polarization states.

5.3. Summary

The nature of the coupling processes involved in RGFs is polarization dependent. There exist configurations where the resonance locations coincide for all incoming polarization states. If only one mode is excited, the coupling efficiency for the incoming linearly polarized light varies according to its projection from 0 to 100%. So for efficient coupling, two modes must be excited, lying in a plane of symmetry. Then, in general, mode coupling can be observed. In some cases, the form birefringence of the grating can be used to equalize the phase difference of the coupling process to achieve efficient coupling. The resonance widths depend in general on the incoming polarization states. It can be shown that only for one incidence angle are the two widths equal. Tuning over a limited range is possible for the above-mentioned examples. In the full conical case, the tolerances are similar to the classical case, with the exception that the conical angle must be matched as precisely as the incidence angle. The tolerances in the crossed grating cases are even tighter. It is necessary to match exactly the conical angle and stay on a plane of symmetry. Deviations lead to a rapid decay of the efficiency and to a splitting of the resonance peak. It can be said that there are possibilities to realize polarization independent RGFs, at the cost of degrees of freedom.

6. Towards the Microsystem

There are many things to consider regarding the microsystem. Firstly the effects of limited device size, as well as limited incident beam are considered. Since the incoming and outgoing light is confined in fibers, the coupling efficiencies are evaluated. At the end we look at degrees of freedom available to influence the spectral resonance shape or to obtain a switching device.

If we reduce the size of an optical system, we usually must also reduce the diameter of the illumination beam. Consequently, the influence of diffraction increases. Therefore, we consider in this chapter finite-extend elements and beams. We investigate their influence on the optical performance. For example a Gaussian beam can be described by a superposition of plane waves. The RGFs of interest (see Sect. 3.3) are weak coupling devices, i.e. they need typically more than 1mm length to couple. The number of retained orders scales with the width of the grating cell, but the computational time (memory) is proportional to the power of three (two) of the retained orders (Fig. 3.2), limiting severely the direct calculation of large elements. First the losses due to finite dimensions of the beam and the element are estimated by using an approximate model. Then three FMM-based techniques are presented. In the first model, a finite incident beam impinges on an infinite device. Secondly, with the use of some approximations the losses of a finite incident beam in combination with a finite device are estimated. In order to compare the approximations, a third model is presented where the FMM-period contains the whole device. A strong coupling device (i.e. having a small interaction length) is presented in order to able to simulate it.

6.1. Losses due to the finite element and beam size in the approximate model

The total efficiency (or maximum obtainable peak reflectivity) can be predicted as a function of the size of the system. For each beam diameter and element length we can determine a maximum efficiency η_B [Eq. (4.11)], (Fig. 6.1). The finite device size induces two kinds of losses: the light not coupled out at the end of the device $l_C=\eta(z=0)$ [Eq. (4.18)] and the light not impinging on the device l_B

$$l_B = 1 - \int_{-L_g}^{0} q(z) q^*(z)\ dz\,, \tag{6.1}$$

with q(z) being the normalized complex amplitude of the incident beam. Then we simply multiply the amount of light coupled in and out again by the angular efficiency η_B to obtain the total efficiency η_{tot}

$$\eta_{tot} = \eta_B \left(1 - l_c - l_B\right). \tag{6.2}$$

The spectral linewidth is proportional to the coupling coefficient. Consequently, the coupling coefficient is fixed by imposing the spectral linewidth of the resonance peak. We can maximize the total efficiency η_{tot} by optimizing the Gaussian beam width w and its position on the grating Δz for a given grating length L_g (Fig. 4.5). The maximum efficiency and their corresponding lengths are presented in Fig. 6.2. Some values are given in Table 6.1. The optimization was done twice: once with the coupling coefficient (radiation loss coefficient α) obtained with the approximate model [Eq. (4.15)] and once with the coupling coefficient from FMM-based

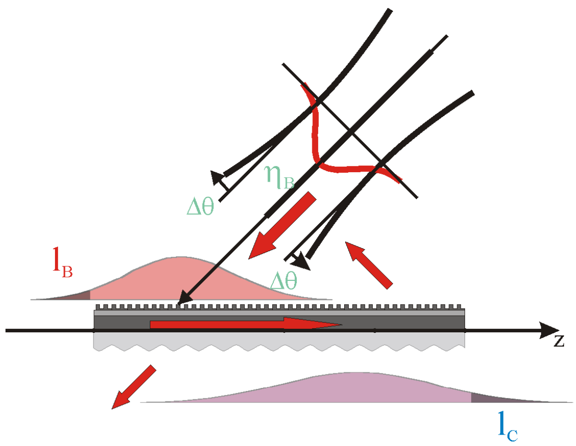

Fig. 6.1: Three factors can reduce the total efficiency. The angular efficiency η_B, the light not impinging on the device l_B and the light not coupled out before the end of the device l_C.

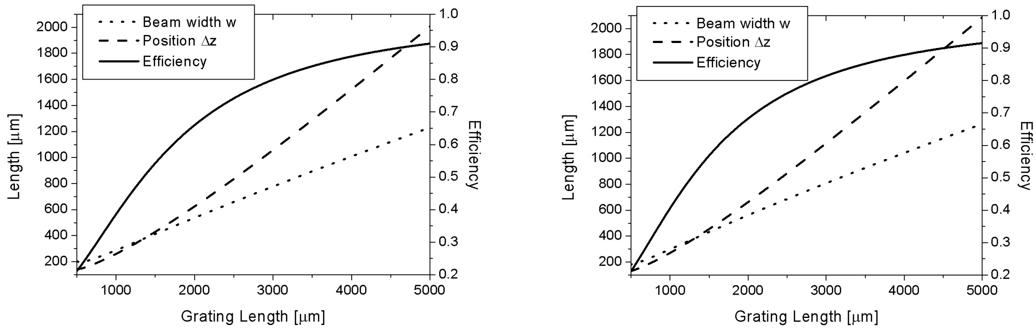

a) *b)*

Fig. 6.2: Maximum obtainable efficiency and their corresponding width w (dotted line) and position Δz (dashed line) as a function of the grating length. The corresponding coupling coefficient is a) α=1.70mm^{-1}, obtained by the approximate model, Eq. (4.15), and b) α=2.03mm^{-1}, obtained from the FMM-based calculations, Sect. 4.5.

α=1.70mm^{-1} (approximate value)

Efficiency	*Grating length*	*Gaussian waist*	*Δz*
20%	0.460	0.228	0.155
30%	0.760	0.232	0.193
40%	1.060	0.304	0.279
50%	1.360	0.378	0.380
60%	1.740	0.473	0.521
70%	2.240	0.596	0.724
80%	3.020	0.782	1.067
90%	4.700	1.164	1.860
95%	7.133	1.676	3.059
98%	12.000	2.662	5.500
99%	17.800	3.757	8.413
99.5%	26.300	5.281	12.677

a)

α=2.03mm^{-1} (rigorous value)

Efficiency	*Grating length*	*Gaussian waist*	*Δz*
20%	0.470	0.182	0.128
30%	0.730	0.229	0.187
40%	1.000	0.299	0.271
50%	1.280	0.374	0.371
60%	1.620	0.464	0.504
70%	2.100	0.587	0.707
80%	2.860	0.778	1.052
90%	4.520	1.159	1.851
95%	6.933	1.676	3.049
98%	11.800	2.657	5.491
99%	17.600	3.751	8.401
99.5%	26.100	5.275	12.661

b)

Table 6.1: Simulation results for a device with a coupling coefficient of a) α=1.70mm^{-1} and b) α=2.03mm^{-1}. For a given efficiency in column 1 the minimum device length L_g is given in column 2. The corresponding Gaussian beam width w and its position Δz are given in column 3 and 4. All lengths are in mm.

calculations (Sect. 4.5). The radiation loss coefficient obtained with the approximate model is 16% smaller than the one obtained with FMM. The values in Table 6.1 for the different radiation loss coefficients differ clearly by less than 16%. For example if we demand 40% efficiency, the required grating lengths differ by only 60µm, which corresponds to a difference of 6%. The Gaussian beam waist and its position on the element differ by 2% and 3%, respectively. The relative difference becomes smaller for higher efficiencies. This attenuation of the effect of 16% of α to 6% by the length is important when considering tolerance aspects. A numerical comparison of the total efficiency estimation with FMM-based model is given in Sect. 6.3.3.

6.1.1. Scaling law

For a given system with a certain efficiency we would like to know how the system must be scaled to obtain the same efficiency for a different spectral linewidth.

With Eq. (6.2) we calculate the maximum efficiency for a given coupling coefficient and thus for a given spectral linewidth. Now we invert the problem and evaluate how the system dimensions need to be modified to obtain the same efficiency for another element with a different spectral resonance width. The simplest approach is to keep η_B, l_C, and l_B in Eq. (6.2) constant, but with a different coupling coefficient. First we look at l_C determined by [Eq. (4.18)], at z=0 and with $\Delta\beta=0$. We define a scaling factor f (f>0). All dimensions (L_g, w, Δz) are multiplied by f whereas the coupling constant α is divided by the same factor f. Then we perform a variable substitution $z'=f\cdot z''$ and we find the initial equation, resulting in the same efficiency. Then we look more closely at the angular efficiency η_B, given in Eq. (4.11). The angular resonance linewidth of the angular response of the filter is proportional to the spectral linewidth, determined by the slope in the λ-θ map (Sect. 3.5). The angular width of the incident collimated Gaussian beam is inversely proportional to the spatial width, w, of the beam. Thus if we multiply the width, w, by the factor f and divide the linewidth by f, we still obtain the same efficiency. Finally we look at the beam losses l_B, given in Eq. (6.1). If we scale the grating length L_g, the incident beam width w, as well as their relative position Δz by f, we find the same loss. This knowledge results in the scaling law: "*To increase the selectivity by a factor of f, it is necessary to scale up the system size by a factor of f*". This prediction is valid when neglecting absorption and scattering losses, as well as fabrication errors. For very weak coupling devices, the absorption α_{abs} becomes a non-negligible factor in addition to the coupling coefficient α_{rad}.

Consequently, further reduction of the filter size while maintaining the linewidth seriously reduces the peak efficiency.

6.2. Simulation with finite incident beam, based on rigorous calculations

The FMM was developed for and works best with one incoming plane wave on an infinite periodic structure. The method presented here treats a finite incident beam in combination with an infinite element. First the angular spectrum of the incoming beam is determined. Since this is done via DFT, the beam decomposition window must be chosen large enough to prevent crosstalk between neighboring (fictive) windows. Then the coefficients $\{R_m, T_m, a_n, b_n\}$ of the grating cell, containing one period of the periodic structure, are determined for each incoming plane wave of the angular spectrum. The field can be computed, for every component of the angular spectrum and the coherent superposition of these field components yields the total field. The incident beam and the grating are described in different spaces that allows to optimize them independently. This offers the possibility to plot the field of very large structures and taking into account subwavelength features. An example of this capability is given in Fig. 6.3, for an incident plane wave and an incident Gaussian beam. The lateral extension of the plotted fields differs by more than a factor of 5000! It is possible to see the detailed mode shape at any given point (Fig. 6.3a,b), as well as the slowly varying mode amplitude (Fig. 6.3f).

We need to give some definitions to clarify the discussion. The *beam decomposition window* is used for the description of the incident beam. A typical size of the beam decomposition window is 100 times the beam diameter. The *grating cell* is used in the FMM routines and contains the strictly repeating section of the element. Its lateral extension is the period of the FMM routines and defines therefore also the spacing between the space harmonics in the

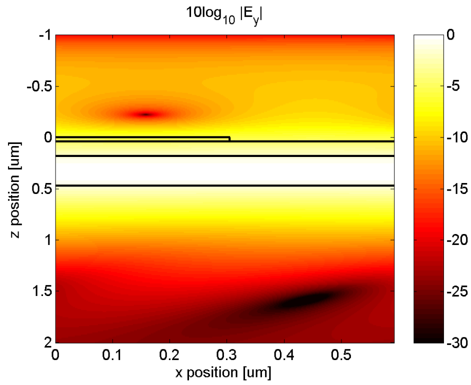

a) Inc. plane wave, 1 period

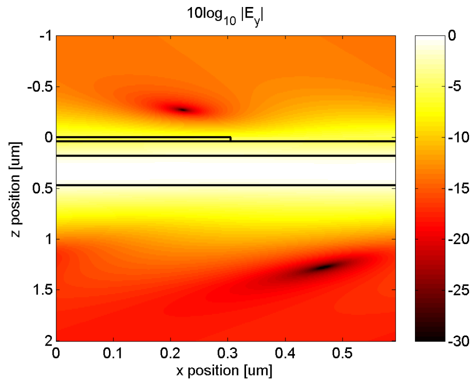

b) Gauss. 500µm, 1 period

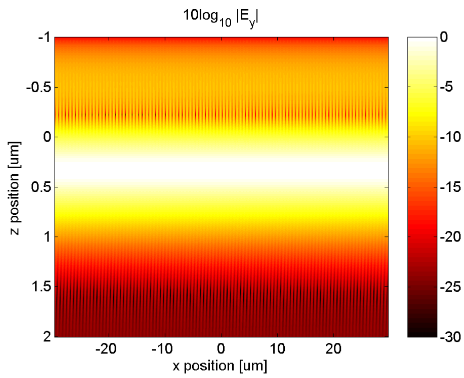

c) Inc. plane wave, 100 periods

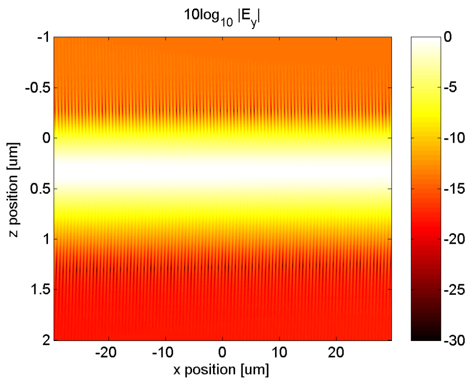

d) Gauss. 500µm, 100 periods

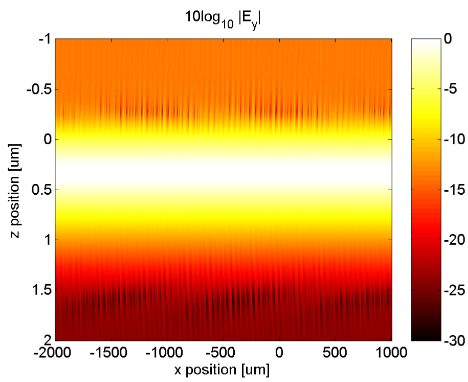

e) Inc. plane wave, ~5000 periods

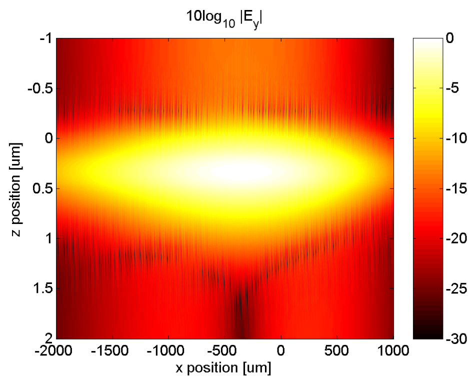

f) Gauss. 500µm, ~5000 periods

Fig. 6.3: Field of the RGF1201 in resonance (λ=1544.6nm, θ=45°), with incident beam omitted. In the left column the incident beam is a plane wave and in the right column a Gaussian beam with waist w_0=500µm impinging on the grating at x=0µm. In the first row (a,b), we can see 1 period, including the contour of the structure. In the second row (c,d) and the third row (e,f), the picture contains 100 periods and roughly 5000 periods, respectively. In the last row, although the number of periods exceeds the number of pixels, the mode shape can still be seen.

FMM routines. Due to computer limitations (Sect. 3.2), the grating cell cannot be chosen too large, i.e. smaller than 0.1mm. In the above implementation the length of the beam decomposition window and the grating cell is independent. In the implementation of Sect. 6.4 they have the same length.

6.2.1. Reflection and transmission

Based on the field calculation it is possible to deduce the total reflectivity and transmissivity of a limited beam. Incident beams with a narrow angular spectrum, as for example collimated beams, can be approximated by only one propagation direction. Within the device, the field distribution can be very complicated. Far away from the structure, there are only propagating fields, and thus no standing wave-fields. On both sides we can place virtual detectors and measure the energy flux and normalize with respect to the incident wave. In transmission into another medium, the propagation direction is changed. We assume collimated beams, and then the reflectivity R and transmissivity T can be obtained [IIZ02]:

$$R = \frac{\int_{-\infty}^{+\infty} |\mathbf{E_R}|^2 \, dx}{\int_{-\infty}^{+\infty} |\mathbf{E}_\mathrm{I}|^2 \, dx} \tag{6.3}$$

$$T = \frac{n_{\mathrm{III}} \cos(\theta_{\mathrm{III}}) \int_{-\infty}^{+\infty} |\mathbf{E}_\mathrm{T}|^2 \, dx}{n_\mathrm{I} \cos(\theta_\mathrm{I}) \int_{-\infty}^{+\infty} |\mathbf{E}_\mathrm{I}|^2 \, dx} \tag{6.4}$$

The expressions are rigorous for a plane wave. With increasing angular spread, the precision decreases. For arbitrary fields, we need to include the angle of each angular spectrum component, as described in Sect. 6.3.2. In the FMM formalism we can profit from the fact that in the incoming medium (region I, chapter 2), it is possible to calculate separately the incident field and reflected field even if they occupy the same surface/volume. An example of the reflection of an incident Gaussian beam with waist w_0 impinging on an infinite RGF1201 is given in Fig. 6.4. The maximum reflectivity drops for smaller incoming beams, with a relative broadening of the reflection peak. In Fig. 6.4d) we can see that the estimated angular efficiency (Eq. 4.11) of the simple model is close to the values obtained with rigorous calculations. The deviation in the case of small beams can be explained by the fact that the thin film reflectivity is not zero, and is contained in the FMM model.

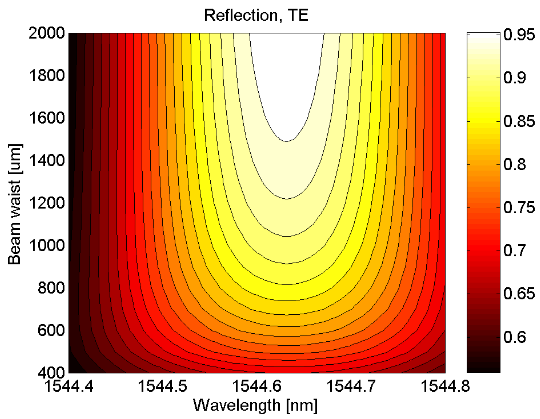

a)

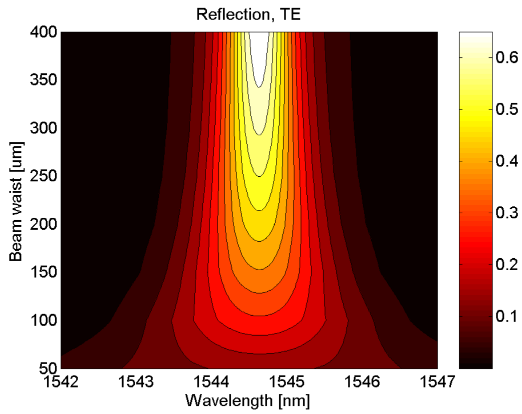

b)

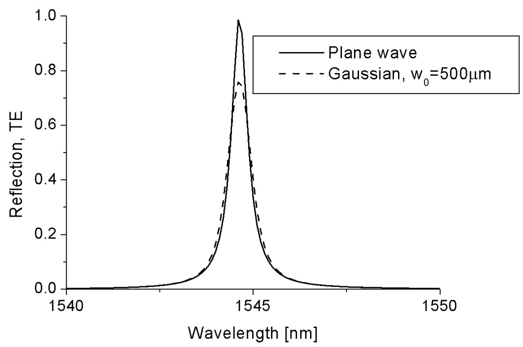

c)

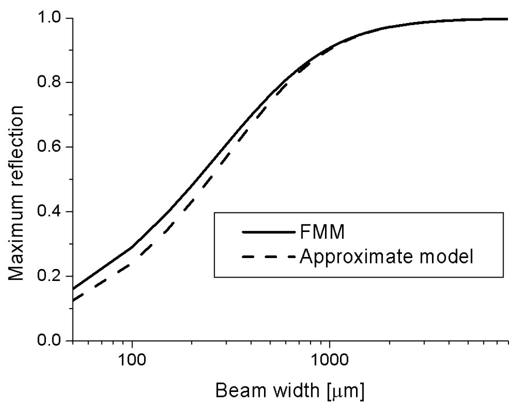

d)

Fig. 6.4: Spectral reflection as a function of the incident Gaussian beam waist on an infinite RGF1201 in a) and for smaller beam waists in b). For comparison in c) the reflection spectrum of an ideal collimated Gaussian beam (dashed line) with a waist of 500µm and the reflection spectrum for an incident plane wave (solid line) are given. In d) the maximum reflection as a function of the beam width obtained from a) and b) (solid line) is compared with the angular efficiency from the simplified model (dashed line) from Eq. (4.11).

6.3. Simulation of finite, large elements

In fully accurate calculations, a finite structure must fit entirely within the grating cell. Since the elements of concern are in the millimeter range, we are not able to simulate these elements in a full rigorous manner, but we can make some approximations to "simulate" a finite structure. So we try to limit the element on both sides.

Definition:

In our system of interest, the oblique incident light is coupled into the backwards propagating waveguide mode (Fig. 6.5). Only one grating diffraction order (-1^{st}) is used and the waveguide is supposed to be single mode. According to Fig. 6.5, we denote the side, limiting opposite to the coupling direction, the *entry side*. Accordingly, the side limiting in the coupling direction, is denoted *exit side*.

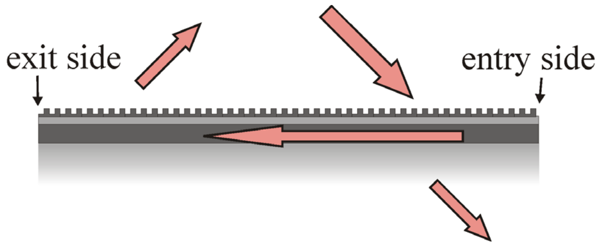

Fig. 6.5: Definition of the entry side and exit side, with respect to the coupling direction. The light coupled into the waveguide propagates to the left. Then the entry side is on the right, and the exit side on the left.

6.3.1. Truncation at the entry side

There is no theoretical limitation on the beam shape of the incident beam. The light impinging on the element only couples in one direction. Thus we can "simulate" a semi-infinite device with a truncated incidence beam. The truncation must be done at the entry side. It should be mentioned that for a correct description of a truncated beam with its sharp change of intensity many times more plane waves are needed in the calculations. An example of a Gaussian beam with w_0=500µm, truncated at the center impinging on the RGF1201 is shown in Fig. 6.6. In Fig. 6.6b), the reflection efficiency is reported as a function of the truncation position. This efficiency is just the angular efficiency η_B. So in order to get the reflection of a semi infinite element, illuminated with a non-truncated incident beam the efficiency must be multiplied by the percentage of the incident beam hitting the grating. For example a Gaussian beam truncated at the center can only create a maximum reflectance of 25%. These edge effects are not taken into account in the simplified model. In the simplified model, the angular efficiency is independent of the truncation position and would be a horizontal line in the Fig. 6.6b), corresponding to the angular efficiency of the untruncated beam. A further system loss is introduced when coupling into the fiber. This is discussed in Sect. 6.3.4.

6.3.2. Termination at the exit side

We are able to calculate the field of a finite incident beam on an infinite structure, but we cannot calculate directly the losses induced by a finite structure. When the light in the waveguide reaches the end of the element, part of the light couples out laterally and the rest is reflected. The reflected light couples out under the same angle, but with opposite sign. In both cases the light does not propagate in the desired direction and is lost. It is possible to estimate the loss of light when looking at the power flux. The power flux per unit area is given by the Poynting vector. In the time harmonic approximation the average Poynting vector is given by Eq. (2.54). We work in the two-dimensional geometry in s-polarization, with linear isotropic materials: E_x=E_z=0. With Eq. (2.60) we find H_y=0. And the Poynting vector is given by

$$\left\langle \mathbf{S}(\mathbf{r}) \right\rangle = \frac{1}{2}\Re\left\{ \mathbf{E}(\mathbf{r}) \times \mathbf{H}^*(\mathbf{r}) \right\} = \frac{1}{2}\Re\left\{ \begin{pmatrix} E_y H_z^* \\ 0 \\ -E_y H_x^* \end{pmatrix} \right\}. \tag{6.5}$$

Then by using Eqs. (2.55) and (2.56), we obtain

$$\frac{1}{2}\Re\left\{ \begin{pmatrix} E_y H_z^* \\ 0 \\ -E_y H_x^* \end{pmatrix} \right\} = \frac{1}{2\omega\mu_0}\Re\left\{ \begin{pmatrix} -E_y \left(i\,\partial E_y / \partial x \right)^* \\ 0 \\ -E_y \left(i\,\partial E_y / \partial z \right)^* \end{pmatrix} \right\} = \frac{1}{2\omega\mu_0}\Re\left\{ \begin{pmatrix} E_y i\,\partial E_y^* / \partial x \\ 0 \\ E_y i\,\partial E_y^* / \partial z \end{pmatrix} \right\}. \tag{6.6}$$

In order to compare with the simplified model, the coordinate system has to be identified. In the approximate model with the waveguide as the central element, for historical reasons, the z-direction is along the waveguide and the x-coordinate the transverse direction. In the FMM formalism the axes are inverted. So the direction along the waveguide corresponds to the x-axis and the transverse direction to the z-axis. We stay in the axis definition of the FMM calculations. Then the power flux through the cross section of the waveguide is:

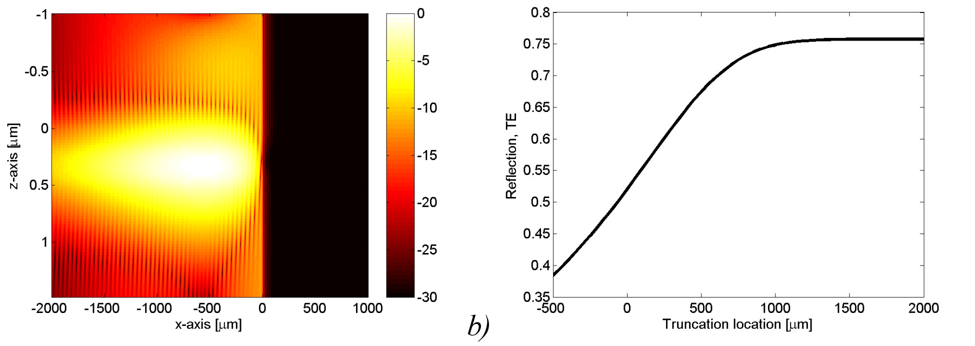

a) b)

Fig. 6.6: Truncated incident beam to simulate a semi-infinite device. In a) the field distribution (dB-scale) of a Gaussian beam with w_0=500µm, truncated at its center position (x=0µm), impinging on the RGF1201 is given. Because of this edge in the light distribution, the angular spectrum is affected and there is less light to fulfill the coupling condition, resulting in reduced reflectivity. In b) the reflection of the truncated beam with respect to the truncated incident beam is given.

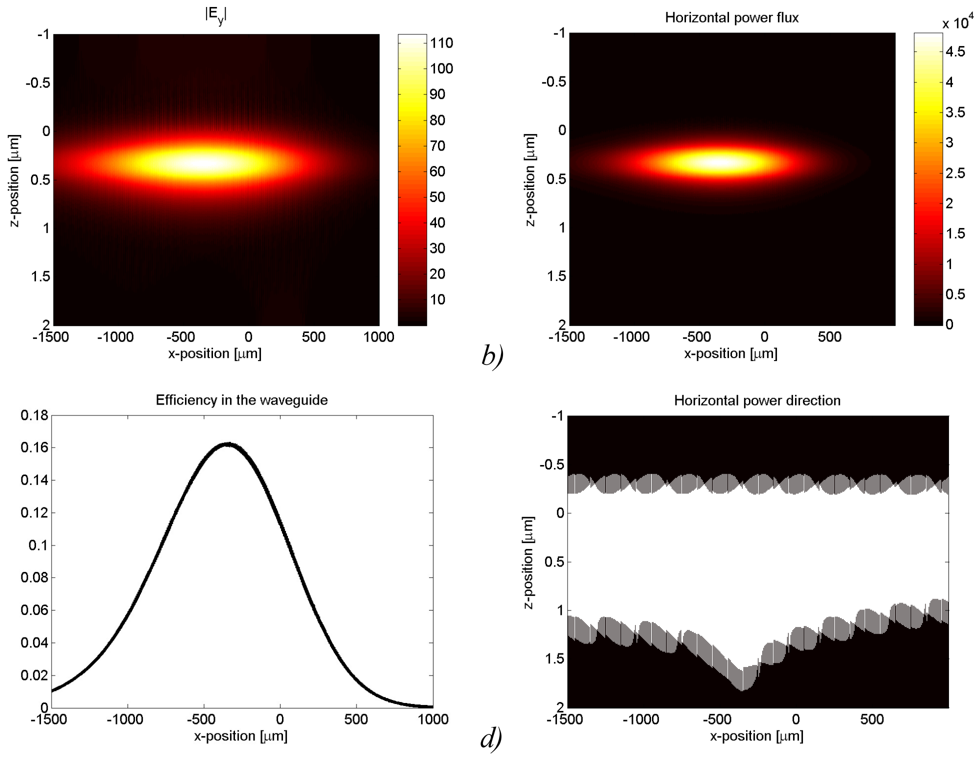

a) b) c) d)

Fig. 6.7: Coupling analysis. A Gaussian beam with waist 500µm impinging on the infinite RGF1201 at x=0 µm at 45° with λ=1544.6nm. a) The field amplitude and b) the horizontal power flux are shown. In this example, their shapes are similar. The efficiency defined as the power flux through the section of the waveguide with respect to the total incident power flux is given in c). The vertical integral along z of Eq.(6.9) was performed in the range z=–1...1.5µm. In d) it is shown whether the dominant contribution comes from the light coupled in the waveguide (white) or the incident and coupled out light (black).

$$P_{wg} = \int \langle \mathbf{S}(\mathbf{r}) \rangle \cdot d\mathbf{n} = -\frac{1}{2\omega\mu_0} \int \Re\left\{ E_y i\, \partial E_y^* / \partial x \right\} dz \tag{6.7}$$

with **n** being the surface normal, the unit vector in the –x direction. In Eq. (6.7), the total power flux is considered, containing the guided, reflected and transmitted light. The guided light has the opposite sign of the horizontal power flux of the transmitted and reflected light. Consequently the total power flux is always smaller than the power flux of the guided light. So the integral should be taken basically over the waveguide mode. In a similar way, the power flux of the incident beam is determined. The incident collimated beam is a TEM wave and thus the Poynting vector, the magnetic and electric fields are orthogonal. Then the power flow through the section, parallel to the element surface reduces to

$$P_{in} = \int \langle \mathbf{S}(\mathbf{r}) \rangle \cdot d\mathbf{n} = \cos(\theta) \frac{1}{2} \sqrt{\frac{\varepsilon_0}{\mu_0}} n_{in} \int \left| E_y \right|^2 dx, \tag{6.8}$$

where θ is the angle of incidence. In order to compare this model to the model presented in chapter 4, we introduce the power efficiency η at position x, as the ratio of the power flux in the waveguide to the incident power flux

$$\eta(x) = \frac{P_{wg}(x)}{P_{in}} = \frac{-\frac{1}{2\omega\mu_0} \int \Re\left\{ E_y i\, \partial E_y^* / \partial x \right\} dz}{\cos(\theta) \frac{1}{2} \sqrt{\frac{\varepsilon_0}{\mu_0}} n_{in} \int \left| E_y \right|^2 dx} = \frac{1}{\cos(\theta) k_0 n_{in}} \frac{\int \Im\left\{ E_y\, \partial E_y^* / \partial x \right\} dz}{\int \left| E_y \right|^2 dx}. \tag{6.9}$$

The derivative in the above equation makes the Poynting vector sensitive to the choice of the grid. A dense grid is necessary and sometimes it can be useful to average the Poynting vector along the propagation direction. An example is shown in Fig. 6.7 for a Gaussian beam with w=500µm impinging on the RGF1201. As stated above, we cannot distinguish in the calculations the contributions in the power flux of the guided light from the contributions coming from the out-coupled light and the incident/transmitted light, with opposite horizontal flux directions. To clarify this, a binary map with the dominant coupling direction is shown in Fig. 6.7d). The comb artifacts come from the fact that the sampling is not dense enough for complete resolution. As expected, the guided light (white) is dominant in the waveguide. Outside the waveguide mode, the other contributions (black) are dominant. With the same parameters, the efficiency within the approximate model is calculated (Fig. 6.8). The curve shapes are similar. However the maximum efficiency obtained with FMM calculations is

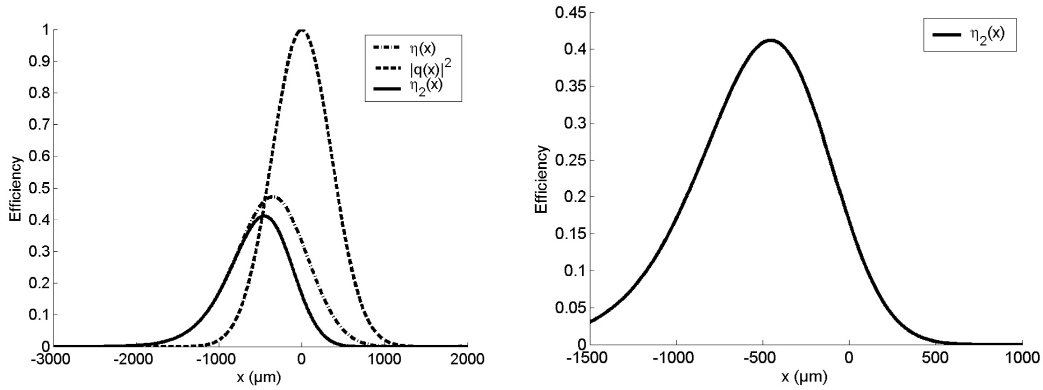

Fig. 6.8: Coupling out losses with the simplified model. The dashed line corresponds to the normalized incident beam, the dash-dotted line to the efficiency $\eta(x)$, with respect to the incident power between x and infinity and the solid line corresponds to the efficiency $\eta_2(x)$, with respect to the total incident power. The general shape is similar to the shape of Fig. 6.7, but the efficiency is higher.

lower. One explanation is the fact that in the power flux determination of the rigorous model, the incident and out-coupled light is still present and the limited angular efficiency is already included. Another difference comes from the fact that in the approximate model, the angular spectrum spread cannot be handled correctly. In Fig. 6.4 it could be shown that even if the central angle of the incident beam corresponds to the resonance angle, the maximum efficiency is only 75% due to the angular spread of the incident beam. However in spite of the differences the approximate model gives good predictions of the light distribution. This is important since the rigorous calculations are very slow and an optimization is not feasible, in contrast to the coupling model, where almost realtime calculations are possible.

A second possibility to obtain the reflectivity is to just compare the vertical power flux just above the element (where it is possible to separate reflected and incident light) over the element extend with the total incident power flux.

6.3.3. Comparison of the efficiency predictions within the approximate model and the rigorous calculations

To compare the approximate model and the model with the rigorous calculations within the above-described approximations, we consider a concrete example. An incident Gaussian beam with waist w_0=500μm impinges on the RGF1201 at x=1mm, under 45° with λ=1544.6nm, coupling in the –x direction. The length of the device is 1.5mm, corresponding to a Δz of 0.5mm.

Then in the approximate model, 8.1% of the incident beam is lost (i.e. l_B=8.1%) and 16.4% of the light is not coupled out before the end of the device (i.e. l_C=16.4%). The angular efficiency η_B is 73.7%. So the total predicted efficiency is *55.7%*.

In the more rigorous model, first the total incident light power, with the non-truncated beam, is determined as the reference. Then the reflected power flux of the truncated incident beam is determined along the finite element. In this example 63.7% of the truncated beam is reflected. This corresponds to 58.7% reflection of the non truncated incident beam.

When comparing the two numbers, 55.7% from the simple model and 58.7% from the second model, a good agreement can be found.

We think it is worthwhile to give an indication of the calculation speed to see the need for the simple model. In the simple coupling model, 0.03 seconds are needed to obtain the result, whereas in the second model 13.9 hours are required! The second model requires more time by a factor of over one million! The calculation time for the second method depends heavily on the sampling of the fields and the number of retained orders of the angular spectrum. For example, a non-truncated incident Gaussian beam, needs only half an hour for the same calculation accuracy. The long calculation times of the second model makes an optimization impractical.

6.3.4. Fiber coupling efficiency

The reflected and transmitted light must be coupled into fibers (Fig. 6.9). It is necessary therefore to estimate the fiber coupling efficiency. As can be seen (Fig. 6.3) the beam shape can be affected by the coupling process, especially through the added exponential tail (Fig. 4.8). So we expect a reduced coupling efficiency. This is not only true in reflection, but in transmission as well. In the later case it is a desirable effect because it reduces the crosstalk between R and T. We work in classical incidence, i.e. grating grooves perpendicular to the plane of incidence. Then the problem can be reduced by one dimension. First of all the beam distribution before the collimators must be determined (perpendicular to the beam propagation direction), in reflection and transmission, denoted ϕ_R and ϕ_T (Fig. 6.9). Here we can benefit from the FMM-formalism and simply determine the field along any desired line. Then we add the orthogonal dimension, unaffected by the grating to form the two-dimensional incident field $\phi(x,y)$ on the collimator. Next the single mode fiber mode is propagated back to the collimator. And finally the fiber coupling efficiency is determined by the field overlap. This is only true if the collimator does not act as the limiting device. If this were the case, then every beam has to be propagated through the collimator and the coupling integral must be evaluated on the fiber input face.

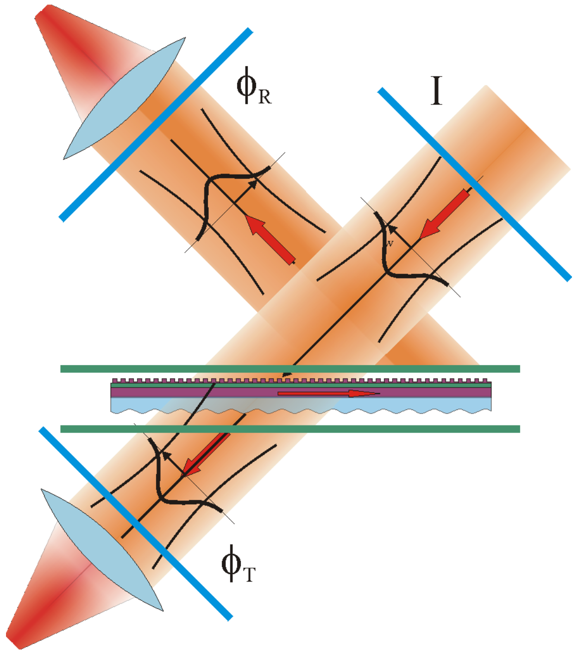

Fig. 6.9: The 1D-fields are determined before the collimator, at ϕ_R and ϕ_T, perpendicular to the beam propagation direction. Then the 2D fields (including the direction, unaffected by the grating) are determined and the coupling efficiency integral is evaluated.

The fundamental mode of the single mode fiber is approximated by a Gaussian distribution. When emerging from the fiber we assume free space propagation of the Gaussian beam [SIE86], with the waist equal to the fiber core radius at the fiber end. The collimator is then approximated by a thin perfect quadratic lens [GOO96], with focal length equal to the distance from the fiber. With the analytical solution of the free space propagation of the Gaussian beam, and multiplication with the phase profile of the lens, the reference modal field $\psi(x,y)$ is determined.

The fiber coupling efficiency η_f is given by

$$\eta_f = \frac{\left|\int \phi(x,y)\,\psi^*(x,y)\,dx\,dy\right|^2}{\int\left|\phi(x,y)\right|^2 dx\,dy \int\left|\psi(x,y)\right|^2 dx\,dy}. \tag{6.10}$$

The distance between the fiber and the position of the perfect lens is chosen such that the size of the modal field corresponds to the size of the Gaussian beam in the direction where the field is not affected by the grating. An example with an incident Gaussian beam having a width of 500µm incident on the RGF1201 is shown in Fig. 6.10. There it can be seen that the efficiency in transmission is much more strongly affected than in reflection. The influence of the beam width is important.

6.3.5. Losses and crosstalk

Within the system losses and crosstalks must be evaluated. The efficiency is defined as the ratio between the light in the corresponding fiber and the incident light. The efficiencies in reflection and transmission, respectively, are then

$$\begin{aligned} \eta_r &= \eta_{f,r} \cdot R \\ \eta_t &= \eta_{f,t} \cdot T \end{aligned}, \tag{6.11}$$

with $\eta_{f,r}$ and $\eta_{f,t}$ the fiber coupling efficiency in reflection and transmission, respectively, and R and T the reflectivity and transmissivity, respectively. η_r corresponds to the portion of the desired signal that is redirected to the drop port and η_t the portion of light which remains in the through port. In the ideal resonance case η_r=1 and η_t=0. The loss is the portion of the desired signal that does not arrive in the drop port and the crosstalk is the portion which leaks into the through port. Then the loss and crosstalk are given by

$$\begin{aligned} \text{loss} &= 1 - \eta_{f,r} \cdot R = 1 - \eta_r \\ \text{crosstalk} &= \eta_t = \eta_{f,t} \cdot T \end{aligned}. \tag{6.12}$$

The efficiency, loss, and crosstalk of the RGF1201 as a function of wavelength and beam width are given in Fig. 6.11. The evaluated spectrum is very narrow (0.4nm). Then it can be said that efficient crosstalk suppression is only possible within a very limited range. In addition, these results confirm that large beams show better performance.

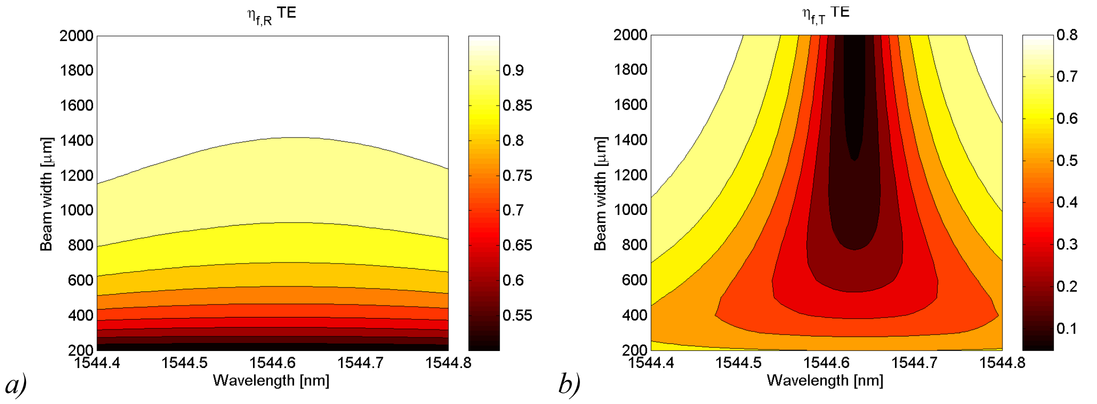

Fig. 6.10: Fiber coupling efficiency for an incident Gaussian beam with width 500µm on the RGF1201. a) In reflection and b) in transmission.

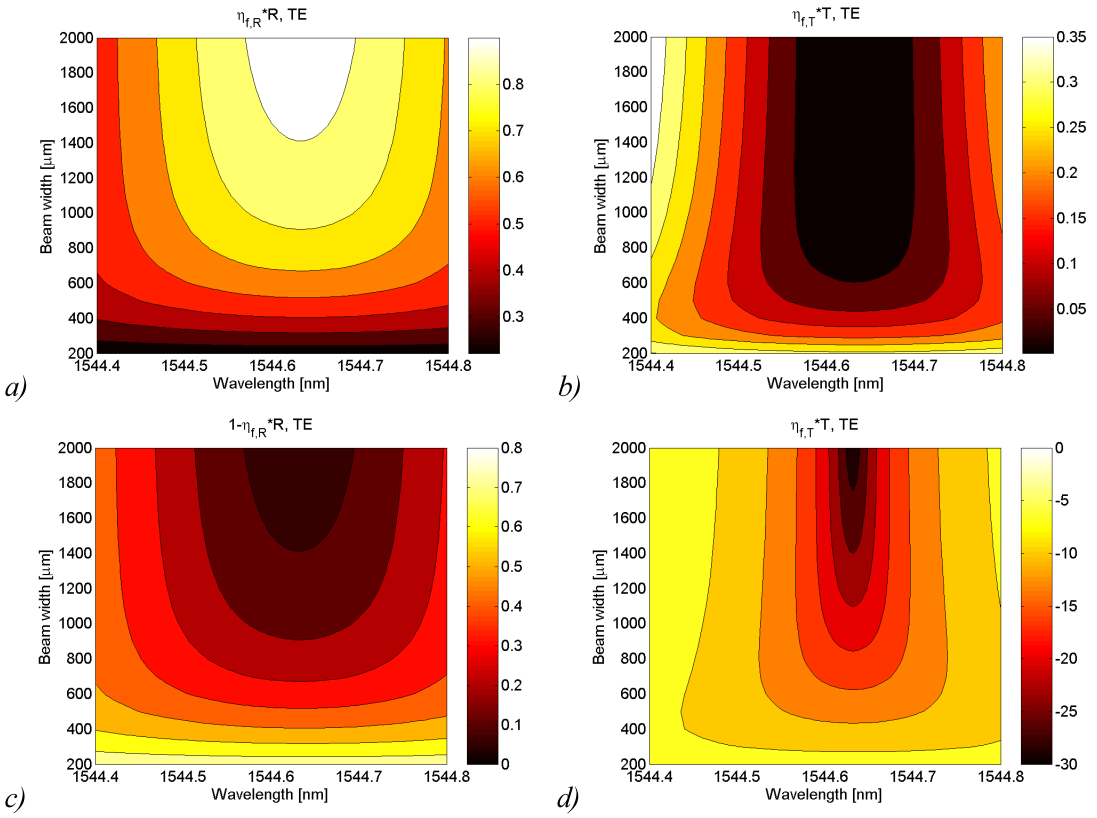

Fig. 6.11: System performance of the infinite RGF1201. The efficiencies are given a) in reflection and b) in transmission. The loss of the reflected channel is indicated in c) and the corresponding crosstalk in dB-scale in d). The ideal case would correspond to homogeneous regions with a) equal to 1, b) equal to 0, c) equal to 0, and d) equal to –infinity.

6.4. Simulation of finite beams and finite devices – strong coupling device

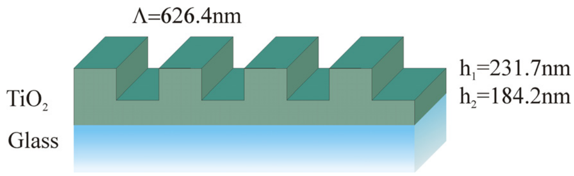

Fig. 6.12: RGF0703, strong coupling device. The strong coupling device contains no separation layer, and the grating grooves are deeper than the waveguide thickness. The fill factor is 0.358, with n_{TiO2}=2.298, and n_{Glass}=1.51.

Weak coupling devices have long interaction lengths and thus require a significant element size for complete coupling. This makes the direct numerical calculation of finite structures very difficult. Therefore a strong coupling device was designed with the goal of scaling down the interaction lengths to be able to place the whole structure, including the incident beam in the grating cell. It is evident that this device no longer satisfies the shallow grating approximation (Sect. 3.3). In order to realize stronger coupling, the separation layer was omitted and the grating height dramatically increased, but the materials are still the same. The designed device, called RGF0703 is shown in Fig. 6.12. The radiation loss coefficient obtained with the FMM is 124.9mm^{-1}, having an associated coupling length of 8.01μm. So the coupling power of this device is more than a factor 60 stronger than the RGF1201. A Lorentzian fit reveals a peak width of 32nm with a reflection maximum for λ=1545nm. This is consistent with the fixed relationship between the line width and the coupling coefficient. The angular FWHM is 5.0°, so even the slope (6.4nm/°) is conserved.

6.4.1. Implementation

The way the field is determined differs from the previous calculations (Sects. 6.2, 6.3) in order that the beam decomposition window and the grating cell have the same size. Then the incident beam is not only a plane wave, but a whole set of plane waves forming a finite beam. This has the advantage that the final field can directly be determined and the calculation time does not depend on the incident beam shape. The drawback is that the angular spectrum resolution is fixed by the grating cell. Adaptation in order to better resolve the incident beam is no longer possible. The whole coupling process must fit in the grating cell and no lateral light propagation outside the grating cell should occur. This light would penetrate into the next grating cell, resulting in aliasing of the fields. This requirement can partially be relaxed by introducing matched layers [LAL00]. These are artificial layers on both sides and serve to absorb the laterally propagating light to prevent aliasing. The material at the edge of the cell is extended with the same real part of the refractive index and the imaginary part is continuously increased towards the edge. A reasonable trade-off between computational cost and accuracy is to take a width on the order of a wavelength. The quality of these boundaries can directly be observed when laterally propagating light hits the boundary and its reflection creates interferences. There exists an extension [SIL01] with the use of perfect matched boundaries [BER94]. This implies the use of magnetic materials and the FMM would need to be adapted. The use of absorbing layers makes the correct reflection and transmission coefficient determination more difficult. The matched boundaries are only applied in region II (modulated region). Sometimes it is necessary to introduce additional cover and substrate layers to be able to apply matched boundaries.

An example of the field distribution based on the RGF0703 is given in Fig. 6.13. The incident Gaussian beam with its waist w_0=10μm hits the structure at 48.5μm. The element has a length of 100 periods plus two wavelengths absorbing boundaries, thus 65.7μm. The wavelength is 1545nm and the AOI is 45°. The resemblance to the situation of Fig. 6.3f) can clearly be seen, including the characteristic blocking of the central part of the transmitted beam. The field enhancement is weaker due to the shorter coupling length (smaller Q-factor of the cavity).

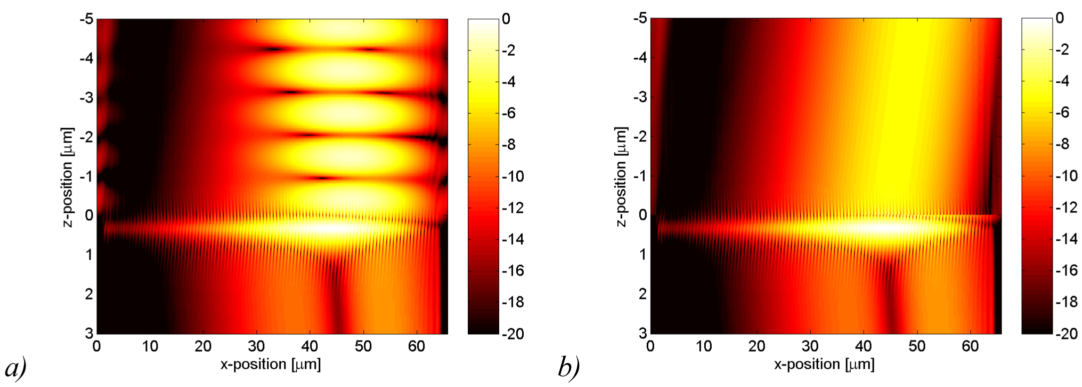

Fig. 6.13: RGF0703 fields in dB scale. The incident Gaussian beam with a waist of 10μm is centered at 48.5μm. a) With the incident beam, and b) without the incident beam.

6.4.2. Reflection / Transmission coefficients

In the case of the finite element, the beam size is relatively small. So the approximation of a collimated beam in the Poynting vector calculation of Eq. (6.8) is no longer valid. The vectorial Poynting vector must be calculated. Then, following Eq. (6.6), we determine the power flux parallel to the device surface

$$P_{in} = \int \left\langle \mathbf{S}(\mathbf{r}) \right\rangle \cdot d\mathbf{n} = \frac{1}{2\omega\mu_0} \int \Re\left\{ E_y i\, \partial E_y^* / \partial z \right\} dx \tag{6.13}$$

and the resulting efficiency is, according to Eq. (6.9)

$$\eta(x) = \frac{P_{wg}(x)}{P_{in}} = -\frac{\int \Im\left\{ E_y\, \partial E_y^* / \partial x \right\} dz}{\int \Im\left\{ E_y\, \partial E_y^* / \partial z \right\} dx}. \tag{6.14}$$

6.4.3. Finite element

With the above implementation we can calculate the field for any kind of structure, only limited by the size. For the subsequent calculations we use a grating cell with 100 periods of the RGF0703, with matched boundaries in the element layers (region II). The incident Gaussian beam with its waist w_0=10µm impinges with its center after 75 periods (48.5µm). In Fig. 6.14 two situations are shown: a) the device is shortened from the entry side, thus from the right, and b) shortened from the exit side, thus from the left. In the first case a fraction of the light does not imping on the device and propagates through. The incident beam is omitted for better presentation. At the right end of the device, edge diffraction occurs which translates in a locally enhanced transmission. In the second case there is not enough waveguide length to complete the outcoupling process. Part of the light in the waveguide reaches the end of the devices and either couples out within a light cone or is reflected and coupled out in the wrong direction.

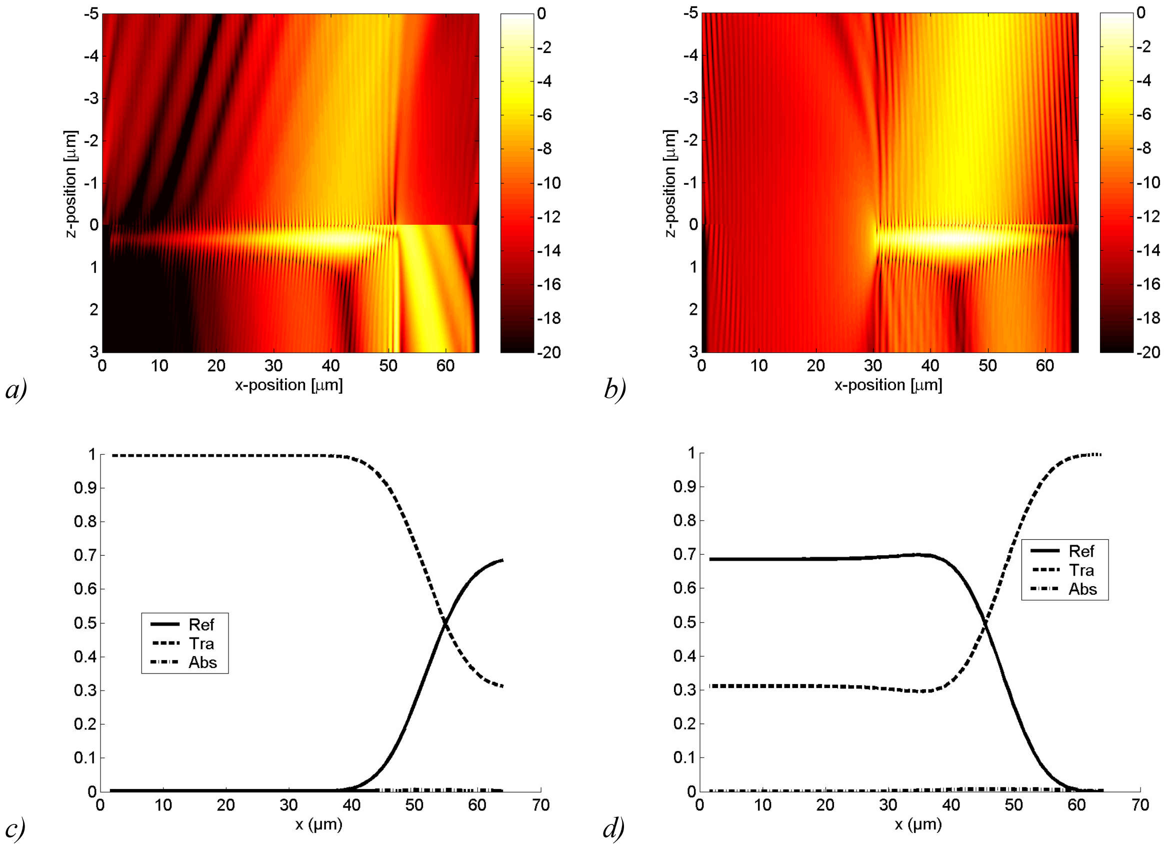

Fig. 6.14: Effects of finite device size. In the figures the incident beam has been omitted for clarity. The grating cell contains 100 periods of the RGF0703. The incident Gaussian beam with waist 10µm hits the grating at 75 periods from the left. In a) there are 80 grating periods and 20 empty periods, corresponding to the device ranging from x=1.55µm to x=51.6µm. Then a part of the incident beam can propagate through. At the end of the element (x=51.6µm), diffraction occurs resulting in enhanced transmission. In b) the grating consists of 54 periods, counted from the right, corresponding to the device ranging from x=30.4µm to x=64.1µm. The guided light reaches the end of the device. Most of the guided light is coupled out and propagates away. In c) and d) the transmission and reflection as a function of the position of the device edge is given. In c) the device is shortened at the entry side and in d) at the exit side. Absorption occurs when light hits the lateral absorption layers, located at the border.

6.4.4. Accuracy of the truncated incident beam approximation

Here we want to show that the truncated incident beam assumption of Sect. 6.3.1 to describe the semi-infinite beam is a valid approximation. This approximation in the case of the strong coupling device, the RGF0703 (Fig. 6.12), is compared with the finite device calculations. The basic situation is the same as before. A Gaussian beam with waist 10μm impinges on the grating (consisting of 100 periods of the RGF0703 and matching boundaries) after 75 periods. First the fields are determined and then the reflection and transmission coefficients are calculated, as shown in Fig. 6.15. For the finite device this has already been done in Fig. 6.14c). The truncation location of the incident beam is defined with respect to the beam center. For comparison, the coordinates need to be adapted, corresponding to an offset of 48.5μm. Then the reflection and transmission coefficients of the device with the truncated incident beam, with respect to the non-truncated incident beam are determined. The absorption in Fig. 6.15c) is defined as the complement to 100% of the field of the non truncated incident beam. It corresponds roughly to the truncated part of the beam. Then it is possible to compare the obtained reflection with the reflection obtained with the finite device, Fig. 6.15d). A very reasonable agreement can be found. It is clear, from a physical point of view, that the results can't be exactly the same. The main differences occur at the edges, with its strong diffraction. So the difference is smaller for larger, weak coupling devices and we can conclude that the truncation of the incident beam for the elements we are interested in (Sect. 3.3) is a valuable approach to simulate semi-infinite devices.

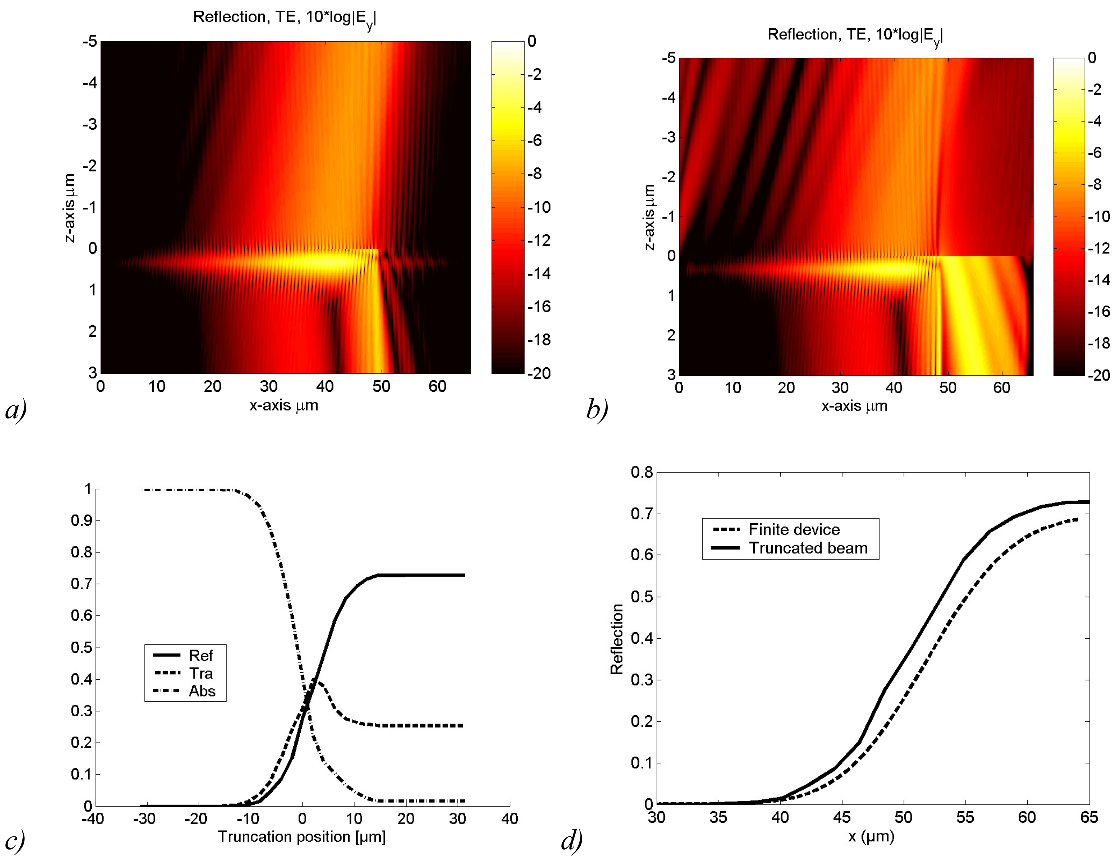

Fig. 6.15: Comparison of the truncated beam and the semi-infinite device. A Gaussian beam (incident beam omitted) with waist 10µm hits the grating after 75 periods (48.5µm) under the resonance condition. In a) half a Gaussian beam impinges on an infinite grating. In b) a Gaussian beam impinges on a finite device (75 of 100 periods). When neglecting the transmitted part of the beam not hitting the grating in b), the field distributions are very similar. In c), the reflected, transmitted and absorbed (=complement to 100%) parts of the truncated beam on an infinite device, with respect to the untruncated incident beam are shown. This allows a comparison with the reflected part of a finite device with untruncated illumination beam, shown in d). The zero truncation position of the beam is at 75 periods (48.5µm) of the finite device.

6.5. Affecting the line shape

The spectral lineshape of a device containing a simple resonance (only one excited mode) results in a Lorentzian peak shape and when we are not working in a thin-film extremum, then the peak shape becomes asymmetric [DAY96]. A filter in demultiplexer applications should ideally show a rectangular spectral response. The Lorentzian shape exhibits a slow decay on both sides of the peak. We want to examine how the spectral response can be affected. Only a few papers about spectral shape control have been published. Most of them optimize the Lorentzian decay tails, by changing the thin film reflectivity. The tails depend essentially on the curvature of the thin-film band (an example of different thin-film band curvature is given in Fig. 3.14) and the AR-quality of the thin film reflectivity. The optimized spectral reflectance can decay rapidly (large band curvature), at the cost that after the minimum the reflectance increases faster [THU03]. The only effective method for improving the central peak shape present in the literature is cascading RGFs [JAC02]. The RGF have to be spatially separated by a minimum distance to prevent mode coupling, which would cause mode coupling. Then the same principles as in the design of thin film filters are applied, namely simple interference. The problem therein is that several RGFs are needed and they have to be aligned carefully, which is very challenging with current technology.

6.5.1. Doubly structured waveguide

We want to look at other possibilities, namely grating superposition. A planar waveguide is modulated on both sides, but with a different period. It would be possible to use multiple gratings on one side to create similar effects. The periodic modulations on both sides have periods close to each other. Then we look at the case where the resonance curves of the structure with identical periods for period 1 and for period 2 should overlap. In the FMM formalism the grating cell has to contain a strictly periodic section of the element. The length of this section is denoted as the equivalent period. If the ratio of the 2 periods is irrational, then the equivalent period is infinity and we cannot calculate it. By allowing a maximum decimal precision (prec), the equivalent period becomes finite. It can be written as

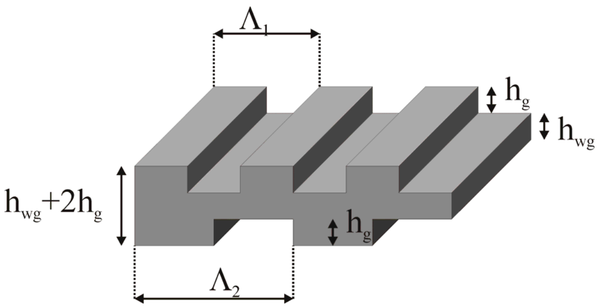

Fig. 6.16: Doubly structured waveguide, RGF1103. With grating height h_g=170.5nm, the waveguide thickness h_{wg}=96.4nm, period 1 Λ_1=664nm, period 2 Λ_2=672nm (equivalent period, Λ_{eq}=55776nm) resulting in a FWHM=14nm. The fill factors are 0.5.

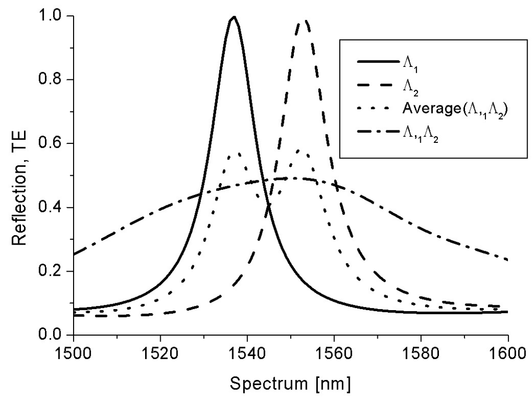

Fig. 6.17: Reflection spectra of the RGF1103. The reflection peaks reaching 100% reflection correspond to the cases where the periods are equal. A large difference between the weighted sum of the individual peaks (dotted line) and the spectrum obtained with two different periods (dashed-dotted line) can be seen. In the last case, an important amount of light is not in the specular order and thus is considered as stray light.

$$\Lambda_{eq} = \frac{\Lambda_1 \Lambda_2}{\mathrm{prec} \cdot \mathrm{gcd}\left[\mathrm{round}\left(\frac{\Lambda_1}{\mathrm{prec}}\right), \mathrm{round}\left(\frac{\Lambda_2}{\mathrm{prec}}\right)\right]}, \tag{6.15}$$

with gcd the "greatest common divisor" operator. For the numerical implementation, we are interested in adjacent period lengths leading to a small equivalent period. The equivalent period is minimum when both periods are multiples of the difference of the periods. Then

$$\Lambda_1 = \mathrm{n} \cdot \Delta\Lambda, \Lambda_2 = (\mathrm{n}+1)\Delta\Lambda \Rightarrow \Lambda_{eq} = \Lambda_1(\mathrm{n}+1). \tag{6.16}$$

Bearing in mind that the computation time scales with the number of retained orders cubed. Therefore it is advisable to minimize the equivalent period. A new device was designed, shown in Fig. 6.16, belonging to the strong coupling devices. Then the spectral response with two equal periods, corresponding either to period 1 or period 2, as well as the spectrum of the device with two different periods were calculated (Fig. 6.17). We can state that the spectral reflectivity of the device with two different periods is very different from the weighted sum of the spectral reflectivity with two equal periods. So we cannot simply add the spectral responses. The specular transmission in the case of two different periods is rather low, clearly below 50%, with a minimum in the resonance region. The difference in the specular reflection is essentially stray light. This can be explained by the fact that the light coupled in, can couple out through both gratings. So roughly half of the light couples out through the "wrong" grating, leading to enhanced stray light.

As a conclusion, it can be said that the approach of the grating superposition in combination with a waveguide is not the best way. Neither the efficiency, nor the peak width of the situations with equal gratings can be maintained.

6.5.2. Wave localization

A subject related to the doubly structured waveguide is wave localization [AVR90]. The aim of this section is to show the potential of the use of wave localization in a switching device, with a maximum displacement of half the grating period, which would allow the application of very stiff actuator designs for fast switching applications. We start by looking at a plane wave, which is itself not localized. A grating in combination with an adjacent waveguide creates a periodic field deformation of the incident plane wave. A second adjacent grating adds a second perturbation and the resulting resonance depends strongly on the relative position of the gratings. This phenomenon is known as wave localization.

As an example the RGF1201 was "mirror unfolded", so that the waveguide is embedded between two equal separation layers with each one the same grating on the top. A new design was made in order to get symmetric line shapes, named RGF0503 and shown in Fig. 6.18. The design is such that for an angle of incidence of 45° resonance occurs for wavelengths around 1545nm. The reflectance as a function of the wavelength and the relative grating offset is given in Fig. 6.19. It can be seen that the reflectance heavily depends on the relative grating offset. Maximum resonance occurs for no or half a period offset, with different strengths. The positions of the maxima with respect to the offset parameter don't shift with a different incidence angle. In the spectral reflectivity of Fig. 6.19 two situations can be identified. The case of the symmetric structure (no grating offset), with the resonance peak at 1545.0nm and a

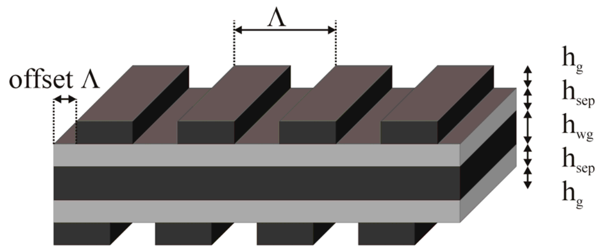

Fig. 6.18: RGF0503. This design is adapted to show wave localization, with grating thickness h_g=35nm, separation layer thicknesses h_{sep}=199nm, waveguide thickness h_{wg}=168nm, grating period Λ=645nm and fillfactor=0.5. The waveguide and the gratings are TiO_2 (n_{TiO2}=2.298) and the separation layers are SiO_2 (n_{SiO2}=1.444).

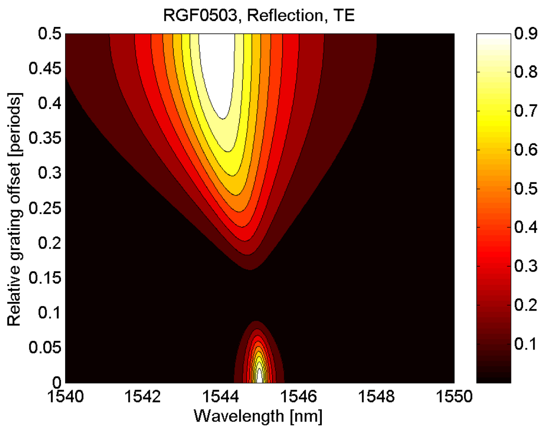

Fig. 6.19: Wave localization for 45° AOI. Maximum reflectance is obtained for 0 and 0.5 relative grating offset, whereas minimum reflectance is obtained for a relative grating offset of 0.11 periods.

FWHM of 0.44nm and the case with a grating offset of half a period with the resonance peak at 1543.9nm and a FWHM of 2.78nm. In the symmetric case the peak is narrower and the field enhancement is stronger than in the second case. Between the two resonance reflection maxima lies a minimum. In the case of the RGF0503 the minimum is obtained for a relative grating offset of 0.12 grating periods. In that case, the field can neither couple in the structure nor couple out of it. A relative shift of 0.12 grating periods can provoke therefore a change between 0% and 100% reflection. In this case 0.12 periods correspond to 77nm. A lateral shift of the grating of half the period (322.5nm) can change the peak width by a factor of 6.4. In practice it is important to notice that the spectral response depends on the relative shift. So when assembling the device, the required absolute precision is much more relaxed.

7. Conclusion

In the present work we investigate the design and characterization of a tunable optical filter for use in a compact add-drop multiplexer. The optical filter is a resonant grating filter (RGF) consisting essentially of a planar waveguide and a grating parallel to the surface. A resonance occurs when the incoming light is diffracted by the grating and matches a mode in the waveguide. Numerous aspects of modeling, design optimization, fabrication tolerances and performance characterization are addressed. A particular emphasis is given to the miniaturization for use in a MEMS microsystem for large-scale manufacturing.

Specifically, we investigated a tunable, oblique incidence resonant grating filter covering the C-band as an add-drop device for incident TE-polarized light. The filter can be tuned by tilting a MEMS platform onto which the filter is attached. The fabrication tolerances were addressed. In good correspondence with simulations, measurements indicate a negligible change in the shape of the resonance peak from 1526nm at 45° angle of incidence to 1573nm at 53° with a full width at half maximum of 0.4nm. In this range the shift of the peak wavelength is linear with respect to changes in the incident angle. The fabrication process is straightforward and adapted for large-scale manufacturing.

An efficient approximate model was developed to predict the maximum obtainable efficiency for a finite device. At oblique incidence, the angular and spectral selectivity are related by the slope in the dispersion map. A narrow spectral linewidth requires a large beam (small angular spectrum), which will only partially illuminate the device. The above case with 0.5nm spectral width and a slope of 6.4nm/° in the dispersion map, requires at least a 1.3mm filter length for 50% power reflection. To obtain this reflection, the incident Gaussian beam has a width of 0.37mm and its center is located 0.37mm from the edge.

The rigorous grating models are modified to treat finite incident beams with Gaussian as well as arbitrary shapes. A finite beam reduces the maximum obtainable reflectivity, due to the angular mismatch. The reflectivity of a Gaussian beam with 1mm diameter impinging on the RGF (RGF1201, 0.5nm linewidth) is reduced to 75%. The reflected and transmitted beam shapes under resonance are affected by the coupling. This distorted beam will reduce the coupling efficiency. We calculated the fields of a semi-infinite element illuminated by a Gaussian beam at the collimator plane. The fiber coupling efficiency is then calculated. Taking into account the overall reflection and transmission coefficients, the total efficiency and crosstalk to other channels are determined. For example, a perfectly collimated Gaussian beam of 1mm diameter impinging on an infinite device under resonance leads to a total reflection efficiency of about 50%. The maximum crosstalk suppression is on the order of 10dB. Larger beams show better performance. A Gaussian beam with 4mm diameter can lead to a total efficiency above 90% and a crosstalk suppression of 30dB. Regarding the tolerances with respect to efficiency and crosstalk the device is more suitable to work with at least 200GHz channel spacing.

Polarization independent configurations were studied, with a simple grating as well as with crossed gratings. Efficient devices need to have mirror symmetry. In full conical mount a design is presented, that is tunable over the C-band. Resonance occurs for all incoming polarization states, but with different linewidths. This design is more demanding on fabrication tolerances and a deviation from the design values often results in a spectral peak splitting for arbitrarily polarized incident light.

A strong coupling device is designed, so that the finite-size aspects can be handled in a fully rigorous manner. The validity of the approximations for the finite size aspects of the weak coupling device is examined. The approximations are valid when most of the incident beam is on the grating. Additional interactions were examined, such as wave localization and double grating structures. The study on possible peak shape changes led to the conclusion that unfortunately with a simple single cavity, single grating structure the peak shape stays Lorentzian.

Although other techniques such as fiber Bragg-grating, thin-film and integrated optical filters may have better performance for some applications, the main advantage of the RGF approach is the easy fabrication and the large tuning range of the filters.

This study has led to a simple tunable device covering the C-band. The resonance width and wavelength can freely be chosen. The systems dimensions have to be in the millimeter range for efficient operation. In special configurations the device is polarization independent, at the cost of degrees of freedom and assembly precision.

Appendix: Definitions and units

Name of the quantity	symbol	units (S. I.)
Electric field	**E**	V/m
Magnetic field	**H**	A/m
Electric displacement	**D**	As/m^2
Magnetic flux density	**B**	Vs/m^2
Charge density	ρ	As/m^3
Electric current density	**j**	A/m^2
Polarization density	**P**	As/m^2
Magnetization density	**M**	A/m
Electric permittivity of free space	ε_0	As/Vm
Magnetic permeability of free space	μ_0	Vs/Am
Conductivity	σ	A/Vm
Poynting vector	**S**	W/m^2

Acknowledgements

This work would not be able without the support of many persons and institutions. Therefore I would like to thank specially:

- Prof. Hans Peter Herzig for accepting me as his first PhD student as thesis advisor. He had always an open ear for my endless questions and gave me always excellent creative ideas for my problems.

- Prof. René Dändliker that he gave me the possibility to start my PhD at IMT. I was always impressed by his optics knowledge and his sense to find irregularities in the theoretical work.

- Prof. Olivier Parriaux, Dr. Daniel Erni and Dr. Marc Schnieper for accepting to be member of my thesis jury and the time they spent to read and correct the manuscript.

- le centre d'électronique et de microtechnique (CSEM) for their financial support.

- the micro-optics group of CSEM Zürich, especially Mike T. Gale, Dr. Hans Thiele, Dr. Marc Schnieper and Dr. Jürgen Söchtig for their collaboration and the filter fabrication.

- SAMLAB of our institute, especially Dr. Wilfried Noell and Thomas Overstolz for our fruitful collaboration and the many discussions, not only restricted to optics.

- Dr. Andreas Schilling for introducing me in the field of micro-optics and his supervision of my first year at the institute.

- Dr. Martin Salt for helping me in the modeling with rigorous theories.

- Dr. Wataru Nakagawa where I had a great chance to have a person, not only being an English native but also being familiar with the content of my thesis, which accepted to correct my manuscript.
- Dr. Gerben Boer and Iwan Märki for sharing the office.
- Dr. Ville Kettunen for giving me the FMM code for crossed gratings.
- Carsten Rockstuhl, our Matlab crack, for providing software codes.
- Dr. Yves Salvadé for his LabView support.
- the administrative crew for their good work.
- the team of the "service des sports" for allowing me to practice ski hiking, skiing, snowboarding, cross-country skiing, snowshoeing, windsurfing, biking, playing volleyball, squash, tennis, badminton, pétanque, climbing, diving,… I will miss this offer in the future.
- all the past and present members of the Applied Optics team for providing an open and stimulating working atmosphere.
- all my friends, especially Kristina, Roman, and Thomas as well as my parents and family that always trusted in me and helped me to find the balance between work and social life.

References

[ASH76] N. W. Ashcroft and N. D. Mermin, "Solid state physics", Holt, Rinehart and Winston, Orlando, 1976.

[AVR89] I. A. Avrutsky and V. A. Sychugov, "Reflection of a beam of finite size from a corrugated waveguide", J. of Mod. Opt. **36**, 1527–1539 (1989)

[AVR90] I. A. Avrutsky, A. S. Svakhin, V. A. Sychugov, O. Parriaux, "High-efficiency single-order wave-guide grating coupler", Opt. Lett. 15, 1446–1448 (1990)

[AVR91] I. A. Avrutsky, V. A. Sychugov, and A. V. Tishchenko, "The study of excitation, radiation, and reflection processes in corrugated waveguides," in Waveguide Corrugated Structures in Integrated and Fiber Optics, IOFAN Proc. 34 3–98 (1991) (Nauka, Moscow) (Russian).

[BEN01] J. M. Bendickson, E. N. Glytsis, T. K. Gaylord, and D. L. Brundrett, "Guided-mode resonance subwavength gratings: effects of finite beams and finite gratings", J. Opt. Soc. Am. A **18**, 1912–1928 (2001)

[BER79] P. M. van den Berg, J. T. Kokkema, "The Rayleigh Hypothesis in the theory of reflection by a grating", J. Opt. Soc. Am., **69**, 27–31 (1979)

[BER94] J.-P. Berenger, "A perfectly matched layer for the absorption of electromagnetic waves", J. Comp. Phys. **114**, 185–200 (1994)

[BLA99] P. Blattner, PhD thesis, "Light fields emerging from periodic optical microstructures", University of Neuchâtel, 1999

[BOR93] M. Born and E. Wolf, "Principles of Optics", Pergamon Press, Oxford, 1993

[BRA95] J. C. Brazas and L. Li, "Analysis of input-grating couplers having finite lengths", Appl. Opt. **34**, 3786–3792 (1995)

[DAY96] R. W. Day, S. S. Wang and R. Magnusson, "Filter-Response Line Shapes of Resonant Waveguide Gratings", J. Lightwave Techn., **14**, 1815–1824 (1996)

[FAN41] U. Fano, "The theory of anomalous diffraction gratings and of quasi-stationnary waves on metallic surfaces (Sommerfeld's waves)", J. Opt. Soc. Am. **31**, 213–222 (1941).

[FEH02] A. L. Fehrembach, D. Maystre and A. Sentenac, "Filtering of unpolarized light by gratings", J. Opt. A: Pure Appl. Opt. **4**, S88–S94 (2002)

[FEH03] A. L. Fehrembach, A. Sentenac, "Study of waveguide grating eigenmodes for unpolarized filtering applications", J. Opt. Soc. Am. A **20**, 481–488 (2003)

[GOL85] G. A. Golubenko, A. S. Svakhin, V. A. Sychugov, A. V. Thishchenko, "Total reflection of light from a corrugated surface of a dielectric waveguide", Kvantovaya Elektronika, **12**, 1334–1336 (1985)

[GOL85] G. A. Golubenko, A. S. Svakhin, V. A. Sychugov, A. V. Tishchenko, "Total light-reflection from a corrugated surface of a dielectric waveguide", Sov. J. Quantum Electron. **15**, 886–887 (1985)

[GOO96] J. W. Goodman, "Introduction to Fourier Optics", McGraw-Hill, New York, 1996

[HEG00] Z. Hegedus, R. Netterfield, "Low sideband guided-mode resonant filter" Appl. Opt. **39**, 1469–1473 (2000)

[HES65] A. Hessel and A. A. Oliner, "A new theory of Wood's anomalies on optical gratings", Appl. Opt. **4**, 1275–1297 (1965)

[IIZ02] K. Iizuka, "Elements of Photonics", John Wiley & Sons, New York, 2002

[JAC02] D. K. Jacob, St. C. Dunn and M. G. Moharam, "Flat-top narrow-band spectral response obtained from cascaded resonant grating reflection filters", Appl. Opt. **41**, 1241–1245 (2002)

[JAC75] J. D. Jackson, "Classical Electrodynamics", John Wiley & Sons, New York, 1975

[KOG79] H. Kogelnik, "Theory of dielectric waveguides" in *Integrated Optics*, ed. T. Tamir, (Springer, New York 1979), pp. 15–79

[LAC01] D. Lacour, J.-P. Plumey, G. Granet and A. M. Ravaud, "Resonant waveguide grating: Analysis of polarization independent filtering", Opt. and Quant. El. **33**, 451–470 (2001)

[LAC02] D. Lacour, PhD-thesis, "Diffraction d'une onde plane par un guide périodique: application à la conception d'un filtre en longueur d'onde indépendant de la polarisation", Université Blaise Pascal, Clermont Ferrand, France (2002)

[LAL00] Ph. Lalanne and E. Silberstein, "Fourier-modal methods applied to waveguide computational problems", Opt. Lett. **25**, 1092–1094 (2000)

[LAL96a] Ph. Lalanne and G. M. Morris, "Highly improved convergence of the coupled.wave method for TM polarization", J. Soc. Am. A **14**, 779–784 (1996)

[LAL96b] P. Lalanne and D. Lemercier-Lalanne, "On the effective medium theory of subwavelength periodic structures", J. Mod. Opt. **43**, 2063–2085 (1996)

[LEM98] F. Lemarchand, S. Sentenac and H. Giovanni, "Increasing the angular tolerance of resonant grating filters with doubly periodic structures", Opt. Lett. **23**, 1149–1151 (1998)

[LI04] Ch. Zhou and L. Li, "Formulation of the Fourier modal method for symmetric crossed gratings in symmetric mountings", J. Opt. A: Pure Appl. Opt. **6**, 43–50 (2004)

[LI96] L. Li, "Use of Fourier series in the analysis of discontinuous periodic structures", J. Opt. Soc. Am A **13**, 1870–1876 (1996)

[LI97] L. Li, "New formulation of the Fourier modal method for crossed surface-relief gratings", J. Opt. Soc. Am. A **14**, 2758–2767 (1997)

[LOE97] E. G. Loewen and E. Popov, "Diffraction gratings and applications", Marcel Dekker, Inc., New York, 1997

[LYN97] N. M. Lyndin, O. Parriaux and V. A. Sychugov, “Waveguide excitation by a Gaussian beam and a finite size grating”, Sensors and Actuators B **41,** 23–29 (1997)

[MAG92] R. Magnusson and S. S. Wang, "New principles for optical filters", Appl. Phys. Lett. vol. **61**, 1022–1024 (1992)

[MAS85] L. Mashev and E. Popov, "Zero order anomaly of dielectric coated gratings", Opt. Comm. **55**, 377–380 (1985)

[MIZ01] A. Mizutani, H. Kikuta, K. Nakajima and K. Iwata, "Nonpolarizing guided-mode resonant grating filter for oblique incidence", J. Opt. Soc. Am. A. **18**, 1261–1266 (2001)

[MIZ03] A. Mizutani, H. Kikuta and K. Iwata, "Wave localization of doubly periodic guided-mode resonant grating filters", Opt. Rev. **10**, 13–18 (2003)

[MOH82] M. G. Moharam and T. K. Gaylord, "Diffraction analysis of dielectric surface-relief gratings", J. Opt. Soc. Am **72**, 1385–1392 (1982)

[MOH95] M. G. Moharam, E. B. Grann, D. A. Pommet and T. K.Gaylord, “Formulation for stable and efficient implementation of the rigorous coupled-wave analysis of binary gratings,” J. Opt. Soc. Am. A **12**, 1068–1086 (1995)

[NEV80] M. Nevière, "The homogeneous problem" in *Electromagnetic Theory of Gratings*, R. Petit, ed., Springer-Verlag, Berlin 1980, ch. 5.

[NIE03] G. Niederer and HP Herzig, "Modeling polarization independent resonant grating filters", Conference Digest, *Diffractive Optics 2003*, Oxford, UK.

[NOR96] S. M. Norton, T. Erdogan and G. M. Morris, "Coupled-mode theory of resonant grating filters", J. Opt. Soc. Am. A **14**, 629–639 (1997)

[OVE02] T. Overstolz, P.-A. Clerc, M. T. Gale, H. P. Herzig, G. Niederer, W. Noell, J. Söchtig, H. Thiele and N. F. de Rooij, "Tilting out-of-plane platform for optical applications", in International Conference on Optical MEMS, donverence digest (Institute of Electrical and Electronic Engineers, Piscataway, N. J. ,2002), pp. 81–82.

[PAR96] O. Parriaux, V. A. Sychugov and V. Tishchenko, “Coupling gratings as waveguide functional elements", Pure Appl. Opt. **5** (1996) 453–469

[PEN96] S. Peng and G. M. Morris, "Resonant scattering from two-dimensional gratings", J. Opt. Soc. Am. A. **13**, 993–1001 (1996)

[PET80] R. Petit, "Electromagnetic Theory of Gratings", R. Petit, ed., Springer-Verlag, Berlin 1980

[POP01] E. Popov and B. Bozhkov, "Corrugated waveguides as resonance optical filters – advantages and limitations", J. Opt. Soc. Am. A. **18**, 1758–1764 (2001)

[POP02] E. Popov, M. Nevière, B. Gralak and G. Tayeb, "Staircase approximation validity for arbitrary-shaped gratings", J. Opt. Soc. Am. A., **19** (2002), 33–42

[POP86] E. Popov, L. Mashev, D. Maystre, "Theoretical study of the anomalies of coated dielectric gratings", Optica Acta, 33, 607–619 (1986)

[RAY07a] Lord Rayleigh, "Note on the remarkable case of diffraction spectra described by Prof. Wood" Phil. Mag. Series 6, **14**, 60–65 (1907)

[RAY07b] Lord Rayleigh, "On the dynamical theory of gratings", Proc. Roy. Soc. Ser. A, **79**, 399–416 (1907)

[RIG76] W. W. Rigrod and D. Marcuse, "Radiation loss coefficient of asymmetric dielectric waveguides with shallow sinusoidal corrugations", J. Quantum El. **12** (1976), 673–685

[ROS97] D. Rosenblatt, A. Sharon and A. A. Friesem, "Resonant grating waveguide structures", IEEE J. Quantum Eletron. **33**, 2038–2059 (1997)

[SCH02] M. Schnieper, M. T. Gale, C. Zschokke and C. David, "Application and fabrication of subwavelength gratings" in *Diffractive Optics and Micro-Optics*, Technical Digest (Optical Society of America, Tucson 2002), p. 228–230

[SHA96] A. Sharon, D. Rosenblatt, A. A. Friesem, H. G. Weber, H. Engel and R. Steingrueber "Light modulation with resonant grating waveguide structures", Opt. Lett., **21**, 1564–1566 (1996).

[SHA97] A. Sharon, S. Glasberg, D. Rosenblatt and A. A. Friesem, "Metal based resonant grating-waveguide structures", J. Opt. Soc. Am. A. **14**, 588–595 (1997).

[SHI98] D. Shin, S. Tibuleac, T. A. Maldonado and R. Magnusson, "Thin-film optical filters with diffractive elements and waveguides", Opt. Eng. **37**, 2634–2646 (1998)

[SIE86] A. E. Siegman "Lasers", Oxford University Press, Oxford, 1986

[SIL01] E. Silberstein, Ph. Lalanne, J.-P. Hugonin and Q. Cao "Use of grating theories in integrated optics", J. Opt. Soc. Am A **18**, 2865–2875 (2001)

[TAM79] T. Tamir, "Beam and Waveguide couplers", in *Integrated Optics* ed. T. Tamir, Springer New York (1979), pp. 83–137

[THU03] S. T. Thurman and G. M. Morris, "Controlling the spectral response in guided-mode resonance filter design", Appl. Opt. **42**, 3225–3233 (2003)

[TIB97a] S. Tibuleac and R. Magnusson, "Diffractive Narrow-Band Transmission Fitlers Based on Guided-Mode Ressonance Effects in Thin-Film Multilayers", IEEE Phot. Techn. Lett. 9, 464–366 (1997)

[TIB97b] S. Tibuleac and R. Magnusson, "Reflection and transmission guided-mode resonance filter", J. Opt. Soc. Am. A **14**, 1617–1626 (1997)

[TUR97] J. Turunen, ch. 2, "Diffraction theory of microrelief gratings" in *Micro-Optics*, ed. HP Herzig, Francis&Taylor, New York (1997), pp. 31–52

[WIR80] A. Wirgin, "On Rayleigh's theory of sinusoidal diffraction gratings", Opt. Act., **27**, 1671–1692 (1980)

[WOO02] R. W. Wood, "On a remarkable case of uneven distribution of light in a diffraction grating spectrum", Phil. Mag. **4**, 396–402 (1902)